

# High-Magnetic-Field Rydberg Atom Interactions

by  
Eric Gerard Paradis

A dissertation submitted in partial fulfillment  
of the requirements for the degree of  
Doctor of Philosophy  
(Physics)  
in The University of Michigan  
2013

Doctoral Committee:

Professor Georg A. Raithel, Chair  
Professor Paul R. Berman  
Professor R. Paul Drake  
Professor Roseanne J. Sension  
Professor Duncan G. Steel



© Eric G. Paradis 2013  
All Rights Reserved

This work is dedicated to my family.



## ACKNOWLEDGEMENTS

First, I would like to thank Professor Georg Raithel, my advisor, who gave me the opportunity to work on this project. His interest and enthusiasm for every scientific problem that presents itself is infectious, and he is a great example to follow. Over the past five years I have learned an immense amount from his patient explanations. Whether the subject be some practical laboratory problem, computational programming or atomic physics theory, he always seems to have the answer with barely a moment's hesitation. I'll never be able to retain half of that information, but hopefully I've managed to write at least some of it down.

Over the last six years the entire Raithel lab group has also proved to be of great help, and forms excellent support network. When I first joined the lab, the senior graduate students (Tara Cubel, Aaron Reinhard, Brenton Knuffman, Rahul Mhaskar and Rui Zhang amongst others), all took time out of their busy schedules to help me acclimate to the lab environment. They were of enormous help in my first couple years as I adjusted to graduate school. Rui, in particular, showed me how to find the fine line between *'needs to be better'* and *'good enough'*. Dave Anderson, Sarah Anderson, Cornelius Hempel, Andy Schwarzkopf and Mallory Traxler have all worked in the lab at the same time with me, and I thank them for their patience in dealing with me over the years. Hopefully I haven't been a complete bear to be around the entire time.

Everyone who spent time working in SB 271 with the high-field trap is, of course,

an honorary member of the High-B Pirate Mafia, whose trademark is bleary eyes and sleeping in the student office after a night in the lab. Thank you for your help and involvement in the project. I must also acknowledge the work of Jae-Hoon Choi, the previous high-field trap graduate student, whose thesis and notes were immensely helpful as I worked toward understanding the experiment.

Over the past few years, several undergraduate students have also contributed to this experiment, either through summer work terms or while completing a senior research project. One student in particular, Stefan Zigo, proved to be invaluable and deserves many thanks. By the end of his two years with the lab, he could run the experiment completely independently, and shouldered much of the workload. Much of this thesis was accomplished thanks to his tireless enthusiasm and patience.

It's also important to keep a balanced life; to have some form of activity or hobby outside of the  $10 \times 20$  foot SB 271. For me, this was the Goaldiggers, a not-terribly-skilled garage league hockey team here in Ann Arbor that I played on for the past 5+ years. I'd like to thank them for putting up with me missing so many games, and keeping me skating forward toward the goal.

I would like to thank my family, who remained supportive and encouraging throughout the entirety of my somewhat-extended graduate school career. My father, who inspired in me a certain sense of determination, which some might call a stubborn streak. My mother, who despite all her assertions to the contrary, instilled in me all of the qualities necessary to succeed. And of course my siblings; Johanna, Robert and Martin, who still always manage to ask questions that stump me and send me scurrying back to a pile of textbooks.

And finally, to Kelly. She somehow managed to put up with me throughout these years, time and time again brought me life-saving food during the long data runs,

and took care of me once I'd exhausted myself in lab. I can honestly say that without her, I would not have gotten this far.

# TABLE OF CONTENTS

<b>DEDICATION</b> . . . . .	<b>ii</b>
<b>ACKNOWLEDGEMENTS</b> . . . . .	<b>iii</b>
<b>LIST OF TABLES</b> . . . . .	<b>viii</b>
<b>LIST OF FIGURES</b> . . . . .	<b>ix</b>
<b>LIST OF APPENDICES</b> . . . . .	<b>xiii</b>
<b>ABSTRACT</b> . . . . .	<b>xiv</b>
<b>CHAPTER</b>	
<b>I. Introduction</b> . . . . .	<b>1</b>
1.1 Introduction . . . . .	1
1.2 High-magnetic-field trapping . . . . .	3
1.3 Rydberg atoms for quantum information . . . . .	5
1.4 Thesis framework . . . . .	9
<b>II. Rydberg atoms in strong magnetic fields</b> . . . . .	<b>12</b>
2.1 The High-field Hamiltonian . . . . .	12
2.2 Magnetic-field regimes . . . . .	13
2.3 Scaled Energy . . . . .	19
2.4 Landau states . . . . .	20
2.5 Vibrator Pairs . . . . .	21
2.5.1 Gamow estimate . . . . .	23
2.5.2 Numerical one-dimensional model . . . . .	24
2.6 Rubidium ground and first excited states . . . . .	26
<b>III. The high-magnetic-field trap</b> . . . . .	<b>30</b>
3.1 Trapping Apparatus . . . . .	30
3.1.1 Field Geometry . . . . .	30
3.1.2 Cold atom injection into the high-field region . . . . .	32
3.1.3 High-Field Trapping . . . . .	34
3.2 Trapping Characteristics . . . . .	36
3.2.1 Lineshape . . . . .	36
3.2.2 Unusual trap geometries . . . . .	38
3.2.3 Cooling transition spectroscopy . . . . .	39
3.2.4 Trap Temperature . . . . .	42
3.2.5 Trap Lifetime . . . . .	44

3.2.6	Dependence on magnetic field parameters . . . . .	46
3.3	Trajectory Simulations . . . . .	48
3.3.1	Frequency dependence . . . . .	50
3.3.2	Temperature dependence . . . . .	51
3.3.3	Beam asymmetry . . . . .	52
3.4	Summary . . . . .	53
<b>IV. Rydberg atom spectra . . . . .</b>		<b>54</b>
4.1	Experimental Method . . . . .	54
4.1.1	Motivation . . . . .	54
4.1.2	Trap parameters . . . . .	54
4.1.3	Rydberg atom characteristics . . . . .	55
4.2	Rydberg Excitation . . . . .	56
4.2.1	Penning ionization probabilities . . . . .	59
4.3	Overview of Rydberg Spectra and State Density . . . . .	61
4.4	Above-threshold excitation . . . . .	65
4.5	Level Structure at fixed magnetic and varied electric fields . . . . .	68
4.6	Magnetic-field tuning of near-degenerate states . . . . .	73
4.6.1	Comparison of coupling behavior with a two-level system . . . . .	76
<b>V. Rydberg atom calculations . . . . .</b>		<b>80</b>
5.1	Level calculations . . . . .	80
5.2	Magnetic and electric dipole moment statistics . . . . .	82
5.3	Interacting line pair statistics . . . . .	84
5.4	Wavefunction overlap . . . . .	86
5.5	Classical trajectory calculations . . . . .	88
5.6	Applications . . . . .	89
5.6.1	Excitation blockade . . . . .	89
5.6.2	Phase Shift . . . . .	90
5.7	Summary . . . . .	91
<b>VI. Trap limitations and future directions . . . . .</b>		<b>94</b>
6.1	Summary . . . . .	94
6.1.1	Current trap limitations . . . . .	95
6.2	Trap Improvements . . . . .	96
6.2.1	Dipole trap . . . . .	96
6.2.2	Dipole trap schemes . . . . .	100
6.2.3	Zeeman slower . . . . .	101
6.3	Future studies . . . . .	102
6.3.1	Blockade Statistics . . . . .	102
6.3.2	Spatial imaging . . . . .	102
6.3.3	Quadrupole Interactions . . . . .	103
6.3.4	Magnetic trapping . . . . .	104
6.3.5	Plasma studies . . . . .	104
6.3.6	Three-body recombination . . . . .	106
6.3.7	Quantum excitation transport . . . . .	107
6.4	Conclusion . . . . .	108
<b>APPENDICES . . . . .</b>		<b>109</b>
<b>BIBLIOGRAPHY . . . . .</b>		<b>143</b>

## LIST OF TABLES

### Table

1.1	Scaling laws for Rydberg atoms. . . . .	2
B.1	Hyperfine structure constant for the ground and first excited states of $^{85}\text{Rb}$ and $^{87}\text{Rb}$ . . . . .	116

## LIST OF FIGURES

### Figure

2.1	Classical calculation of the electron motion for a Rydberg atom in the $\ell$ -mixing regime of energy $-55 \text{ cm}^{-1}$ , with $B = 0.6 \text{ T}$ . . . . .	15
2.2	Magnetic field regimes versus excitation energy, in wavenumbers ( $\text{cm}^{-1}$ ). . . . .	18
2.3	Electron in a one-dimensional, symmetric double-well potential perturbed by an electric field $F_{\text{el}}$ . . . . .	22
2.4	Numerical solution of the energy levels for the double-well problem. . . . .	25
2.5	Numerically-calculated wavefunctions for the energy levels of the double-well system. . . . .	26
2.6	$^{85}\text{Rb}$ hyperfine structure of the $5\text{P}_{3/2}$ state within a magnetic field. . . . .	27
2.7	Cooling and trapping transition diagram for $^{85}\text{Rb}$ . . . . .	28
2.8	Cooling and trapping transition diagram for $^{87}\text{Rb}$ . . . . .	29
3.1	High magnetic field atom trapping apparatus. . . . .	30
3.2	Contour plot of the magnetic field within the trapping apparatus. . . . .	31
3.3	Schematic of the high-magnetic-field trapping apparatus . . . . .	32
3.4	Measured flux ratio versus frequency detuning from the MOT trapping transition beams. . . . .	33
3.5	Signals from direct atomic beam excitation and out of an optimized trap versus frequency offset of the cooling laser. . . . .	37
3.6	Measurement of frequency spacing and trapping behavior for two $m_l$ sublevels in $^{85}\text{Rb}$ . . . . .	40
3.7	Mixing fraction probabilities ( $\varepsilon^2$ ) versus magnetic field, for $^{85}\text{Rb}$ and $^{87}\text{Rb}$ isotopes. . . . .	42
3.8	Trap temperatures versus the molasses laser frequency. . . . .	43
3.9	Trap decay and loading behavior, taken by spatial integration of the fluorescence signal recorded with the CCD camera. . . . .	44
3.10	Lifetime of the atom trap. . . . .	45

3.11	Fluorescence images of the high magnetic field trap at 2.6 T for different transverse field conditions. . . . .	48
3.12	Trap lifetime versus magnetic field $B_0$ for both Rb isotopes. . . . .	49
3.13	Simulated steady-state number of trapped atoms versus molasses laser frequency offset $\nu_{\text{ofs}}$ . . . . .	50
3.14	Simulated trap position along the field axis versus axial beam asymmetry parameter $\eta$ . . . . .	52
4.1	Timing schematic of the Rydberg excitation pulse. . . . .	57
4.2	MCP phosphor screen images, showing the extent of the excitation region transverse to the magnetic field axis. . . . .	58
4.3	Fraction of counts from a 10 $\mu\text{s}$ Rydberg excitation pulse arriving as free electrons versus delay time, for various energy levels. . . . .	60
4.4	Sample Rydberg excitation spectra, with $F_{\text{el}} = 0$ , for lower energy ranges. . . . .	62
4.5	Sample Rydberg excitation spectra, with $F_{\text{el}} = 0$ , for three higher energy ranges. . . . .	63
4.6	Comparison between observed and calculated density of states (in number of states per GHz) versus excitation energy. . . . .	64
4.7	Sample Rydberg excitation spectra, with $F_{\text{el}} = 0$ , above the field-free ionization threshold. . . . .	66
4.8	Time-resolved signal from several Rydberg resonances above the field-free ionization threshold. . . . .	67
4.9	Comparison between observed and calculated Rydberg levels in the vicinity of scaled energy $\varepsilon \approx -0.51$ . . . . .	69
4.10	High-resolution contour plot showing the pair of Rydberg states labeled “X” at $-55.1 \text{ cm}^{-1}$ , with $B_{\text{exp}} = 2.576 \text{ T}$ and excitation pulse lengths of 10 $\mu\text{s}$ . . . . .	70
4.11	Comparison between observed and calculated Rydberg levels observed in the vicinity of $\sim -31 \text{ cm}^{-1}$ . . . . .	73
4.12	Scans of the state pair labeled “X” in Fig. 4.9 for the indicated magnetic field values and a weak parallel electric field $F_{\text{el}} \approx 1 \text{ V/m}$ . . . . .	74
4.13	Magnetic field scan from Fig. 4.12, with colored lines to show the magnetic dipole moments. . . . .	75
4.14	Energy levels of the simplified two-level Hamiltonian versus electric field, for $B = B_0$ . . . . .	77
4.15	Comparison of the line splitting between the even and odd states. . . . .	78
4.16	Comparison between experimentally-measured ratio of the $m_J = 3/2$ , $\Pi_z = \text{even}$ peak and the $\Pi_z = \text{odd}$ peak versus magnetic field offset $B_0$ , with an applied electric field of $F_{\text{el}} = 1 \text{ V/m}$ . . . . .	79



5.1	Magnetic and electric dipole moment histograms of states from $-60 \text{ cm}^{-1}$ to $-50 \text{ cm}^{-1}$ , for $B_{\text{th}} = 2.581 \text{ T}$ . . . . .	83
5.2	Number of interacting state pairs versus excitation energy, binned in increments of $10 \text{ cm}^{-1}$ . . . . .	84
5.3	Scatter plot of line pairs for the energy range between $-60 \text{ cm}^{-1}$ and $-50 \text{ cm}^{-1}$ . . . . .	85
5.4	Calculated normalized electron wavefunction probabilities $P =  \psi(\mathbf{r}) ^2 r \sin \theta$ , with $B_{\text{th}} = 2.589 \text{ T}$ and $F_{\text{el}} = 0 \text{ V/m}$ . . . . .	87
5.5	Calculated normalized electron wavefunction probabilities $P =  \psi(\mathbf{r}) ^2 r \sin \theta$ , with a weak parallel electric field of $F_{\text{el}} = 3 \text{ V/m}$ . . . . .	88
5.6	Classical electron trajectories at an energy of $\sim -55.1 \text{ cm}^{-1}$ , $B_{\text{th}} = 2.580 \text{ T}$ . . . . .	90
5.7	Applied electric field pulse versus time, and resulting dipole moment $p(t)$ and phase shift $\Delta\phi$ . . . . .	91
6.1	Sketch of a dipole trap overlapped with the magnetic potential minimum. . . . .	96
6.2	Contour plot of the trapping potential (in MHz) with the addition of a dipole trap with $P = 5 \text{ W}$ , $w_0 = 27 \text{ }\mu\text{m}$ . . . . .	98
6.3	Scan taken with the dipole trap being applied, at $2 \text{ W}$ and $6 \text{ W}$ . . . . .	99
6.4	Possible experiment investigating the presence of spatial correlations within a sample of excited Rydberg atoms. . . . .	103
6.5	Sample averaged image of simultaneous excitation of two different Rydberg states. . . . .	108
B.1	$^{85}\text{Rb}$ hyperfine structure of the $5\text{P}_{3/2}$ state within a magnetic field. . . . .	115
B.2	$^{85}\text{Rb}$ hyperfine structure of the $5\text{P}_{1/2}$ state versus magnetic field. . . . .	116
B.3	$^{87}\text{Rb}$ hyperfine structure of the $5\text{S}_{1/2}$ ground state versus magnetic field. . . . .	117
B.4	$^{87}\text{Rb}$ hyperfine structure of the $5\text{P}_{1/2}$ state versus magnetic field. . . . .	117
C.1	Pictures of electron signal impinging upon the MCP detector, for subsequent steps of the delay time. . . . .	120
C.2	Two-dimensional plot of time-resolved signal from the Penning Trap versus hold time within the trap. . . . .	121
C.3	Summed signal, for each set delay time, showing the magnetron motion. . . . .	122
D.1	Pyramidal trap performance versus applied $5\text{S}_{1/2} \rightarrow 5\text{P}_{3/2}$ molasses frequency. . . . .	123
D.2	Sample time-resolved data of the atom flux being suddenly turned on/off via magnetic field coil switching. . . . .	124
D.3	Mean speed versus pusher beam frequency. . . . .	125

D.4	Calculated ratio of the atomic beam flux versus pusher beam frequency, as compared to the case of no pusher beam. . . . .	126
E.1	Helium loss rate from the inner dewar during operation. . . . .	128
E.2	Top of the high-magnetic field apparatus. . . . .	129
E.3	Picture of the liquid helium transfer tube. . . . .	132
E.4	Examples of molasses beam profiles . . . . .	134
E.5	Pusher beam alignment . . . . .	135

## LIST OF APPENDICES

### Appendix

A.	Derivation of the magnetic-field Hamiltonian . . . . .	110
B.	Rubidium hyperfine structure . . . . .	114
C.	Electron motion in a Penning trap . . . . .	118
D.	Optical injection into the high-field trap . . . . .	123
E.	High-B: a How-to Guide . . . . .	127
	E.1 Introduction . . . . .	127
	E.2 Coils . . . . .	127
	E.3 Lasers . . . . .	133
	E.4 Counts . . . . .	135
	E.5 Checklist . . . . .	140

## ABSTRACT

In this thesis I examine high-magnetic-field Rydberg spectra, with the goal of discerning the viability of using such states as an interaction mechanism for quantum computation processes. In the presence of a strong magnetic field of  $B_0 = 2.6$  T, high-lying states of  $E \sim -55$  cm<sup>-1</sup> are non-degenerate and show a wide range of magnetic dipole moments. Near-degenerate pairs of states of the same  $m_J$  manifold but of different axial parity  $\Pi_z$  will strongly interact in the presence of an applied weak parallel electric field  $F$ , generating a pair of highly polar states. I show experimental results that, in agreement with theoretical work presented here, illustrate the presence of strong permanent dipole moments  $p \approx 1500$   $ea_0$  under these conditions. Such Rydberg states can also be tuned into resonance through careful control of the magnetic field, and are suitable for developing quantum phase gates and performing Rydberg-Rydberg interaction experiments.

In order to perform such high-field Rydberg excitation experiments, a stable, dense and well-controlled cold atom cloud is needed within a high-magnetic-field environment. Toward this end, I present a full characterization of the utilized high-field trapping apparatus, including measurements of the trapped atom sample size, shape, and temperature. Analysis of the loss rate from the high-magnetic-field atom trap, both as a function of the applied magnetic field  $B_0$  and transverse confinement, are presented. Experimental results for the high-field confinement of <sup>85</sup>Rb are presented, as well as the first demonstration of a high-field <sup>87</sup>Rb trap. Current

trap limitations and possible improvements to the trapping apparatus are discussed. Other applications of the high-magnetic-field trap, such as the investigation of ultracold two-component plasmas and three-body recombination experiments, are also presented.

## CHAPTER I

### Introduction

#### 1.1 Introduction

Rydberg atoms, or atoms with an electron excited to a high-lying electronic energy state, bear unique characteristics that bridge the gap between the classical and quantum worlds [1]. The effective size of an atom scales with the square of the principal quantum number  $n$  of the valence electron, while the electron motion slows down correspondingly, vastly increasing the time that the atom spends in this high-lying state before decaying back down to the ground level. This means that high- $n$  Rydberg atoms are quasi-macroscopic objects with sizes that are on the micron scale and whose long-lived valence electron is far enough removed from the positive core that it can interact strongly with outside forces. Many atomic properties such as the lifetime and the Rydberg atom dipole moment will correspondingly scale up with the atom size. Because of this, Rydberg atoms are host to a range of exaggerated characteristics, such as their strong polarizabilities (which scale as  $n^7$ ) [2] and large energy-exchange collisional cross-sections (scaling as  $n^4$ ) [3]. Table 1.1 shows some other typical energy scalings.

Such exaggerated properties results in an increased sensitivity to outside forces and makes Rydberg atom systems useful for the development of delicate field sensors.

Property	Scaling	Property	Scaling
Binding energy	$n^{-2}$	Atom size	$n^2$
Dipole moment	$n^2$	Collisional cross-section	$n^4$
Rydberg state lifetime	$n^3$	$n$ -level splitting	$n^{-3}$
Ionization electric field	$n^{-4}$	Polarizability	$n^7$
Excitation Rabi frequency	$n^{-3/2}$		

Table 1.1: Scaling laws for Rydberg atoms.

Rydberg atoms can also be used to probe the quantum world by conducting precise measurements of fundamental constants [4, 5]. Indeed, Rydberg atoms have been employed in a wide variety of experiments and applications, ranging from many-body physics studies [6] and plasma studies [7] to precision measurements [8, 9]. Rydberg atoms have recently been used to create non-dispersive local wave packets [10], an analogous system to Jupiter’s Trojan asteroids. They can also form macrodimers [11], or giant loosely-bound molecules whose component atoms are separated by large distances. Because of their delicate nature, these may in turn be used to study sensitive effects such as vacuum fluctuations or correlations in quantum gases. Perhaps most importantly for the context of this work, Rydberg atoms are also being used for quantum information processing [12] via the blockade mechanism[13].

Although scientists have been interested in the unusual properties of Rydberg atoms for many years, it was not until the recent development of neutral atom trapping and cooling techniques that high-precision experiments could take place. Atom trapping occurs when a cold atomic sample is tightly confined and cooled to temperatures at the microKelvin level. Since the first realization of a cold atom trap in 1986 [14], they have proven to be a fruitful stage for a multitude of research efforts, including precision spectroscopy [15, 16], trace and rare gas analysis [17, 18], Bose-Einstein Condensation [19], precision clocks [20, 21] and high-precision measurements [22]. The low temperatures eliminate many frequency broadening concerns and time

constraints that arise from using hot gases or atomic beams. Various types of atom traps have been developed, such as Magneto-Optical Traps (MOTs), optical dipole traps [23] and Ioffe traps [24].

Another remarkable achievement was the parallel development of traps for charged particles, such as Penning [25–28] and Paul traps [29]. In contrast with neutral atom traps, ion traps allow for storage and selective separation of charged particles, and have been essential to advance mass spectrometry [30], containment of anti-matter particles [31, 32], and quantum information processing.

## 1.2 High-magnetic-field trapping

The primary experimental platform for this thesis work is a high-magnetic-field atom trap, a new type of trap recently developed by the Raithel research group [33] in order to investigate the high-magnetic-field regime for neutral atoms and ultracold plasmas. This trap, capable of operating at fields of up to 3 T, represents a twenty-fold increase over previous efforts [34] to achieve atom trapping within a large bias magnetic field. Previous atomic physics experiments in magnetic fields in the Tesla range had been completed with atomic beams [35–37]. The high field trap, in contrast, enables us to perform precision spectroscopy with exquisite control of the electric field in the atoms’ rest frame, all while controlling the magnetic field offset down to the Gauss level of accuracy, with magnetic-field stability around the 10 mG level. The high-magnetic field trap has already been used in the first demonstration of Rydberg atom trapping [38]. It is compatible with nested Penning trap configurations, and has been used to create two-component ultracold plasmas via photo-ionization of the trapped atoms [39]. Traps employing similar magnetic-field offsets ( $\sim 3$  T) and magnetic-field potential curvature are currently in use at CERN,



having been developed to contain anti-hydrogen atoms formed through three-body recombination processes [40, 41]. Three-body recombination (where the collision between two free electrons and a positive ionic core results in a bound Rydberg atom and a hot electron) has previously been examined [42], but using a high-magnetic-field trap may offer better insight into the temperature and density scalings for the particular magnetic field conditions used in the anti-hydrogen experiments. Since the valence electron in a Rydberg atom is quite loosely bound, Rydberg atom samples also Penning-ionize in large numbers in an analogous fashion to three-body recombination. This in turn leads to the formation of a two-component ultracold plasma [43].

The primary focus of this thesis work is the investigation of Rydberg atom spectra within a high magnetic field (1 to 3 T). One particularly interesting characteristic of highly-excited atoms is that they are strongly affected by the presence of magnetic fields. The atomic unit of magnetic field (corresponding to  $2.35 \times 10^5$  T in S.I. units) is incredibly large and unattainable under laboratory conditions. Because of this, magnetic fields are usually only considered as small perturbations to the electron wavefunction; in a typical ground state atom it is tightly confined and governed by the Coulomb force. However, in the case of a Rydberg atom the large separation between the charged core and the valence electron diminishes the strength of the Coulomb interaction term. In this case, the presence of a magnetic field will strongly affect the wavefunction and energy levels. For highly-excited Rydberg atoms the energy contribution from the diamagnetic interaction (which has cylindrical symmetry) rivals the strength of the spherically-symmetric Coulomb term. Such systems can be studied as examples of chaotic classical dynamics [44].

Using our unique high-magnetic-field trap Rydberg atoms can be created in well-

controlled conditions over a wide range of applied magnetic field values. Additionally, an electrode package also allows for the application of electric fields that are parallel to the magnetic-field axis. As I will demonstrate in this thesis, careful selection of applied electric and magnetic field conditions results in Rydberg states that bear ideal characteristics for quantum information processes, a current area of considerable research interest, motivating the study and manipulation of quantum systems. Indeed, the 2012 Nobel prize was awarded to Serge Haroche and David Wineland for “*ground-breaking experimental methods that enable measuring and manipulation of individual quantum systems.*” Wineland with trapped ions, and Haroche with photon-cavity systems, were both able to prepare their experimental systems in a manner so as to create highly entangled states. This represents an important step towards harnessing the quantum systems for quantum information processing.

### **1.3 Rydberg atoms for quantum information**

As modern computing demands continue to increase, the size of transistors has been driven down in order to achieve faster processing speeds. However, soon quantum mechanical effects will begin to interfere with the operation of these electrical devices. Today’s transistors are already operating close to the nanometer scale [45]. It is predicted that the size of transistors will reach this fundamental limit, at around 5 nm, by 2020 [46]. This represents a physical limit that poses severe constraints to any further improvements of modern computer processing speeds, making this a pressing concern.

A new type of computer has been conceived that can surpass this classical limit by taking advantage of quantum mechanical effects. Such a quantum computer would harness the quantum superposition principle, where instead of the classical binary

bit (information stored as a binary state of either a 0 or 1), there would instead be a quantum state capable of existing as either a  $|0\rangle$ , a  $|1\rangle$ , or any coherent superposition thereof. A quantum computer would use these quantum bits, or ‘qbits’, and perform many parallel processes on a superposition state before finally reading out the result of these operations. The resulting computing system would offer an essential speed advantage over a classical computer, and could be used for specific applications as well, for example in the fields of encryption [47], prime number factoring [48, 49] and implementing faster search algorithms [50].

In order to achieve quantum computation, the candidate system needs to meet a particular set of requirements [51], including the ability to perform operations faster than the decoherence time of the system. Many quantum systems are currently being studied in order to assess their viability for quantum computing purposes. Rydberg atoms represent a promising candidate system because they are easily trapped (as ground-state neutral atoms), have extended lifetimes and are capable of long-range interactions. Already several proposals and experiments have demonstrated that Rydberg atoms are useful for creating quantum gates [13, 52, 53].

To date, the most significant vehicle toward the development of a viable qbit has been the use of strong interactions between Rydberg levels to control the number of excited atoms. In such a ‘Rydberg blockade’, the presence of a Rydberg excitation within an atomic ensemble is used to inhibit the formation of a second Rydberg excitation within a certain volume. In the region close to the first Rydberg excitation the dipole interaction will shift the energy levels of the nearby atoms. If a narrow-band laser is being used to excite the atoms, this can detune the energy levels completely out of resonance and thus prevent a second Rydberg excitation from occurring within a given distance. If this characteristic blockade radius increases to

the size of the ensemble, the ensemble of atoms can carry either zero or one Rydberg excitations, but never any more. It is then possible to use the absence or presence of a control Rydberg atom to conditionally excite a second one within the sample. This has immediate practical applications for quantum information processes, and the blockade has been used to produce entangled pairs of atoms [54] and to implement a CNOT-gate [55].

In order to practically implement a blockaded Rydberg system, both strong electrostatic Rydberg-Rydberg interactions as well as reasonably high optical excitation rates of Rydberg levels in question are necessary. In particular, there are three common methods of achieving the required strong electrostatic interactions within Rydberg atoms: through the use of static electric fields, via Förster resonances [56–58], or by using a second-order van-der-Waals interaction [59, 60]. So far, these methods have all been investigated within low-magnetic-field systems as possible coupling mechanisms to be used in order to create interacting qubits.

In the first case, the presence of two nearby strongly-polarized Rydberg atoms (acting effectively as dipoles) due to an applied electric field will induce an energy shift. This effect scales with the size of the individual dipole moments ( $p_1$  and  $p_2$ ) and the distance  $r$  between the dipoles:

$$V_{\text{Int}} \simeq \frac{1}{4\pi\epsilon_0} \frac{\mathbf{p}_1 \cdot \mathbf{p}_2 - 3(\mathbf{p}_1 \cdot \hat{\mathbf{n}})(\mathbf{p}_1 \cdot \hat{\mathbf{n}})}{r^3} \quad (1.1)$$

Here  $\hat{\mathbf{n}}$  is the normal vector aligned with the electric field axis. For a strong interaction, levels with large permanent electric dipole moments are needed. Such states can be found, for instance, in linear Stark states [3, 44]. However, these states tend to have small optical excitation cross sections, and the close proximity of other Stark states can complicate the system through unwanted energy level crossings and

state mixing.

Although in the absence of any external field Rydberg atoms do not have permanent electric dipole moments, a strong interaction can still exist in the form of a transition dipole moment to other near-lying states. Whether this transition is resonant or not will determine whether the interaction is a dipole-dipole (resonant) interaction or a van der Waals (off-resonant) type of interaction, and consequently will also determine the energy and distance scaling [3, 61, 62].

The second method is to use Rydberg levels that exhibit an energy exchange (Förster) resonance [58, 63], where a pair of excited Rydberg states  $2|A\rangle$  are resonant with another set  $|B\rangle + |C\rangle$ , with significant dipole transition elements  $\langle A|\hat{d}|B\rangle$  and  $\langle A|\hat{d}|C\rangle$ . Such Förster resonances do occur occasionally within the Rydberg energy level spectrum. Additionally, these transitions can be tuned into exact resonance (giving an energy defect of zero) either by applying external DC electric fields [56, 64] or by using AC Stark shifts [65]. However, if the excited Rydberg state  $|A\rangle$  is degenerate, as is often the case due to the presence of magnetic sub-levels, some unwanted complications may arise. If a sub-level here has a dipole-dipole matrix element equal to zero as well as a strong light coupling, the Förster resonance will lose its long-range dipole-dipole character: the presence of this Förster zero [66] allows for excitation of close-lying Rydberg atoms and effectively lifts the Rydberg blockade. Further, there are only a limited number of levels that exhibit Förster resonances within a given atomic species. This limits the usefulness of the dipole-dipole interaction to a few select energy values.

In the third case, where the transition channel is non-resonant (i.e., the energy detuning is much greater than the strength of the interaction term), the induced van-der-Waals energy shift is a second-order effect. Here the scaling of this shift ( $n^{11}/r^6$ )

falls off rapidly with distance, and so is not quite as conducive toward generating long-range Rydberg-Rydberg interactions.

Since robust atom-atom interaction schemes require insensitivity to moderate variations of the various experimental parameters such as initial-state preparation, laser polarizations, stray electric and magnetic fields, level degeneracies and near-degeneracies should be avoided if at all possible. Degeneracy-free atomic levels allow for atom-atom interactions without the added complication of possible unwanted state mixing effects. With this goal in mind, in this thesis I explore the Rydberg atom spectrum in the presence of both a strong magnetic field  $B$  and a weak parallel electric field  $F_{\text{el}}$ . The aim is to prepare states with large dipole moments, large optical excitation cross sections, and no close degeneracies with other states.

#### 1.4 Thesis framework

Although the presence of a magnetic field is usually considered to be a perturbative effect, in Rydberg atoms the presence of a strong magnetic field can drastically alter the system. In Chapter II, I present a detailed discussion of the high-magnetic-field Hamiltonian. I detail the extent and characteristics of several different energy regimes that depend on the relative strength of the magnetic-field term. I also present a simple one-dimensional model system to illustrate the behavior of remnant near-degenerate Rydberg state pairs in the presence of a large magnetic field, where pairs of states with opposing axial parity ( $\Pi_z$ ) are separated by a small energy defect ( $\Delta E$ ). I also show that the high-magnetic-field allows for excitation of states above the field-free ionization threshold; these states follow ionization bands according to  $m_J$ . Finally, in the ground and first excited states of rubidium the magnetic field has the effect of decoupling the  $I$  and  $J$  quantum numbers. The separation of the

sub-levels into groups of the same  $m_J$  are presented.

The base of the high-field experiment is a high-magnetic-field atom trap. The ability to control both the large magnetic field offset and the transverse magnetic field curvature of the trap gives a high degree of control for the creation and manipulation of cold atomic samples within a magnetic field ranging from 1-3 T. In Chapter III, I present a detailed description of a high-field atom trap [33] in which atoms are cooled and confined at a local magnetic field minimum, within a field of several Tesla at location of the trap center. This trap is an ideal means of performing high magnetic field spectroscopy: by cooling the atoms, the motional Lorentz electric field  $\mathbf{F}_{\text{el}} = \mathbf{v} \times \mathbf{B}$  is reduced down to a few mV/cm, much lower than in atomic beam experiments and close to our experimental electric field noise limit. Additionally, the high-field trap exhibits several unusual features, including highly asymmetric trap fluorescence spectra and shell-like atom density distributions when the cooling laser is blue-detuned from the trap fluorescence line center. In this Chapter I conduct a detailed analysis of the laser cooling properties of this trap, describing the specifics of the trapping mechanism and the experimental setup. I also present my numerical simulation work, that reproduces the trap characteristics and provides a more in-depth understanding of the underlying mechanics of this system. The simulation results agree well with experimental observations and provide additional insight into the trapping behavior.

The primary experimental focus of this thesis work is the exploration of the potential of using highly-excited atoms within a large magnetic field environment for Rydberg-atom interaction studies, and possibly for quantum information purposes. In Chapter IV, I explore the high-field states and present a series of Rydberg level spectra for various excitation energies. I also show the presence of strong auto-

ionizing states above the field-free ionization threshold. A parallel weak electric field is used to generate and investigate dipole moments of Rydberg states. I present detailed observations showing the presence of pairs of near-degenerate states with extremely large electric dipole moments.

I follow this with a series of state calculations in Chapter V that shows the source of these strongly-interacting state pairs; they are pairs of states extending primarily along the  $z$ -axis, with opposing  $z$ -parity, and whose strong wavefunction overlap gives rise to large dipole moments under an applied electric field  $F_{\text{el}}$ . I investigate the abundance of these interacting pairs and their suitability for quantum information purposes. I also explore the effect of incrementing the large axial magnetic field by small controllable steps of 10 G, and discuss how this can be used as an additional controllable parameter to tune the quantum states.

In Chapter VI I look to the future by discussing the current limitations of the trapping apparatus, the most significant being the atom density. Potential improvements, including the application of an optical dipole trap, are presented. In addition, I briefly outline several potential future experiments, such as the possibility to create two-component ultracold plasmas or the investigation of quantum state hopping in Rydberg atom samples. As well, the high-magnetic-field trap offers some intriguing possibilities into looking at dynamics between Rydberg atoms and free electrons.



## CHAPTER II

### Rydberg atoms in strong magnetic fields

#### 2.1 The High-field Hamiltonian

In this section, I consider the case of an atom with a single valence electron and infinite nuclear mass in the presence of both magnetic and electric fields. Within the high-magnetic-field trapping apparatus atoms are subjected to large magnetic fields as well as a weak parallel electric field. As such, the Hamiltonian will contain non-zero magnetic and electric field components. The problem is simplified by using the symmetric gauge and choosing to align the fields with the  $z$ -axis:

$$\mathbf{A}(\vec{r}) = -\frac{1}{2}(\mathbf{r} \times \mathbf{B}) = -\frac{1}{2}(y\hat{x} - x\hat{y})B_z \quad (2.1)$$

Using this gauge, one can rewrite the Hamiltonian for an atom in parallel electric and magnetic fields as (see Appendix A):

$$\hat{H} = \frac{\hat{\mathbf{p}}^2}{2} - \frac{1}{\hat{r}} + F_{\text{el}}\hat{z} + \frac{B}{2}(\hat{\ell}_z + g\hat{s}_z) + \frac{B^2}{8}\hat{\rho}^2 + \hat{V}_{\text{LS}} + \hat{V}_{\text{C}}(r) \quad (2.2)$$

Here,  $\hat{\mathbf{p}}$  is the momentum operator and  $\hat{r}$  is the radial component of the position operator. The electric and magnetic fields  $F_{\text{el}}$  and  $B$  are directed along the  $z$ -axis,  $\hat{V}_{\text{LS}}$  represents the fine structure and  $\hat{V}_{\text{C}}(r) = V(r) + 1/r$  is the core potential, present

within the inner ionic core to account for interaction with the other bound electrons. This can be accounted for through the quantum defects [3, 44]. The operators  $\hat{\ell}_z$  and  $\hat{s}_z$  represent the orbital and spin angular momenta of the Rydberg electron in the field direction, and  $g = 2 + \alpha/\pi \approx 2.00232$  is the electron  $g$ -factor. Other QED effects such as the Lamb shift are not considered, and the hyperfine structure is similarly discounted. Because of the azimuthal symmetry present in the problem (there is no  $\phi$ -dependence), the total angular momentum  $\hat{j}_z = \hat{\ell}_z + \hat{s}_z$  is conserved. The diamagnetic term,  $B^2 \hat{\rho}^2/8$  (where  $\hat{\rho}^2 = \hat{x}^2 + \hat{y}^2$ ), will rapidly become dominant in the case of a strong magnetic field. The  $1/r$  Coulomb potential is spherically symmetric, whereas the magnetic effects are cylindrically symmetric, leading to classical chaos at high magnetic field strength [44].

There also exists another important symmetry to the Hamiltonian, namely the parity  $\Pi_z$ , which is an inversion across the  $x - y$  plane:  $\Pi_z \psi(x, y, z) \rightarrow \psi(x, y, -z)$  [3]. The parity  $\Pi_z$  is a discrete symmetry (even/odd), having eigenvalues of  $\{1, -1\}$ . Since replacing  $\hat{z} \rightarrow -\hat{z}$  in the Hamiltonian (equation 2.2) only affects the electric field term ( $F_{\text{el}} \hat{z}$ ), in the absence of an electric field ( $F_{\text{el}} = 0$ ) the Rydberg atom wavefunctions all have a definite parity, and will either be even or odd under the  $\Pi_z$  parity operation.

## 2.2 Magnetic-field regimes

Considering the case of weak electric fields ( $F_{\text{el}} \approx 0$ ) for now, the electric-field term in the Hamiltonian can be neglected. In this case, the defining feature of the Hamiltonian is the strength of the magnetic field. When the diamagnetic term in the Hamiltonian is gradually increased the system progresses through several qualitatively different regimes. For the case of low magnetic fields, the diamagnetic term

is vanishing compared to the linear Zeeman term:

$$\begin{aligned} \frac{\rho^2 B^2}{8} &\ll \frac{B}{2} \\ \frac{(1.5 n^2)^2 B^2}{8} &\ll \frac{B}{2} \\ B &\ll \frac{4}{2.25 n^4} \approx 2n^{-4} \end{aligned} \quad (2.3)$$

Here I have used the fact that the radius of a Rydberg atom scales as  $r = 2n^2$  for  $\ell = 0$  states and  $r = n^2$  for maximal  $\ell = n - 1$  states, writing an approximate value of  $\rho \sim 1.5n^2$ . In this low-field regime the linear Zeeman shift lifts some of the zero-field Rydberg level degeneracies by separating states of different magnetic quantum numbers  $m_J$ . However, states of the same  $n$  and  $m_J$  and without an appreciable quantum defect are still approximately degenerate.

If the magnetic field is further increased, the Hamiltonian enters a regime in which the diamagnetic term ( $\rho^2 B^2/8$ ) becomes important. This has the effect of mixing states of different  $\ell$  quantum numbers [67]:

$$\langle n'\ell'm' | \hat{H}_D | n\ell m \rangle = \langle n'\ell'm' | \frac{\rho^2 B^2}{8} | n\ell m \rangle = \langle n'\ell'm' | \frac{(r^2 \sin^2 \theta) B^2}{8} | n\ell m \rangle$$

This matrix element is non-zero in the cases of  $\Delta\ell = 0, \pm 2$ . For  $\Delta\ell = 0$ :

$$\frac{B^2}{8} \langle n'\ell'm' | r^2 \sin^2 \theta | n\ell m \rangle = \frac{B^2}{8} \left[ 2 \frac{(\ell^2 + \ell - 1 + m^2)}{(2\ell - 1)(2\ell + 3)} \right] \langle n'\ell' | r^2 | n\ell \rangle \delta_{\ell',\ell} \delta_{m,m'} \quad (2.4)$$

and for  $|\Delta\ell| = 2$ :

$$\begin{aligned} \frac{B^2}{8} \langle n'\ell'm' | r^2 \sin^2 \theta | n\ell m \rangle = \\ \frac{B^2}{8} \left[ \frac{(\ell_{<} + m + 2)(\ell_{<} + m + 1)(\ell_{<} - m + 2)(\ell_{<} - m + 1)}{(2\ell_{<} + 5)(2\ell_{<} + 1)(2\ell_{<} + 3)^2} \right]^{1/2} \\ \times \langle n'\ell_{>} | r^2 | n\ell_{<} \rangle \delta_{\ell_{>},\ell_{<}+2} \delta_{m,m'} \end{aligned} \quad (2.5)$$

Here,  $l_<$  is the lesser of  $\{\ell, \ell'\}$ . Because  $\langle \hat{H}_D \rangle$  is non-zero for  $|\Delta\ell| = 2$ , states with different  $\ell$  quantum numbers are no longer eigenstates of the systems since they become mixed. This domain, when the diamagnetic term becomes important ( $B > 2n^{-4}$ ), is termed the  $\ell$ -mixing regime. Here most of the remaining level degeneracies are lifted. The energy spectrum in the  $\ell$ -mixing regime is organized into rotator and vibrator states [68, 69]. Rotator states are non-degenerate and have wavefunctions extending mostly in the plane transverse to  $B$ . They have large magnetic dipole moments and large diamagnetic shifts. Vibrator states, on the other hand, have wavefunctions extending mostly in the direction of  $B$ . Their small transverse extent causes their diamagnetic shifts and magnetic dipole moments to be relatively small. They are also two-fold degenerate, with one state having even  $\Pi_z$  and the other having odd  $\Pi_z$ .

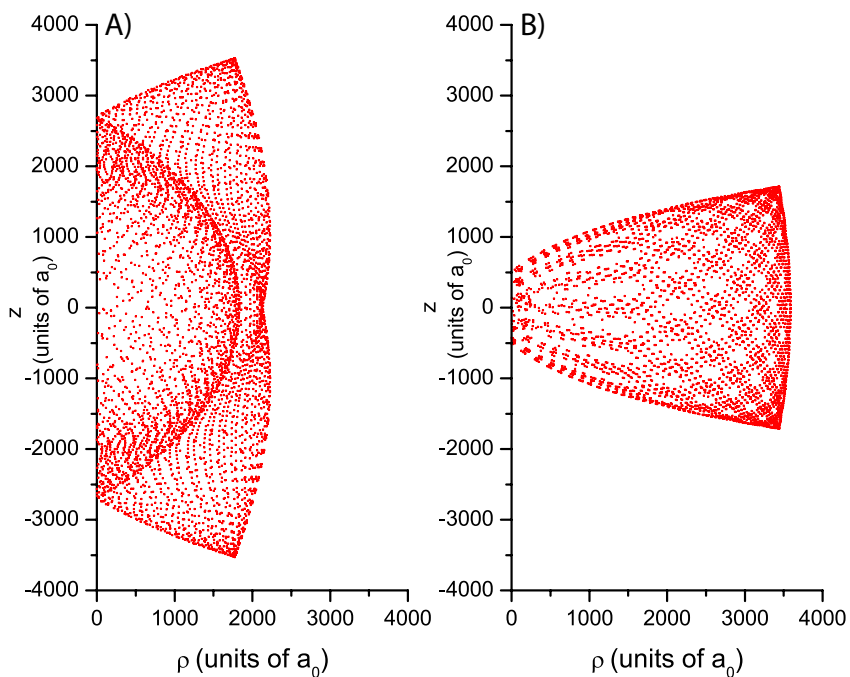


Figure 2.1: Classical calculation of the electron motion for a Rydberg atom in the  $\ell$ -mixing regime of energy  $-55 \text{ cm}^{-1}$ , with  $B = 0.6 \text{ T}$ . A) Vibrator state, showing relatively tight confinement along  $\rho$ . B) Extreme rotator state, which samples a larger extent in the transverse direction.

Figure 2.1 shows the result of a classical calculation for the electron motion of a Rydberg atom of  $-55 \text{ cm}^{-1}$ , with  $B = 0.6 \text{ T}$ , for two different valence electron initialization conditions. The resulting trajectories represent the two different types of wavefunctions within the  $\ell$ -mixing regime. Figure 2.1A is a vibrator state, characterized by an oscillatory electron motion along the magnetic field axis. In contrast, in Fig. 2.1B the electron samples a much larger extent along  $\rho$  as it precesses about the magnetic field axis. This would be a rotator state and bears a much larger magnetic dipole moment as compared to the vibrator states.

As  $B$  is further increased, the system reaches a regime where the diamagnetic energy term becomes greater than the approximate energy spacing  $\Delta E_n$  between the  $n$  manifolds of energy  $E$ :

$$\begin{aligned}
 E &= -\frac{1}{2n^2} \\
 \Delta E_n &\simeq \frac{1}{n^3} \\
 \frac{\rho^2 B^2}{8} &> \Delta E_n = \frac{1}{n^3} \\
 \frac{2n^4 B^2}{8} &> \frac{1}{n^3} \\
 B &> 2n^{-3.5}
 \end{aligned} \tag{2.6}$$

Since the diamagnetic term is larger than the separation between adjacent  $n$  levels, states of different  $n$  are no longer independent and  $n$  is no longer an approximately conserved quantum number. This is termed the  $n$ -mixing regime ( $B \gtrsim 2n^{-3.5}$ ) [36, 70]. As the system enters the  $n$ -mixing regime the level structure organization of rotator and vibrator states, as well as the vibrator-state degeneracies, is increasingly lost. Rydberg levels become more or less evenly spread out in energy and (near-) degeneracies become increasingly less likely. However, some near-degenerate vibrator

pairs do still exist up to comparatively high magnetic field strength.

As the magnetic field strength is even further increased, the size of the diamagnetic energy contribution finally reaches a point where it rivals the Coulomb term ( $-1/r$ ).

This occurs when:

$$\begin{aligned} \frac{\rho^2 B^2}{8} &> \frac{1}{r} = \frac{1}{2n^2} \\ \frac{2n^4 B^2}{8} &> \frac{1}{2n^2} \\ B &> \sqrt{2}n^{-3} \end{aligned} \tag{2.7}$$

In this regime ( $B \gtrsim \sqrt{2}n^{-3}$ ) the spherical symmetry of the Coulomb term is rivaled by the cylindrical symmetry of the diamagnetic term, and the system becomes classically chaotic. Here the classical evolution of the system is highly sensitive to the initial conditions, such that the motion becomes unpredictable except in the case of very short timescales. The corresponding phase space covered by the wavefunction is increasingly dominated by irregular trajectories. Although a bound quantum mechanical system cannot show this same sensitivity to initial conditions, and the quantum spectrum remains discrete [71], the energy structure does exhibit signatures of “quantum chaos” [44]. One hallmark of the chaotic regime is that the nearest-neighbor spacing of the Rydberg states become increasingly regular [72], as a consequence of strong level repulsion.

Figure 2.2 gives a visual representation of the various magnetic field regimes. The Zeeman regime lies below the black line; in the lower left section of the plot. The  $\ell$ -mixing regime lies approximately between the black curve and the red curve (start of the  $n$ -mixing regime), and so forth. Using a standard zero-field atom trap and fast-field switching to probe magnetic regimes only allows one to operate up to fields

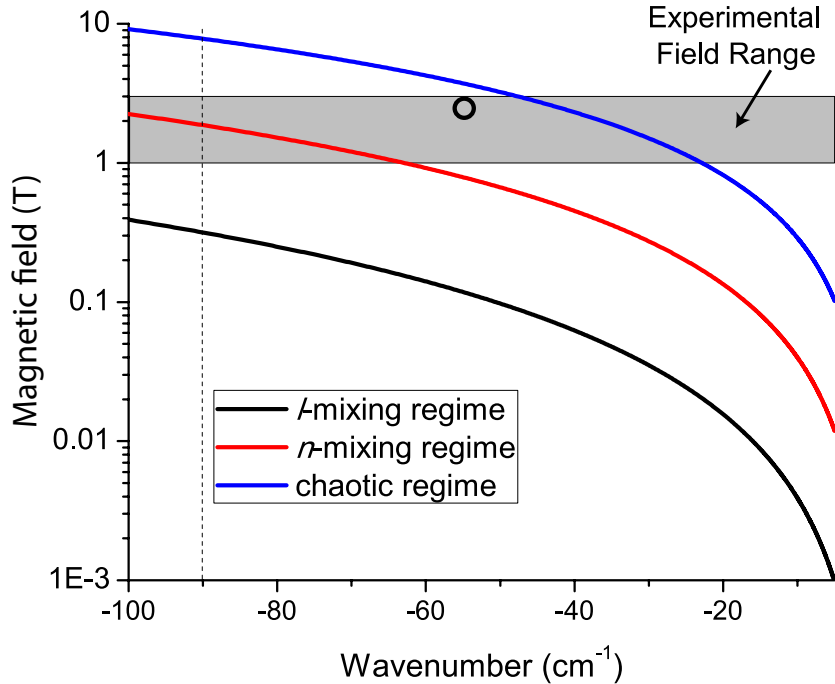


Figure 2.2: Magnetic field regimes versus excitation energy, in wavenumbers ( $\text{cm}^{-1}$ ). The shaded box represents the experimental magnetic field range over which the trap can operate, while the dashed line represents the lower limit for experimental detection, beyond which the maximally applied electric field is not strong enough to ionize the Rydberg atom. The circle shows the specific location a particular pair of states investigated further in Chapter IV.

on the order of 1 kG (0.1 T) or less. This means that in a standard trapping setup, all but the most energetic Rydberg atoms remain in the Zeeman or  $\ell$ -mixing regimes. In contrast, as detailed in Chapter III and shown in the gray region of Fig. 2.2, the high-magnetic-field trap utilized in this work allows for operation in the 1-3 T range, and the energy ranges of the  $n$ -mixing and chaotic regimes correspondingly become much more accessible.

The primary focus of this thesis is upon states in the  $n$ -mixing regime, where the Rydberg levels are well spread out in energy, while at the same time a few near-degenerate vibrator pairs are left. At  $B \approx 2.6$  T, this corresponds to a range of  $32 \lesssim n \lesssim 56$  (or equivalently  $-108 \text{ cm}^{-1}$  to  $-35 \text{ cm}^{-1}$ ). At energies above  $-35 \text{ cm}^{-1}$ , the density of states generally becomes so high that isolated, near-degenerate level

pairs with the mixing properties described in the following section and with negligible perturbation from nearby states become hard to find.

### 2.3 Scaled Energy

One useful measure of Rydberg atom systems is the scaled energy  $\varepsilon$  parameter [44]. The scaled energy is a convenient method to describe the classical dynamics of the Rydberg atom, as it is dependent on both the excitation energy of the atom and the applied magnetic field. In atomic units, the scaled energy is:

$$\varepsilon = EB^{-2/3} \quad (2.8)$$

This scaled energy ranges from  $-\infty$  for low values of  $E$  and  $B$ , up to a maximal value approaching zero in the case of increasingly high fields and Rydberg level energies. Below  $\varepsilon \approx -0.35$  [73, 74] the phase space is dominated by regular trajectories of the electron motion. Above this threshold, the phase space is characterized by irregular trajectories, as the electron motion becomes chaotic. This division matches well the onset of the chaotic regime as described in Sec. 2.2. To compare this scaling with the magnetic-field regimes, at a field of 2.6 T, states within the Zeeman regime have scaled energy  $\varepsilon < -2.3$ . The  $\ell$ -mixing regime lies between the bounds  $-2.3 < \varepsilon < -1$ , and the  $n$ -mixing regime  $-1 < \varepsilon < -0.4$ .

Most of the studies presented in this thesis are at scaled energy  $\varepsilon \approx -0.5$ , with  $B \approx 2.6$  T and  $E \sim -55$  cm<sup>-1</sup>. In this regime, the electron motion is still predominantly regular. The instantaneous magnetic dipole moment of the states are given by the level energy slope ( $-\partial E/\partial B$ ). These depend on the transverse extent of the electron motion and vary widely from state to state. The magnetic moments of remnant, near-degenerate vibrator pairs tend to be relatively low and somewhat different from each other, due to varying, small admixtures of states extending in the plane transverse to



*B.* These admixtures are so small that they do not fundamentally alter the character of the states, but they are sufficient to cause small variations in the magnetic dipole moments of the states.

## 2.4 Landau states

In Chapter IV spectra of near- and above-threshold Rydberg atoms are presented. It is therefore important to also examine the free electron problem. For the case of a free electron in high-magnetic fields, the cyclotron motion results in the Landau quantization [44] of energy levels. The problem may be solved in cylindrical coordinates, resulting in the following solution:

$$\begin{aligned}\psi_{n_c,m,k}(\rho, \phi, z) &= \Phi_{n_c,m}(\rho)e^{im\phi}e^{ikz} \\ \Phi_{n_c,m}(\rho) &= C_{n_c,m}e^{-\rho^2/(4a_B)}L_{n_c}^{|m|}\left(\frac{\rho^2}{2a_B^2}\right) \\ E_{n_c,m,k} &= \left(n_c + \frac{1}{2}m + \frac{1}{2}|m| + \frac{1}{2}\right)\hbar\omega_c + \frac{\hbar^2k^2}{2\mu}\end{aligned}\quad (2.9)$$

Here,  $n_c$  is the cyclotron frequency,  $m$  the azimuthal magnetic quantum number and  $\mu$  the mass.  $\omega_c$  is the cyclotron frequency ( $qB/m$ ), while  $a_B = \sqrt{\hbar/(\mu c)}$  is the cyclotron radius ( $r_c = \mu v/(qB)$ ) for energy  $E = (1/2)mv^2 = (1/2)\hbar\omega_c$ .

For an energetic Rydberg atom with high angular momentum ( $|m| \gg 1$ ), the Rydberg Hamiltonian can be adiabatically separated into a slow component along  $\mathbf{B}$  and a fast transverse component. This leads to a guiding center drift-atom solution [44, 75, 76] with energies (including the spin component):

$$W_{n_c,m,m_s} = \left[n_c + \frac{1}{2}(m + |m|) + m_s + \frac{1}{2}\right]\hbar\omega_c$$

For small values of  $|m|$ , the adiabatic approximation is no longer valid, and Landau

states of different  $n_c$  but same  $\{m, m_s\}$  become mixed. Because of this, all low- $|m|$  Rydberg states should contain at least some non-zero  $n_c = 0$  character, and thus can be ionized at this lower potential:

$$\text{IP} = \left[ \frac{1}{2}(m + |m|) + m_s + \frac{1}{2} \right] \hbar\omega_c$$

Since the high-field atom trap confines atoms that are low-field seeking with  $m_s = +1/2$ , all optically-available Rydberg states will see a raised ionization potential. However, in an  $^{85}\text{Rb}$  experiment the actual measured quantity is the ionization energy relative to the intermediate  $5\text{P}|m_I = 5/2, m_J = 3/2\rangle$  level, which uniquely maps onto  $m = 1, m_s = +1/2$ . Accounting for the magnetic-field dependence of this intermediate state, the relative shift to the ionization potential is:

$$\begin{aligned} \Delta\text{IP} &= \text{IP} - W_{5\text{P}} \\ &= \left[ \frac{1}{2}(m + |m|) + m_s + \frac{1}{2} \right] \hbar\omega_c - (1 + 2(1/2)) \frac{\hbar\omega_c}{2} \\ &= \left[ \frac{1}{2}(m + |m|) + m_s - \frac{1}{2} \right] \hbar\omega_c \end{aligned} \quad (2.10)$$

From the intermediate 5P state, the optically available Rydberg levels are  $m = \{0, 1, 2\}$ ,  $m_s = +1/2$ . These correspond to relative ionization potentials of  $\Delta\text{IP} = \{0, \hbar\omega_c, 2\hbar\omega_c\}$  respectively.

## 2.5 Vibrator Pairs

In Chapter IV I present a detailed investigation of observed near-degenerate state pairs within the  $n$ -mixing regimes. Such states show strong interactions, raising the possibility of potential quantum information processing applications. Here I compare such states to a simple one-dimensional model, to better understand the source of

the interaction.

If a small electric field  $F_{\text{el}}$  parallel to  $B$  is applied to Rydberg levels in the  $n$ -mixing regime, non-degenerate diamagnetic states exhibit small second-order quadratic Stark shifts in  $F_{\text{el}}$ . However, near-degenerate pairs of vibrator states of the same  $m_J$  and opposite  $\Pi_z$  will become mixed and lose their well-defined  $\Pi_z$  character already at low values of  $F_{\text{el}}$ , leading to a behavior reminiscent of the linear Stark effect. If the two near-degenerate levels are vibrator states of similar overall wavefunction structure and opposite  $\Pi_z$ , the  $F_{\text{el}}$ -induced mixing induces large, opposite electric dipole moments in such a state pair. This in turn results in large linear shifts with respect to the applied electric field. Because no other states are degenerate with these two interacting levels, excitation to vibrator pairs in the  $n$ -mixing regime avoids unwanted state mixing effects that are characteristic of linear Stark states in low-magnetic-field systems.

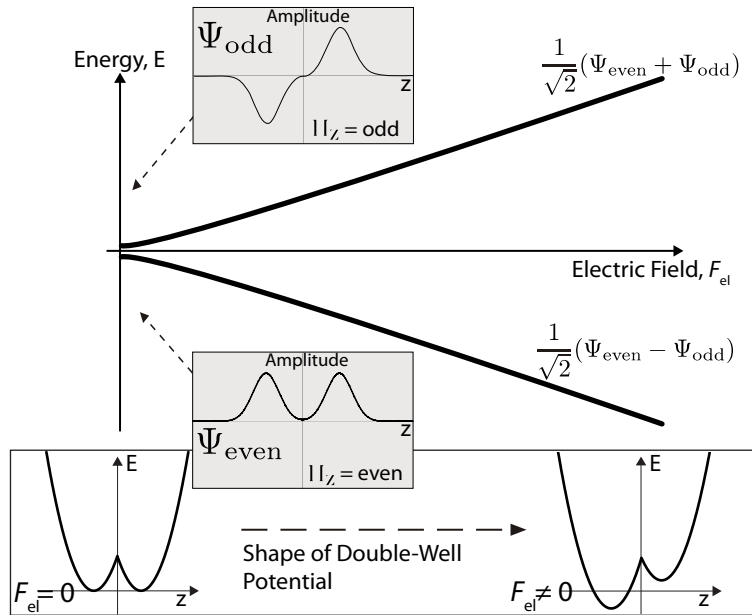


Figure 2.3: Electron in a one-dimensional, symmetric double-well potential perturbed by an electric field  $F_{\text{el}}$ . For  $F_{\text{el}} = 0$  the double-well system has discrete  $\Pi_z$  symmetry, which is lost when  $F_{\text{el}} \neq 0$ . As explained in the text, this simple model system mimics the essential properties of electric-field-coupled vibrator states of Rydberg atoms in strong magnetic and weak parallel electric fields.

The behavior of such electric-field-coupled pairs of vibrator states is analogous to that of pairs of states within a symmetric one-dimensional double-well potential, as illustrated in Fig. 2.3. Considering identical harmonic wells connected at  $z = 0$ , the oscillation frequency  $\omega_{\text{osc}}$  and its inverse, the density of states, are set by the particle mass and the force constant in the individual wells. The physical separation between the two wells determines how many sub-barrier levels each well holds. As sketched in Fig. 2.3, the sub-barrier states are grouped in near-degenerate pairs, with one state being an even and the other an odd superposition of the single-well states. The analogous states in the high-magnetic-field problem are the vibrator pairs of near-degenerate states, one having an elongated wavefunction along the  $z$ -axis that is even in  $\Pi_z$ , and the other an odd wavefunction. The wavefunction amplitude will also be primarily concentrated away from the central region (where the positive ionic core lies). The presence of an electric field  $F_{\text{el}}$  creates a relative energy shift between the wells, which lifts the near-degeneracy of the sub-barrier state pairs. When the electric-field-induced energy shift exceeds the tunneling frequency through the central barrier, the state energies become linear in  $F_{\text{el}}$  and the resulting wavefunctions become localized in one of the two individual wells (corresponding to symmetric and anti-symmetric 50/50 superpositions of the even- and odd-parity states). These characteristics are summarized in Fig. 2.3.

### 2.5.1 Gamow estimate

The tunneling-induced energy differences such pairs of states that lie beneath the energy level of the potential at  $z = 0$  can be estimated by  $\omega_{\text{osc}}$  times the Gamow factor [77]:

$$G = \sqrt{\frac{2m}{\hbar^2}} \int_a^b \sqrt{V(r) - Q} dr$$

$$P = e^{-2G}$$

Here,  $a, b$  are the limits of the classically forbidden region,  $V(r) - Q$  is the difference between potential and the energy of the particle, and  $P$  is the tunneling probability. The tunneling frequency is then  $\omega_{\text{tunnel}} = P\omega_{\text{osc}}$ . The energy splitting between a pair of states is defined as  $\Delta E_{\text{defect}} = 2 \times \hbar\omega_{\text{tunnel}}$ . For the double-well model, using a particle of one electron mass and elementary charge, a well curvature corresponding to  $\omega_{\text{osc}} \sim 2\pi \times 10$  GHz, and well minima at  $\pm 2000 a_0$  will give a system analogous to the behavior of Rydberg atoms in the  $n$ -mixing regime. The corresponding potential is then:

$$V(z) = \frac{1}{2} \hbar m \omega_{\text{osc}}^2 (|z| - z_0)^2$$

Using the Gamow factor gives, for a first estimate, a tunneling-induced splitting of  $\sim 10$  MHz for the ground state level pair, and in the presence of an electric field  $F_{\text{el}}$  the dipole moments are approximately  $\pm 2000 ea_0$ .

### 2.5.2 Numerical one-dimensional model

To further explore the essential physics of coupled vibrator states I present a numerical model for the case of the one-dimensional double-well system. Using the same factors as in the Gamow estimate above (a particle of  $m = m_e$ , a well curvature of  $\omega_{\text{osc}} \sim 2\pi \times 10$  GHz, and well minima at  $\pm 2000 a_0$ ) results in the energy level structure shown in Fig. 2.4. For these parameters, about three sub-barrier levels fit within each well. The ground state energy splitting  $\Delta E \approx 60$  MHz is quite small: the wavefunction penetration into the classically forbidden region of the central potential

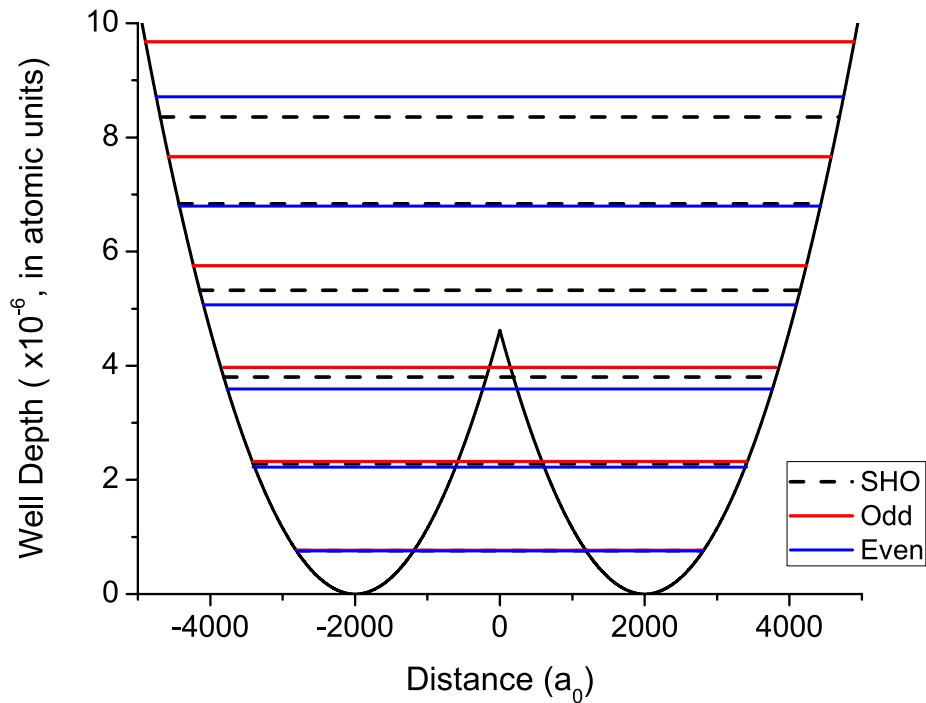


Figure 2.4: Numerical solution of the energy levels for the double-well problem, in the case of  $\omega_{\text{osc}} \sim 10$  GHz,  $z_0 = 2000 a_0$ , and  $m = m_e$ . The dashed black line shows the single-well energy levels, while the red/blue lines indicate the numerically calculated odd/even solutions for the double-well system. The energy defect becomes larger with increasing energy and penetration into the core region.

barrier about  $z \sim 0$  is almost negligible, and the two solutions closely match the symmetric and anti-symmetric superpositions of the ground-state wavefunction of a single well. Such a level pair is analogous to the case of near-degenerate vibrator pairs within the  $n$ -mixing regime; already at a small applied electric field  $F_{\text{el}}$  the  $\Pi_z$ -odd and  $\Pi_z$ -even states form symmetric and anti-symmetric linear combinations, generating large permanent dipole moments.

The numerically-calculated wavefunctions of this double-well problem are illustrated in Fig. 2.5. The energy splitting becomes much larger for each subsequent energy level as the wavefunctions penetrate further into the central barrier region. For energy levels that exceed the barrier height at  $z = 0$ , the effect of the central region becomes smaller with increasing energy, until the levels are separated by even

steps in energy, with alternating even/odd wavefunctions. For very high energies the problem reduces back to that of a simple harmonic well with the same frequency of oscillation.

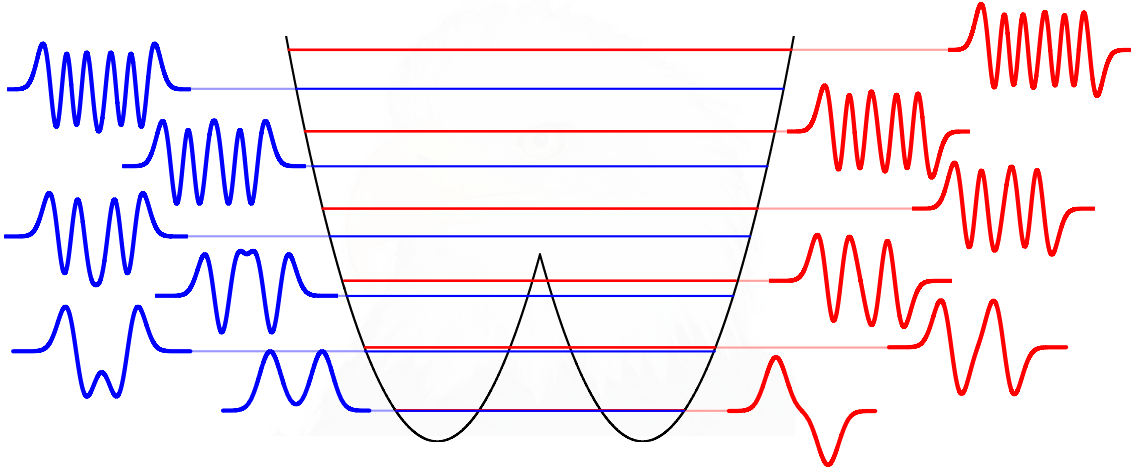


Figure 2.5: Numerically-calculated wavefunctions for the energy levels of the double-well system. The ground state solutions can be closely approximated by symmetric and anti-symmetric superpositions of the single-well ground state wavefunctions.

## 2.6 Rubidium ground and first excited states

Since our trap operates within a strong bias field of several Tesla, the energy structure of not only the Rydberg states but also the ground state and the trapping transition are also affected. The high-magnetic-field trap can be employed to trap either rubidium 85 or 87, the two most common isotopes. To trap the atoms, a two-level cycling transition from the 5S ground state to the intermediate 5P state is used. For both of these tightly-bound states, the effect of the applied magnetic field can simply be treated as a perturbation [78, 79]:

$$H' = Ah\mathbf{I} \cdot \mathbf{J} + g_J\mu_B\mathbf{J} \cdot \mathbf{B}_0 - g_I\mu_B\mathbf{I} \cdot \mathbf{B}_0 \quad (2.11)$$

Although at low fields  $\mathbf{F} = \mathbf{I} + \mathbf{J}$  is still a good quantum number and the energy

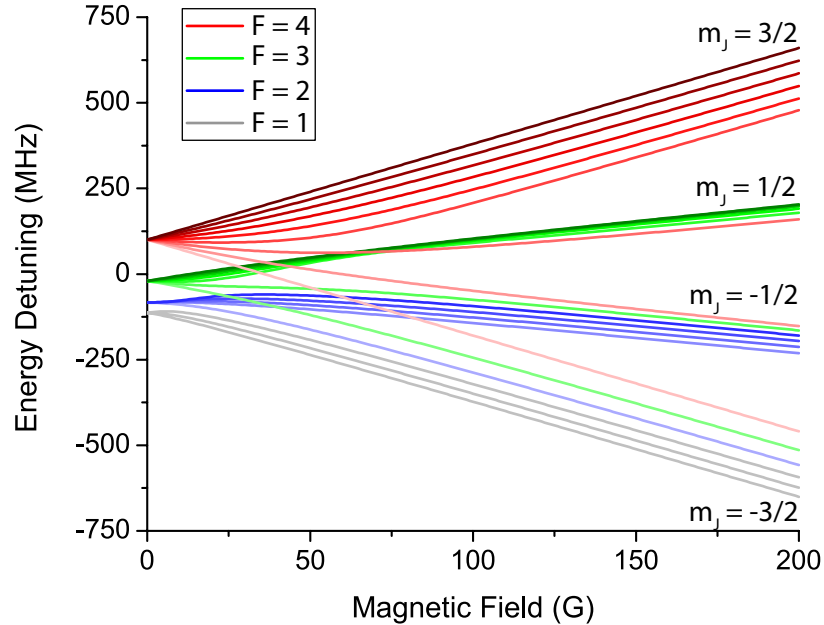


Figure 2.6:  $^{85}\text{Rb}$  hyperfine structure of the  $5\text{P}_{3/2}$  state within a magnetic field. In low-field conditions  $|F, m_F\rangle$  is a good basis, as indicated by the colors. As the magnetic field increases, the states pass through an intermediate region, until finally the  $I$  and  $J$  quantum numbers become decoupled, and the states are organized in groups of the same  $m_J$ .

splitting may be treated as  $H' = g_F \mu_B m_F B_0$ , already at magnetic fields values of  $\sim 100$  Gauss this is no longer a good basis. If  $F = I \pm 1/2$  the system may be described using the Breit-Rabi formula, while for a more general case the energy states of the sublevels can be found by re-diagonalizing the problem. This is shown above in Fig. 2.6, where the hyperfine structure for the  $5\text{P}_{3/2}$  state of  $^{85}\text{Rb}$  is plotted versus the applied magnetic field. At low fields the states are divided into groups of the same  $F$ , while at higher magnetic field values the  $I$  and  $J$  quantum numbers become increasingly decoupled. The complete hyperfine structure for the  $5\text{S}_{1/2}$  and  $5\text{P}_{3/2}$  states of  $^{85}\text{Rb}$  and  $^{87}\text{Rb}$  with respect to the applied magnetic field are detailed in Appendix B.

In the high magnetic field regime, the usual basis of stationary states  $\{|F, m_F\rangle\}$  is replaced by the basis  $\{|I, J, m_I, m_J\rangle\}$  as the magnetic field decouples the nuclear and



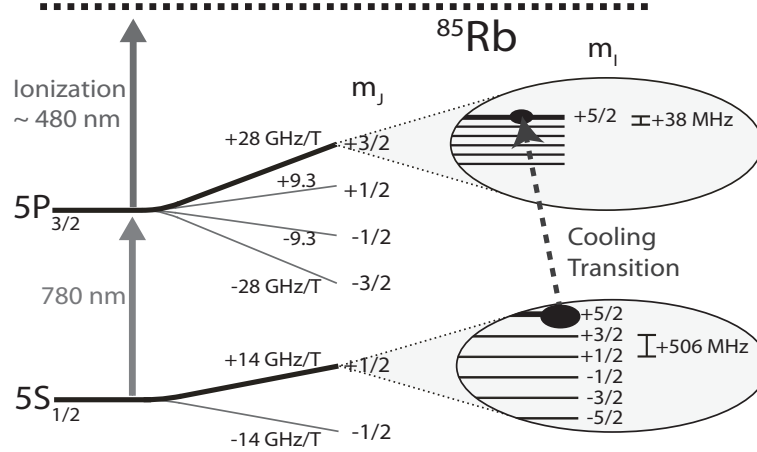


Figure 2.7: Cooling and trapping transition in  $^{85}\text{Rb}$ . Trapping occurs on the uppermost 5S – 5P transition; from  $5\text{S}|m_I = 5/2, m_J = 1/2\rangle \rightarrow 5\text{P}|m_I = 5/2, m_J = 3/2\rangle$ . This transition has a net shift of 14 GHz/T. The closest allowed transition would be  $5\text{S}|m_I = 3/2, m_J = 1/2\rangle \rightarrow 5\text{P}|m_I = 3/2, m_J = 3/2\rangle$ , which would be  $506 - 38 = 468$  MHz detuned from the trapping transition.

orbital angular momenta  $\mathbf{I}$  and  $\mathbf{J}$  ( $I = 3/2$  for  $^{87}\text{Rb}$ ,  $I = 5/2$  for  $^{85}\text{Rb}$ ). Throughout the rest of this thesis kets with integer numbers denote states  $\{|F, m_F\rangle\}$ , while kets with half-integer numbers denote states  $\{|m_I, m_J\rangle\}$ . In the Paschen-Back regime of high magnetic field this creates energy shifts and organizes the hyperfine structure as [44]:

$$\Delta W_{m_I, m_J} = \mu_B g_J m_J B_0 + A_{nl} m_I m_J. \quad (2.12)$$

For  $^{85}\text{Rb}$ , this results in a net shift of  $\sim 14$  GHz/T upon the trapping transition, while the  $5\text{S}_{1/2}$  and  $5\text{P}_{3/2}$  ( $m_J = 3/2$ ) hyperfine levels are separated by steps of 506 MHz and 38 MHz, respectively [80]. Figure 2.7 shows the resulting level structure for the states of interest. The laser cooling occurs on an almost perfect two-level system:  $5\text{S}_{1/2}|5/2, 1/2\rangle \rightarrow 5\text{P}_{3/2}|5/2, 3/2\rangle$  (wavelength  $\sim 780$  nm). The next-nearest allowed transition is to  $5\text{P}_{3/2}|5/2, 1/2\rangle$ . At  $B_0 = 2.6$  T, this transition is 48.6 GHz away with a resulting scattering rate of  $1 \times 10^{-3} \text{ s}^{-1}$  when the total intensity

of the six trap beams is  $I_{\text{TOT}} = 0.1 I_{\text{SAT}}$  ( $I_{\text{SAT}} = 1.6 \text{ mW/cm}^2$ ). Because of the low value of this scattering rate, repumper lasers are unnecessary.

In the case of  $^{87}\text{Rb}$ , the level structure is quite similar, as illustrated in Fig. 2.8.. Here  $I = 3/2$ , so there are only 4  $m_I$  sublevels for each  $m_J$ . The trapping transition ( $m_J = 1/2 \rightarrow m'_J = 3/2$ ) holds the same magnetic field dependence of  $\sim 14 \text{ GHz/T}$ . The splitting between the  $m_I$  sublevels are 1709 MHz and 127 MHz for the  $5S_{1/2}$  and  $5P_{3/2}$  ( $m_J = 3/2$ ) hyperfine levels, respectively [80].

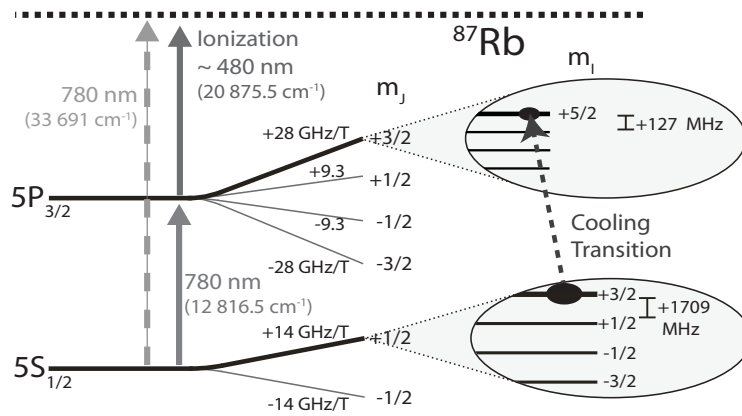


Figure 2.8: Cooling and trapping transition in  $^{87}\text{Rb}$ . Trapping occurs on the uppermost  $5S$ - $5P$  transition; from  $5S|m_I = 3/2, m_J = 1/2\rangle \rightarrow 5P|m_I = 3/2, m_J = 3/2\rangle$ .

## CHAPTER III

### The high-magnetic-field trap

#### 3.1 Trapping Apparatus

##### 3.1.1 Field Geometry

The high magnetic field trap confines low-field seeking atoms at a local field minimum within a large offset magnetic field of up to 3 T. The field topology is established by super-conducting coils in a Ioffe-Pritchard configuration [81]. The dipole coils are set slightly further apart than a standard Helmholtz pair so as to create a local minima in the axial direction. A second set of racetrack-shaped quadrupole coils are used to confine the atoms along the azimuthal directions. Figure 3.1 shows the trapping apparatus, while Fig. 3.3 provides a cut-out showing the geometry and relative placement of the magnetic field coils. The trap shape itself is governed by the magnetic potential,

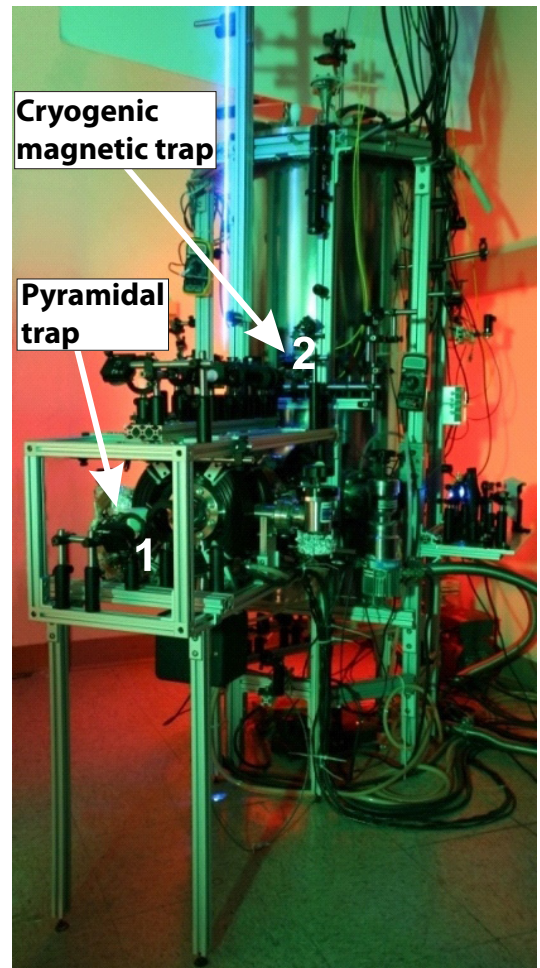


Figure 3.1: High magnetic field atom trapping apparatus. A pyramidal trap (1) injects a stream of cool Rb atoms into a cryogenic magnetic trap (2). The magnetic trap, formed by four superconducting coils, has a field minimum at 2.6 T.

as determined by the coil geometry and the applied currents. Near the trap center, the magnetic field is given by:

$$\vec{B}(\vec{r}) \simeq B_0(\beta x - \alpha xz, -\beta y - \alpha yz, 1 + \alpha z^2 - \frac{\alpha}{2}[x^2 + y^2]) \quad (3.1)$$

Here  $B_0$  is the central magnetic field, which is proportional to the dipole coil (D in Fig. 3.3) current, with a stability better than  $10^{-4}$  T. The factor  $\alpha$  is set by the coil geometry ( $\alpha = 22 \text{ m}^{-2}$ ), while  $\beta$  depends on the quadrupole coil (Q in Fig. 3.3) current. At the trap center the magnetic trapping potential is approximately harmonic in shape:

$$V(\vec{r}) \simeq \mu_z[B_0 + C_t(x^2 + y^2) + C_z z^2] \quad (3.2)$$

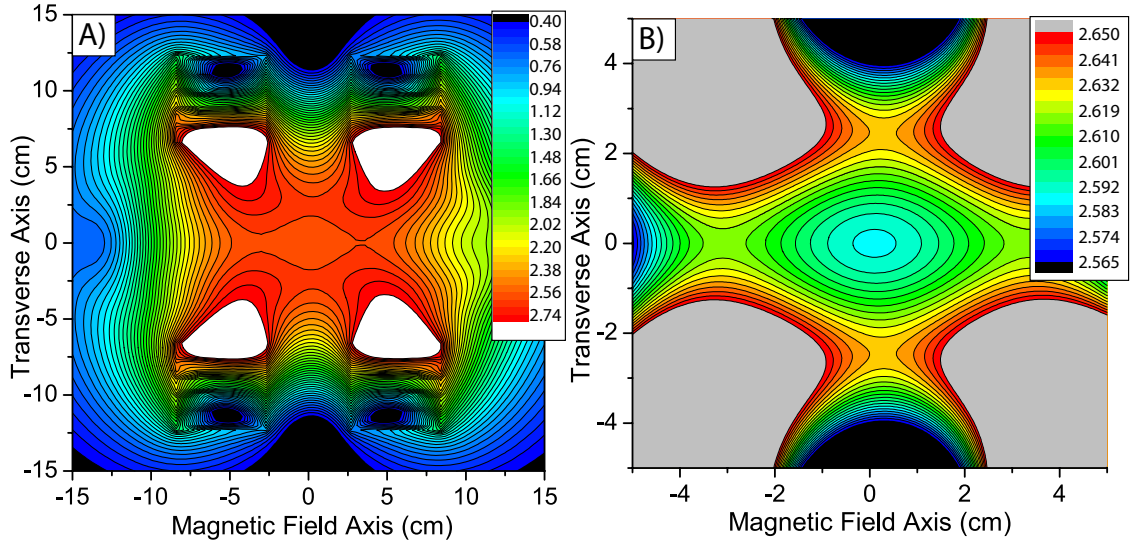


Figure 3.2: A) Contour plot of the magnetic field, with a central local magnetic field minimum of 2.59 T. B) Close-up of the central region, showing the local magnetic minimum and the depth of the potential well ( $\sim 300$  Gauss).

The factors  $C_t$  and  $C_z$  are the transverse and longitudinal magnetic field curvatures;  $C_t = B_0 \frac{\beta^2 - \alpha}{2}$  and  $C_z = B_0 \alpha$ . Further,  $\mu_z$  is the component of the magnetic dipole moment in the magnetic field direction. Under typical operating conditions, such as used in Figs. 3.5-3.9, these parameters are set to  $C_t = 130 \text{ T/m}^2$  and

$$C_z = 57 \text{ T/m}^2.$$

Figure 3.2 shows a contour plot of the magnetic field within the trapping apparatus, for  $B_0 = 2.59 \text{ T}$ . Here the resulting trap has an ellipsoidal geometry. The aspect ratio can be changed by either increasing or decreasing  $C_t$ , the transverse curvature parameter. For the typical operating values quoted above, at  $B = 2.59 \text{ T}$  the trap depth is  $\simeq 300 \text{ G}$ , corresponding to a temperature  $T = (\mu_B B)/k_B \simeq 22 \text{ mK}$ .

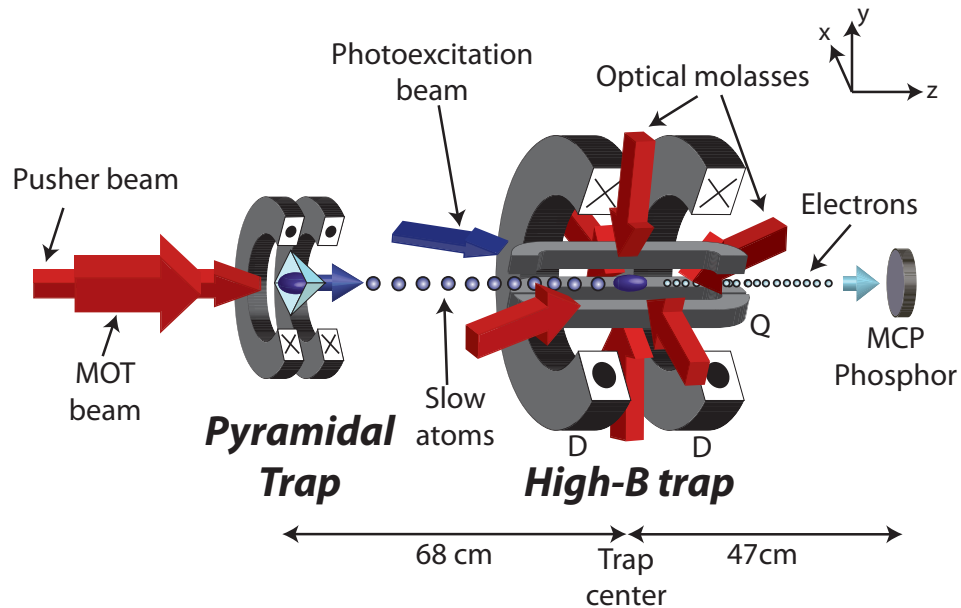


Figure 3.3: Schematic of the high-magnetic-field trapping apparatus. The high field trap is surrounded by a four-component electrode package, which allows for ionization of excited atoms and collection of the resultant electron signal upon a micro-channel plate, located outside of the high-field region.

### 3.1.2 Cold atom injection into the high-field region

Rubidium atoms are initially cooled and collected outside of the high-field region, using a pyramidal MOT [82, 83] set between a pair of magnetic-field coils to create the required field zero. Within a standard magneto-optical trap, atoms that drift away from the magnetic-field zero feel a restoring force via preferential scattering from the optical beam propagating back toward the center. The Zeeman shift causes this  $\sigma^-$  beam to be tuned toward the resonant condition, while the counter-propagating

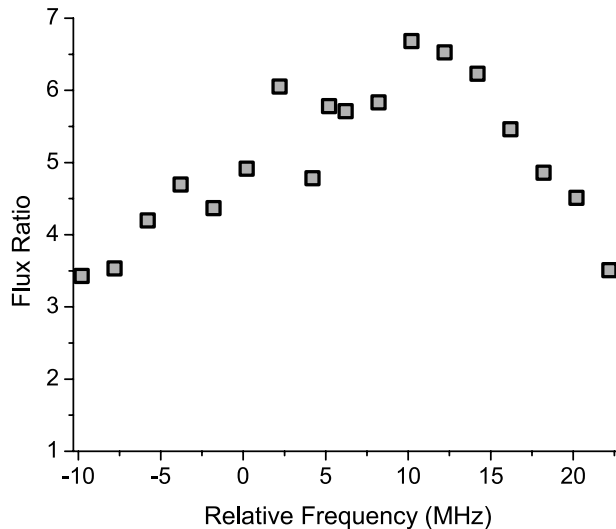


Figure 3.4: Effect of the pusher beam, measured through the observed flux ratio (as compared to the case with no pusher beam present) versus frequency detuning from the pyramidal MOT trapping transition beams.

$\sigma^+$  beam (that would expel the atoms) is detuned by the same mechanism. This has the additional effect of pumping the atoms into a high-field-seeking state, as the atoms preferentially scatter  $\sigma^-$  light. However, in the case of a pyramidal MOT, the small aperture at the apex of the pyramid removes a narrow section of the return  $\sigma^-$  beam. Since the atoms only see one incident beam along that axis, they are expelled out of the trap center and through the hole at the apex. The atoms scatter  $\sigma^+$  light despite the increasing detuning, and are optically pumped to the highest-lying sublevel of the  $5S_{1/2}$  ground state, as described in Sec. 2.6. For  $^{85}\text{Rb}$  this corresponds to the  $5S_{1/2}|m_I = 5/2, m_J = 1/2\rangle$  state, while for  $^{87}\text{Rb}$  this is the  $5S_{1/2}|m_I = 3/2, m_J = 1/2\rangle$ . In both cases, this is a low-field seeking state with  $1 \mu_B$  of magnetic moment. As shown in Fig. 3.3, a collimated pusher beam with a full width at half maximum (FWHM) intensity profile of 0.7 mm and with a frequency detuning +10.5 MHz above the MOT laser frequency is also applied to help direct the atoms from the MOT toward the high-field region. The resulting atom flux output is

profiled via an absorption measurement 15 cm downstream from the low-field MOT. The pusher beam increases the net flux out of the trap by a factor of  $\sim 7$ , resulting in a measured flux of  $5 \times 10^8 \text{ s}^{-1}$  and a full divergence angle of 50 mrad. Figure 3.4 shows the relation between the measured atom flux and frequency detuning of this pusher beam. It also raises the mean speed of the ejected atoms from  $\sim 10 \text{ m/s}$  to  $\sim 20 \text{ m/s}$ , with a root-mean-square spread of  $\sigma \sim 5 \text{ m/s}$ . This speed increase is necessary to reach the central region of the apparatus, as these low-field-seeking atoms lose kinetic energy when they climb the magnetic dipole potential and travel toward the high field trapping region:

$$g_J m_J \mu_B B = 1 \mu_B B = \frac{1}{2} m v^2 \quad (3.3)$$

For a field of 2.6 T only atoms with velocities greater than 18.5 m/s will reach the top of the magnetic dipole potential, so the pusher beam must be present in order to load atoms from the pyramidal MOT into the high magnetic field trap. Further information about the loading characteristics relating to the pusher or loading beams can be found in Appendix D.

### 3.1.3 High-Field Trapping

The incident atomic beam density at the location of the high-field trap is  $\sim 10^{10} \text{ m}^{-3}$ . Within this high-field trapping region, these cold atoms are recaptured at the location of the local magnetic-field minimum using a six-beam optical molasses [81]. At an operating field of 2.6 T, the trapping transition has a net +36.4 GHz Zeeman shift from the zero-field frequency resonance. With no readily available atomic reference line, the high-field cooling laser is instead locked to a pressure-tuned Fabry-Pérot interferometer [84] that can be pressure-tuned so as to scan

and control the laser frequency. This molasses is frequency-tuned to act upon the  $5S_{1/2}|5/2, 1/2\rangle \rightarrow 5P_{3/2}|5/2, 3/2\rangle$  transition (in the case of  $^{85}\text{Rb}$ ) for the magnetic field value  $B_0$  of the local minimum, as set by the coil currents. This is a  $\sigma^+$  transition, and because of the large frequency detuning induced by the magnetic field the atoms will be transparent to the other polarization components. Along the magnetic field axis the two counter-propagating molasses beams are linearly polarized (and thus equal parts  $\sigma^+$  and  $\sigma^-$ ), and their intensities matched through polarization optics that control the relative power in each beam. For the two transverse directions, the molasses beams are applied with linear polarization at a 45 degree angle relative to the magnetic field axis, resulting in equal parts  $\pi$  and  $\sigma$  light. Each of these two transverse beams is then retro-reflected back through the chamber to create the counter-propagating component. To account for intensity losses (for example, from the optical components and the chamber windows) the polarization of each retro-reflected beam is rotated so as to increase the  $\sigma$  component and match the incident intensity.

The performance of the high-field atom trap can be monitored through two different methods. The cryogenic setup, the coil geometry as well as the electrodes available for charged-particle manipulation and electric field control are conducive to using photo-ionization and charged-particle detection with a micro-channel plate (MCP) as the primary method of monitoring and analyzing the trapped atoms. The MCP has a detection efficiency of  $\lesssim 50\%$  (manufacturer technical note [85]). The trapped atoms sit within a four-component electrode package, so the atoms may be photo-ionized through the intermediate 5P state with a beam of 479 nm light. The resulting free electron signal can then be detected via collection onto the MCP, giving both temporal count resolution as well as spatial resolution from a phosphor screen



located directly behind the MCP.

The second detection method is to monitor the trap performance via fluorescence imaging of the atoms as they are illuminated by the cooling light on the 5S-5P trapping transition. Since the superconducting coil helium bath requires a high degree of thermal radiation shielding, the optical access ports are quite small (each port has a diameter of  $\sim 1$  cm). The radiant heat load on the helium cryostat from the 300 K background comes from a total surface area of  $\sim 10$  cm<sup>2</sup>, which gives an estimated helium loss rate of 1.1 L/hour [86]. This is close to our measured loss rate of 1.5 L/hour.

Each individual optical port only subtends a solid angle of  $\sim 0.0006$  steradian with respect to the trap center. To compensate for this lack of optical access, a high-sensitivity cooled EMCCD camera (ANDOR iXon+ [87]) with a maximal quantum efficiency of greater than 80 % at the 780 nm fluorescence wavelength is used for the trap imaging, along with an optical imaging system to collect the entire available solid angle. Several additional details on the trapping apparatus can be found in Ref. [33].

## 3.2 Trapping Characteristics

### 3.2.1 Lineshape

A distinctive feature of the trap is its asymmetric spectroscopic lineshape, obtained via a frequency scan of the  $5S_{1/2}|5/2, 1/2\rangle \rightarrow 5P_{3/2}|5/2, 3/2\rangle$  cooling transition. As the red-detuned laser approaches the resonant frequency at the bottom of the potential well, the scattering rate increases and greater numbers of atoms are cooled and localized. However, when the frequency sweeps across to the blue-detuned side of the resonance relative to the magnetic field at the location of the well minimum, any atom population at this central location undergoes heating. The well is

quite shallow ( $\sim 300$  G), meaning that any appreciable amount of heating will cause atoms to be forcibly driven out of the magnetic trapping region. As can be seen in Fig. 3.5, this behavior results in highly asymmetric lineshapes. Here, the horizontal axis is the frequency offset  $\nu_{\text{ofs}}$  of the molasses laser from the 5S-5P resonance at the trap center (local magnetic field minimum). The full width at half maximum (FWHM) of the line has been measured to be as little as 3.5 MHz, substantially less than the natural linewidth of the cooling transition (6 MHz). This contrasts with the signal due to the hot atomic beam, which is much weaker and broader (circles in Fig. 3.5, measured via photo-ionization). The properties of laser cooling in the high-magnetic-field trap are similar to that of Doppler cooling of an ion within an external potential such as an RF trap [88].

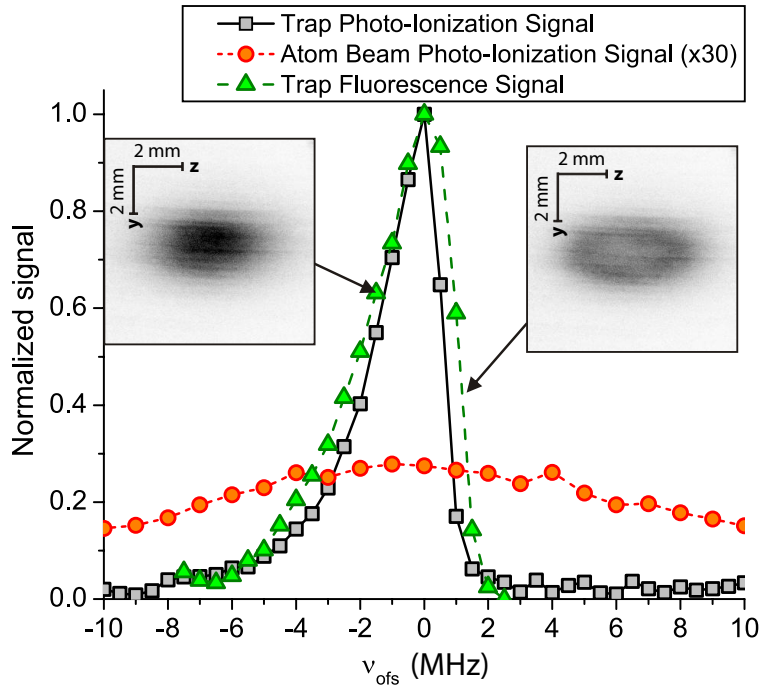


Figure 3.5: Signal obtained by direct excitation out of the incident atomic beam (circles,  $\times 30$ ) and normalized trap signal versus frequency offset,  $\nu_{\text{ofs}}$ , of the cooling laser for a fully optimized trap (squares and triangles). For the atomic beam, the signal is from photo-ionization of 5P atoms. For the optimized trap I show both ionization and fluorescence signals. The trap shows a narrow linewidth (FWHM  $< 4$  MHz) and highly asymmetric character. The two insets are fluorescence images, with the trapping light frequency slightly red or blue-detuned. Atoms are cooled onto a shell by setting the frequency just above the peak trapping condition.

The left inset picture of Fig. 3.5 shows a fluorescence image of the trap under optimal trapping conditions, with the laser frequency just below the transition resonance at the location of the trap center. Similar images have been taken along the  $z$ -axis, to ensure that the  $x$  and  $y$  transverse trap extents are symmetric. Since this frequency offset varies with the magnetic field, the molasses laser appears increasingly red-detuned away from the trap center. In this case, stable and relatively dense traps with approximately Gaussian density distributions are achieved. With a bias magnetic field of  $B_0 = 2.6$  T, and a corresponding trap curvature of  $C_t = 130$  T/m<sup>2</sup> and  $C_z = 57$  T/m<sup>2</sup>, the trap is elliptically-shaped with a long axis FWHM of 4.0 mm (corresponding to a root-mean-square spread of  $\sigma_z = 1.7$  mm) along the direction of the dipole field and a short axis FWHM of 2.2 mm ( $\sigma_t = 0.9$  mm). Under optimal conditions the trap can contain  $\sim 2 \times 10^7$  atoms, yielding atom densities of up to  $\sim 10^9$  cm<sup>-3</sup>.

### 3.2.2 Unusual trap geometries

If the molasses laser frequency is tuned such that it is just above the resonant frequency for  $B_0$ , there is a stable configuration in which atoms remain confined to a shell surrounding the bottom of the trap, but are driven out of the central region. To interpret this behavior, note that the atom-field detuning depends on atom position within the trap, and is given by:

$$\nu_{\text{AF}} = \nu_{\text{ofs}} - (|\vec{B}(\vec{r})| - B_0) \times 1.4 \text{ MHz/Gauss} \quad (3.4)$$

This value is negative when the molasses laser is red-detuned relative to the local 5S-5P transition frequency. For positive values of  $\nu_{\text{ofs}}$ ,  $\nu_{\text{AF}}$  takes the value of 0 on an approximately ellipsoidal shell, centered around the bottom of the trap. If

$\nu_{\text{ofs}} \sim +1$  MHz, this situation leads to a stable three-dimensional density profile that peaks on the surface of that ellipsoidal shell. Within this shell the molasses laser is blue-detuned ( $\nu_{\text{AF}} > 0$ ), and atoms are heated and expelled from the interior of the shell. Outside of the shell the molasses laser is red-detuned ( $\nu_{\text{AF}} < 0$ ), resulting in laser cooling. In addition, the magnetic force due to the magnetic dipole potential of the atoms in the inhomogeneous magnetic field provides a restoring force that is always directed toward the center of the trap. The combination of these three characteristics creates a tenuous balance in which the atoms are cooled and confined to the surface of the shell, with some radial spread. The right inset picture of Fig. 3.5 shows this shell structure. Stable atom shells are observed over a trap laser frequency range of  $\sim 1$  MHz. As the molasses laser is further scanned up in frequency, the ellipsoidal shell defined by the resonance condition  $\nu_{\text{AF}} = 0$  moves further out from the trap center. For  $\nu_{\text{ofs}} \gtrsim 2$  MHz the heating due to the molasses laser inside the shell becomes overwhelming, and atoms gain enough kinetic energy to completely escape the trap as they are expelled from the central region. These observed shell structures have been reproduced in simulations, as detailed in Sec. 3.3.

### 3.2.3 Cooling transition spectroscopy

While for both  $^{85}\text{Rb}$  and  $^{87}\text{Rb}$  the trapping transition is non-degenerate, there do still exist other hyperfine states within an energy range of several GHz. Figure 3.6 shows the trap performance (i.e. the trapped atom signal) for  $^{85}\text{Rb}$  as the cooling laser frequency is scanned over 600 MHz in steps of 2 MHz at high intensity ( $I_{\text{TOT}} > 5 I_{\text{SAT}}$ ). The strong, sharper resonance (FWHM  $\sim 20$  MHz) on the left is the desired  $5S_{1/2}|5/2, 1/2\rangle \rightarrow 5P_{3/2}|5/2, 3/2\rangle$  transition. Since their  $m_I$  and  $m_J$  components are maximal, both  $5S_{1/2}|5/2, 1/2\rangle$  and  $5P_{3/2}|5/2, 3/2\rangle$  states do not carry any hyperfine-induced admixtures of other magnetic sublevels. Hence, the transition between these

two states is closed and suitable for atom trapping. This becomes evident when reducing the total molasses intensity to  $I_{\text{TOT}} = 0.1 I_{\text{SAT}}$  (corresponding to an intensity of  $I_1 \sim 0.02 I_{\text{SAT}}$  per beam), as the left feature in Fig. 3.6 becomes very narrow (black line, same data as in Fig. 3.5).

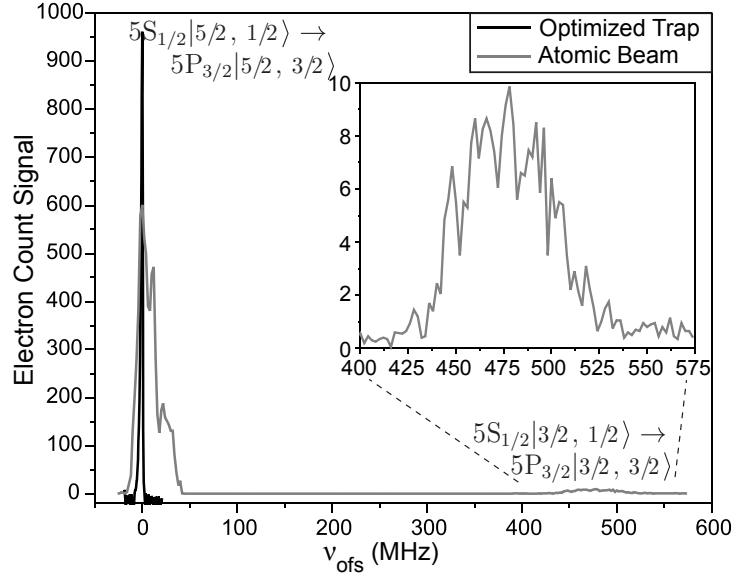


Figure 3.6: Measurement of frequency spacing and trapping behavior for two  $m_I$  sublevels in  $^{85}\text{Rb}$ . The gray curve, taken at high molasses intensity, shows the strongly broadened trapping transition  $5S_{1/2}|5/2, 1/2\rangle \rightarrow 5P_{3/2}|5/2, 3/2\rangle$  on the left, as well as the transition  $5S_{1/2}|3/2, 1/2\rangle \rightarrow 5P_{3/2}|3/2, 3/2\rangle$  on the right. The inset shows a magnification of the  $5P_{3/2}|3/2, 3/2\rangle$  signal, peaked at 476 MHz. For comparison, the black line shows the trapping transition under optimal low-intensity trapping conditions (not to scale).

The faint broad signal (FWHM $\sim$ 50 MHz) on the right results from excitation out of the incident atomic beam on the  $5S_{1/2}|3/2, 1/2\rangle \rightarrow 5P_{3/2}|3/2, 3/2\rangle$  transition. The line spacing is measured to be 476 MHz, with a statistical uncertainty of  $\pm 1$  MHz. Considering systematic uncertainties, which include non-linearities of the Fabry-Pérot scan and the different distributions of trapped atoms and atomic beam atoms within the magnetic trapping potential, the measurement agrees reasonably well with the expected value of  $A_{5S_{1/2}}(\Delta m_I)(1/2) - A_{5P_{3/2}}(\Delta m_I)(3/2) = 468$  MHz. This second peak is both broad and weak for two reasons. First, the pyramidal trap mostly

emits atoms in the  $5S_{1/2}|3, 3\rangle$  state, which is identical to the state  $5S_{1/2}|5/2, 1/2\rangle$  at the location of the high magnetic field trap, corresponding to the left peak in Fig. 3.6. The pyramidal trap emits relatively few atoms in the  $5S_{1/2}|3, 2\rangle$  state. This state connects to the  $5S_{1/2}|3/2, 1/2\rangle$  state, which produces the signal about 476 MHz in Fig. 3.6. Second, the  $5S_{1/2}|3/2, 1/2\rangle$  state carries a weak admixture  $\varepsilon_1 5S_{1/2}|5/2, -1/2\rangle$  due to residual hyperfine coupling. Similarly, the corresponding excited state is  $5P_{3/2}|3/2, 3/2\rangle + \varepsilon_2 5P_{3/2}|5/2, 1/2\rangle$ . As shown in Fig. 3.7, in the case of  $^{85}\text{Rb}$  the calculated coefficients are  $\varepsilon_1 \approx 1 \times 10^{-2}$  and  $\varepsilon_2 \approx 1 \times 10^{-3}$  at 2.6 T. Since  $5P_{3/2}|5/2, 1/2\rangle$  opens up a decay channel into  $5S_{1/2}|5/2, -1/2\rangle$ , which is an anti-trapped state, one would not expect any trapping on this transition. In fact, careful observation revealed no indication of atom trapping on the right line in Fig. 3.6; the signal disappears immediately when the incident atom beam is blocked, and diminishes correspondingly as the high-field molasses beam intensity is lowered. Similar considerations apply to all other magnetic sublevels  $5S_{1/2}|m_I \leq 3/2, m_J = 1/2\rangle$ , which cannot be trapped. For high molasses power intensities, sparse counts have been observed at laser frequencies corresponding to the lower  $m_I$  sub-levels, but again no trapping signal is observed.

For  $^{87}\text{Rb}$  the trapping transition  $5S_{1/2}|3/2, 1/2\rangle \rightarrow 5P_{3/2}|3/2, 3/2\rangle$  bears the same characteristics as the trapping transition of  $^{85}\text{Rb}$ . However, the next-higher transition of  $^{87}\text{Rb}$ ,  $5S_{1/2}|1/2, 1/2\rangle \rightarrow 5P_{3/2}|1/2, 3/2\rangle$ , is 1.6 GHz detuned and, is barely detectable. For the case of  $^{87}\text{Rb}$  the mixing parameters  $\varepsilon_1$  and  $\varepsilon_2$  are about a factor of 3 larger than in  $^{85}\text{Rb}$ , and so the optical-pumping rates into untrapped states are correspondingly higher.

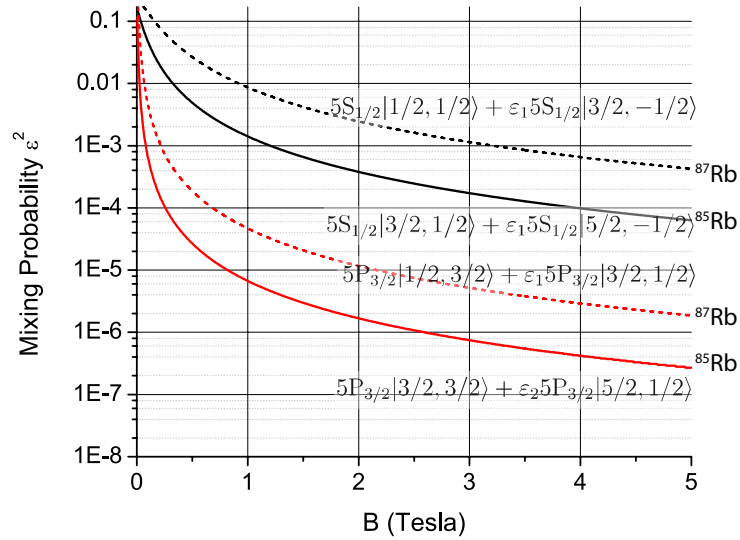


Figure 3.7: Mixing fraction probabilities ( $\varepsilon^2$ ) versus magnetic field, for  $^{85}\text{Rb}$  (solid lines) and  $^{87}\text{Rb}$  (dashed lines) isotopes. The next-highest  $m_I$  states for the  $5S_{1/2}$  ground state (black) and  $5P_{3/2}$  excited state (red) are shown. The indicated kets are written as  $|m_I, m_J\rangle$ .

### 3.2.4 Trap Temperature

Though the largest atom numbers are attained with the molasses frequency on resonance, a slight red detuning produces a colder trap temperature. Fluorescence images at a detuning of -1.5 MHz show that with  $C_t = 130 \text{ T/m}^2$  and  $C_z = 57 \text{ T/m}^2$  the trap is cigar-shaped, with a long axis FWHM of 4.0 mm (corresponding to a root-mean-square spread of  $\sigma_z = 1.7 \text{ mm}$ ) along the direction of the dipole field and a short axis FWHM of 2.2 mm ( $\sigma_t = 0.9 \text{ mm}$ ). A measurement of the atom temperature can be extracted by assuming that the fluorescence images are approximately identical with the underlying atom density distributions. This assumption is validated by simulations conducted to investigate the trapping behavior, described in Section 3.3. This in turn allows one to calculate the average potential energy of the atoms in the trap. Based on the virial theorem, kinetic and potential energies in a near-harmonic trap should be equal, and the atom cloud temperature can be determined via the density distributions:

$$n(x) = n_0 \exp\left[-\frac{y^2}{2\sigma_x^2}\right] = n_0 \exp\left[-\frac{\mu_B B_0 (\beta - \alpha) x^2}{2k_B T}\right] \quad (3.5)$$

$$n(z) = n_0 \exp\left[-\frac{z^2}{2\sigma_z^2}\right] = n_0 \exp\left[-\frac{\mu_B B_0 \alpha z^2}{k_B T}\right]$$

As shown in Fig. 3.8, the observed temperature is of  $\sim 220 \mu\text{K}$  along the  $z$ -axis (axial direction), and  $\sim 150 \mu\text{K}$  in the transverse  $x$  and  $y$  directions.

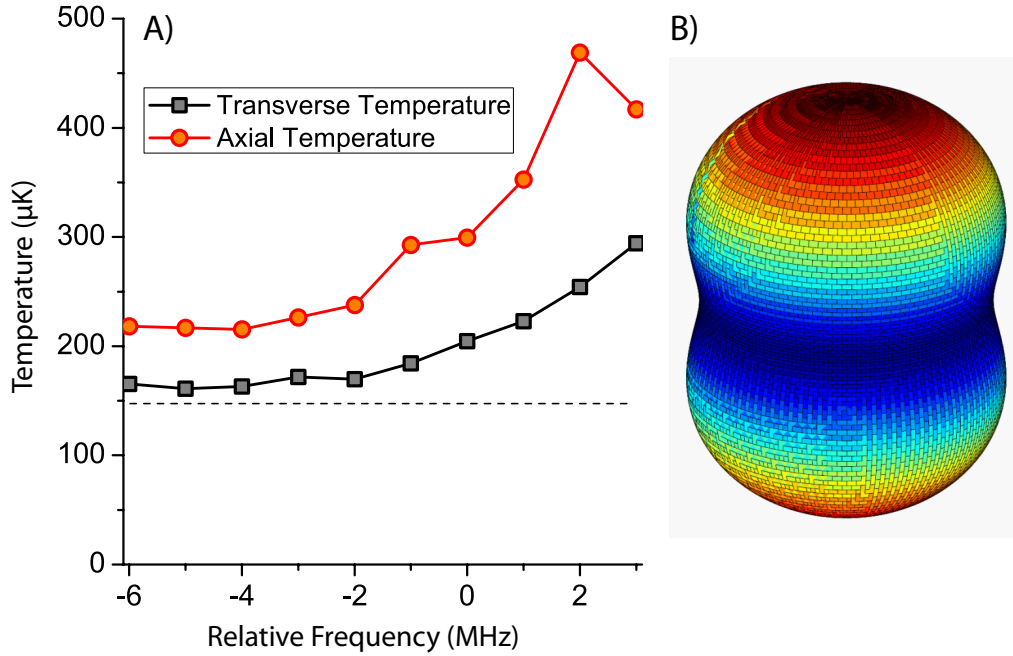


Figure 3.8: A) Trap temperatures, derived from fits to fluorescence images, versus the molasses laser frequency. Here 0 MHz corresponds to the laser frequency being on resonant for the bottom of the potential well. B) Representation of the  $1 + \cos^2(\theta)$  spontaneous emission pattern.

To explain the temperature difference between the axial and transverse directions, note that spontaneous emission on the cooling transition  $5S_{1/2}|5/2, 1/2\rangle \rightarrow 5P_{3/2}|5/2, 3/2\rangle$  is circularly polarized. The fluorescence has a  $|\Delta m| = 1$  dipole emission pattern of  $1 + \cos^2(\theta)$ , where  $\theta$  is the polar angle relative to the magnetic field. Consequently, the observed elevated axial temperature is expected. The axial and transverse temperatures consistently differ from each other, showing that atom collision rates are too small to allow for complete thermalization between the axial and



transverse degrees of freedom.

### 3.2.5 Trap Lifetime

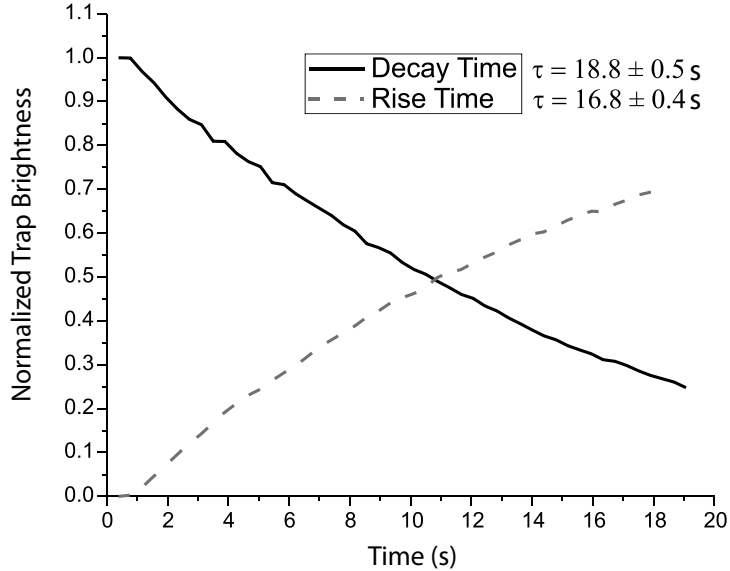


Figure 3.9: Trap decay and loading behavior, taken by spatial integration of the fluorescence signal recorded with the CCD camera. Time  $t = 1$  s corresponds to the atomic beam being suddenly blocked or unblocked. Fits to these curves give a  $1/e$  lifetime of 18.8 s and a  $1/e$  rise time of 16.8 s.

The high-field atom trap exhibits a long molasses lifetime. Figure 3.9 shows a typical measurement for  $C_t = 130$  T/m<sup>2</sup> and  $C_z = 57$  T/m<sup>2</sup> with a low molasses intensity of  $I_1 = 0.02 I_{\text{SAT}}$  per beam, where the trap's  $1/e$  lifetime (with no incoming flux of atoms) approaches 20 s. The loading behavior shows a similar timescale. These characteristic times have been observed to reach upward of 30 s under optimal conditions.

The observed characteristic times can be compared with two fundamental limits. One is due to transfer into the  $5S_{1/2}|5/2, -1/2\rangle$  state via scattering through the far-detuned  $5P_{3/2}|5/2, 1/2\rangle$  state. At  $B_0 = 2.6$  T and total beam intensity  $I_{\text{TOT}} \leq 0.1 I_{\text{SAT}}$ , off-resonant scattering is estimated to lead to  $1/e$  lifetimes of 500 s

or greater. Further, the effect of collisions with background gas atoms is measured by suddenly turning the molasses light off and monitoring the atom number as a function of waiting time. Resulting observations, shown in Fig. 3.10, give  $1/e$  magnetic-trapping lifetimes due to background gas collisions approaching 200 s.

When the molasses beams are applied to the trapping region and the trap operation is fully optimized, the experimentally-observed lifetimes ( $\tau = 20 - 30$  s) are considerably less than both the limit due to off-resonant scattering events, and the background gas lifetime. Beam imperfections must therefore play a larger role in the atom loss rate than either off-resonant scattering or background gas collisions. Possible beam imperfections include overlap misalignment near the edges of the beams, minor intensity and polarization drifts, and diffraction at the vacuum windows.

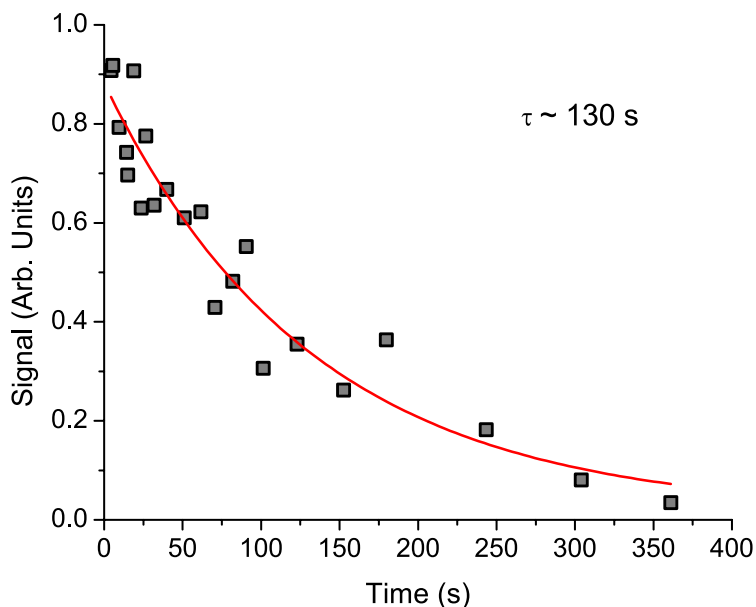


Figure 3.10: Lifetime of the atom trap. Here at  $t = 0$  the atom injection into the high-field region is suddenly turned off and all incident light is blocked. To measure the number of atoms, the molasses beams are suddenly unblocked, and the resultant signal instantaneously measured. This cycle is then repeated to produce this series of measurements. Here we see a lifetime of  $\tau \simeq 130$ . The highest lifetimes recorded were  $\sim 200$  s.

The observed lifetime for cooled atoms in the dark magnetic trap ( $\sim 200$  s) can

be compared to the calculated lifetime due to collisional losses. One possible loss source is from the hot effusive Rb beam flux that enters into the cold chamber via outgassing from the pyramidal MOT. The resulting collision rate can be calculated [89]:

$$\begin{aligned}\Gamma &= I\sigma \\ I &= \left(\frac{n_{\text{at}}\bar{v}}{4}\right) S_1 \frac{\cos(\theta)}{\pi L^2}\end{aligned}\tag{3.6}$$

Here,  $\Gamma$  is the collision or loss rate,  $I$  the effusive beam flux, and  $\sigma$  the cross-section ( $\sigma = 5 \times 10^{-18} \text{ m}^2$ ) for cold Rb-Rb collisions [90, 91]). The other parameters are the number density  $n_{\text{at}}$ , the mean speed  $\bar{v}$ , the orifice or aperture area  $S_1$ , and the distance  $L$ . In the case of our apparatus, the pyramidal primary MOT has a fairly large number pressure resulting in a high number density  $n_{\text{at}} = 3 \times 10^{15} \text{ m}^{-3}$ . However, the small aperture size (of diameter  $\sim 2 \text{ mm}$ ) and large distance from the trap ( $L = 0.68 \text{ m}$ ) result in an almost negligible loss rate, with  $1/\Gamma_{\text{pyr}} \approx 4 \times 10^5 \text{ s}$ .

The central 4 K chamber does have several much larger apertures to allow for optical access. In all, there are ten openings of diameter  $d \sim 1 \text{ cm}$ . Because of this, the high-field cold atom trap is subjected to incoming hot atoms from all directions, resulting in an increased loss rate. These losses will occur through background gas collisions. Taking  $\sigma_{\text{Rb-N}_2} = 2 \times 10^{-18} \text{ m}^2$  with 300 K atoms incident from a region with  $P \approx 10^{-10} \text{ Torr}$ , the resulting loss rate gives  $1/\Gamma_{\text{pyr}} \approx 300 \text{ s}$ . This rough estimate is consistent with our observed optimal magnetic lifetimes of  $\sim 200 \text{ s}$ .

### 3.2.6 Dependence on magnetic field parameters

The aspect ratio of the atom trap can be modified for a constant magnetic field  $B_0$  at the trap center by varying the quadrupole coil current. The general trap shape

follows our expectations based on the field geometry. Figure 3.11 shows that it is possible to produce a narrower trap by increasing the quadrupole current (and  $C_t$ ). Conversely, decreasing the quadrupole current generates a more spherical trap. As shown in the graph inset of Fig. 3.11, decreasing the transverse curvature significantly depletes the trap by reducing its characteristic lifetime. This lifetime reduction becomes more severe as the trapped atoms increasingly sample beam imperfections near the outer edges of the beams. The viability of this hypothesis can be tested by intentionally introducing intensity imbalances of as little as 1-2 % in the axial molasses beams. Doing so (in both the experiment as well as in the numerical simulations in Sec. 3.3) shows that such small imbalances already causes atom loss and trap depletion. Hence, light intensity balance is much more crucial for this trap than it is for MOTs.

The magnitude of the dipole field  $B_0$  also has a strong effect on the trap lifetime. Figure 3.12 shows lifetimes measured for a range of  $B_0$ , for both  $^{85}\text{Rb}$  and  $^{87}\text{Rb}$ . For each individual data point, the aspect ratio of the trap was held constant by proportionally adjusting the quadrupole field. Despite some variation of the trap lifetime and stability, the trend clearly is that the trap lifetime increases with the magnetic field. Since the temperature does not significantly depend on  $B_0$ , the lifetime increase observed by increasing  $B_0$  must be attributed to the reduction in spatial extent of the trap. With a reduced spatial extent, the atoms sample fewer molasses beam imperfections, leading to increased lifetimes. Conversely, a lower  $B_0$  leads to sampling of a greater area of the optical trapping beams, where beam imperfections in the edges will result in shorter lifetimes. If there were no imperfections, the lifetime would be limited by off-resonant scattering through the state  $5P_{3/2}|m_I = 5/2, m_J = 1/2\rangle$ . The off-resonant excitation rate scales as the inverse-square of the detuning, that

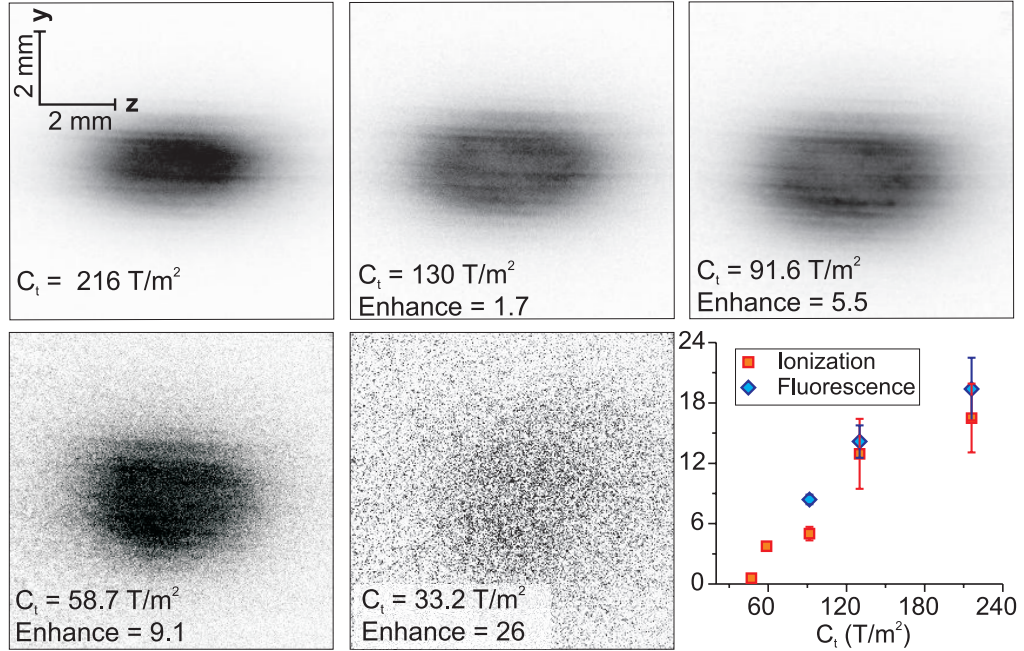


Figure 3.11: Fluorescence images of the high magnetic field trap at 2.6 T for different transverse field conditions. Bottom right: measured trap lifetime as a function of the transverse trap curvature  $C_t$ , for both photo-ionization and fluorescence measurements. As  $C_t$  is raised the trap becomes increasingly confined toward the central axis, and the trap lifetime (and the number of trapped atoms) increases. For clarity images taken at small values of  $C_t$  are rendered using the indicated brightness enhancement factors.

in turn scales with the magnetic field. Hence in the absence of beam imperfections one would observe a lifetime proportional to  $B_0^2$ . The fact that this  $B_0^2$  scaling is not observed reiterates the point that beam imperfections and asymmetries are the dominant loss mechanisms of the high-field atom trap.

### 3.3 Trajectory Simulations

To further study the trapping characteristics I have performed numerical Monte Carlo trajectory simulations of atoms in the system. The magnetic trap shape is simulated with a harmonic well of axial curvature  $C_z = 57 \text{ T/m}^2$  and transverse curvature  $C_t = 130 \text{ T/m}^2$ , corresponding to typical experimental settings. The optical beams within the trapping area are mimicked by applying a single-beam light intensity of  $I_1 = 0.02 I_{\text{SAT}}$  along each axis, shaped as a top-hat profile of radius

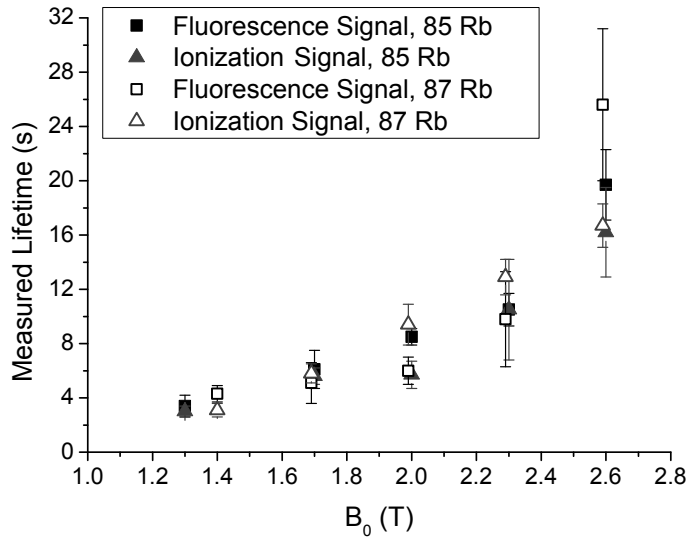


Figure 3.12: Trap lifetime versus magnetic field  $B_0$  for both Rb isotopes. Measurements were taken both with photo-ionization and fluorescence detection techniques. Errors bars represent the standard deviations of series of 2-7 measurements. For clarity, data taken at identical values of  $B_0$  are slightly offset from each other along the  $B_0$ -axis.

$r = 3.5$  mm (corresponding to the experimental aperture sizes). As only circularly polarized components of the light field interact with the two-level system, recoil from scattering events is set to follow a circular-light dipole emission pattern, proportional to  $1 + \cos^2(\theta)$ . The time step in the simulation is chosen to be  $0.5 \times 10^{-6}$  s; short enough that even for the maximal scattering rate at zero effective detuning the probability of a scattering event occurring within a single time step is still much less than one. In order to account for the experimentally observed trap loss I introduce an empirical decay rate of  $0.1 \text{ s}^{-1}$  in the simulation. The incident atomic beam is simulated by a flux of  $500 \text{ s}^{-1}$  atoms entering the region of interest through an aperture of radius 3.5 mm, located at a distance of  $z = 2$  cm from the trap center. The axial velocity distribution for atoms entering the trapping region is set to a homogeneous distribution from 0 to 5 m/s. The transverse velocity has a Gaussian distribution with  $\sigma = 0.25$  m/s, consistent with a temperature of  $\sim 1$  mK. Variations to the input parameters of the incident atomic beam do not significantly affect the

simulation results.

### 3.3.1 Frequency dependence

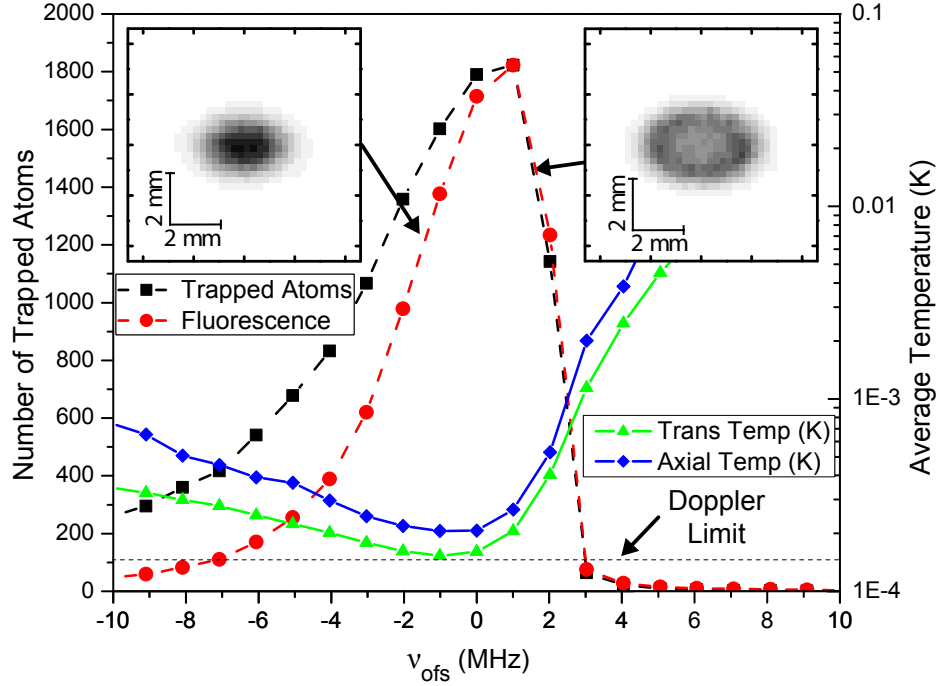


Figure 3.13: Simulated steady-state number of trapped atoms (squares, left axis), fluorescence signal (circles, arbitrary units) and atom temperature (diamonds and triangles, right axis, log scale) versus molasses laser frequency offset,  $\nu_{\text{ofs}}$ , for a constant input flux of atoms into the trapping region. Trapping is asymmetric in character with respect to frequency. The transverse temperature also attains lower limits than the axial temperature. The displayed simulated fluorescence images are analogous to the ones in Fig. 3.5, and demonstrate the same characteristic behavior.

The results of the simulations reproduce the experimentally observed trap behavior. To determine the trapping efficiency as a function of molasses beam frequency, the resulting simulated number of atoms within the trapping volume is calculated as a function of the frequency detuning. The trapping volume is established via an auxiliary calculation, in which a fixed number of atoms is allowed to attain a steady-state condition with no losses present in the system. With a constant flux of atoms input into the simulation the relative trapping efficiency is calculated as a function of the molasses frequency offset, as shown in Fig. 3.13. The square points

show the number of simulated trapped atoms, while the circles show the simulated fluorescence signal from these atoms. The simulation reproduces well the frequency asymmetry seen in the experiment: as the detuning is varied narrow lineshapes are produced that exhibit the same asymmetric character. The FWHM of the simulated fluorescence curves is 4.5 MHz, in close agreement with the experimental value of  $\approx 4$  MHz. The insets of Fig. 3.13 are simulated spatial distributions of trap fluorescence for red-detuned (-1.5 MHz) and blue-detuned (+1.5 MHz) molasses beams ( $I_1 = 0.02 I_{\text{SAT}}$ ). These distributions agree closely with the observed trap fluorescence images, shown in Fig. 3.5. The blue-detuned case also reproduces the shell structures observed in the experiment where atoms are cooled and stabilized about a shell defined by the resonance condition  $\nu_{\text{AF}} = 0$ , but are cleared out of the inner region of the shell where the molasses beams are blue-detuned and cause heating.

Comparing the experimental and simulated trap sizes at a detuning of  $\nu_{\text{ofs}} = 0$  MHz, corresponding to the brightest traps, shows close agreement. The longitudinal and transverse spreads of the simulated trapped atom distribution are  $\sigma_z = 1.6$  mm and  $\sigma_t = 1.0$  mm, respectively. At this detuning the simulated fluorescence distribution has  $\sigma_z = 1.6$  mm,  $\sigma_t = 1.1$  mm, which is close to the spread of the simulated atom distribution. These numbers agree fairly well with the experimentally observed trap size ( $\sigma_z = 2.1$  mm,  $\sigma_t = 1.2$  mm).

### 3.3.2 Temperature dependence

The associated temperature dependence is calculated from the velocity distribution of the trapped atoms, and is also shown in Fig. 3.13. In this steady-state simulation, the temperature is minimized at a frequency of about  $-1$  MHz relative to the resonance condition, where it approaches the Doppler limit of  $\sim 150$   $\mu\text{K}$  along the transverse directions (triangles). The transverse directions ( $150$   $\mu\text{K}$ ) attain a



lower limit than the axial direction (diamonds,  $210 \mu\text{K}$ ). Since our simulation does not include any re-thermalization due to collisions, the temperature asymmetry is expected due to the dipole emission pattern of the cooling transition. Hence, the simulation reproduces the temperature asymmetry observed in the experiment. An average minimum temperature can be defined as  $(2T_{\text{Trans}} + T_z)/3 = 170 \mu\text{K}$ . Above the resonant frequency atoms are rapidly heated and expelled from the trap center.

### 3.3.3 Beam asymmetry

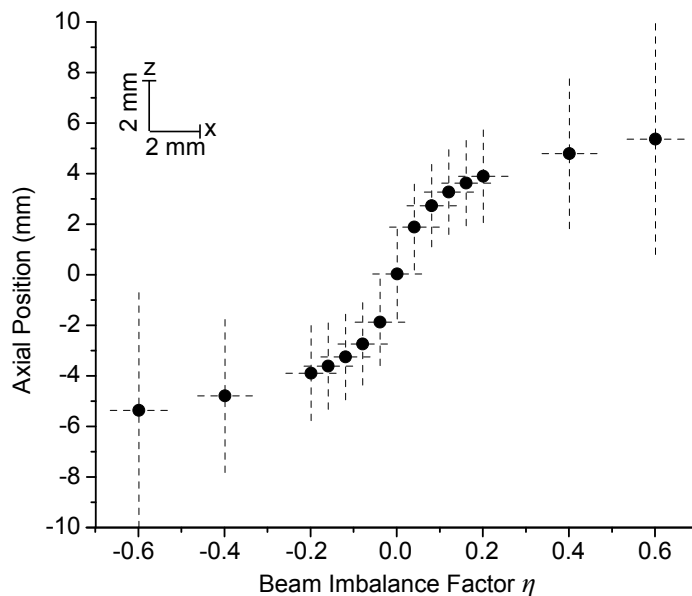


Figure 3.14: Simulated trap position along the field axis versus axial beam asymmetry parameter  $\eta = (I_{+z} - I_{-z})/(I_{+z} + I_{-z})$ , with the molasses red-detuned to one-half linewidth (3 MHz). The bars represent the simulated trap size (standard deviations) in the transverse and axial directions (scales as shown in the inset).

One particular feature distinguishing the trap's performance from that of low-field MOTs is that the trap position and atom number is highly sensitive to the relative intensities of opposing cooling beams. Figure 3.14 shows the simulated dependence of the axial position and size of the trap versus the axial beam intensity imbalance  $\eta$ :

$$\eta = (I_{+z} - I_{-z}) / (I_{+z} + I_{-z}) = (2I_{+z} - 0.04 I_{\text{SAT}}) / (0.04 I_{\text{SAT}}) \quad (3.7)$$

In Fig. 3.14 the bars represent the trap size, showing the standard deviation of the Gaussian atom distribution. The trap is displaced along the direction of the stronger molasses beam. For the case of balanced beams ( $\eta = 0$ ), the position variation of the trap over beam intensity imbalance  $\eta$ , denoted as  $\Delta z / \Delta \eta$ , is 50 mm. The result shown in Fig. 3.14 is in qualitative agreement with the observed strong sensitivity of trap position and size to beam intensity imbalances. Experimental tests have shown that a deviation of as little as 1-2 % from an even balance between the axial beam intensities both moves the trap position and greatly reduces the number of trapped atoms.

### 3.4 Summary

The high magnetic field atom trap has proven to be a stable and efficient platform for producing cold high-density samples of atoms within a large magnetic field. I have observed phenomena such as asymmetric trap fluorescence lineshapes and cold atom clouds with a shell-like distribution. The trap shows a significant spatial temperature asymmetry, with the transverse temperature being near the Doppler limit. Both  $^{85}\text{Rb}$  and  $^{87}\text{Rb}$  atoms have been cooled and trapped for a wide range of magnetic field values. The motional Lorentz electric fields associated with the residual motion of the atoms within the trap are in the range a few mV/cm. The trap is therefore suitable for precision laser spectroscopy applications, such as the excitation and observation of Rydberg atoms in strong magnetic fields.

## CHAPTER IV

# Rydberg atom spectra

### 4.1 Experimental Method

#### 4.1.1 Motivation

In this Chapter I explore the energy level spectrum of highly-excited atoms within a large bias magnetic field, and investigate the particular characteristics and properties of these states. As described in Chapter II, in the presence of a strong magnetic field the energy levels in the  $n$ -mixing regime are largely non-degenerate, with a few near-degenerate pairs of vibrator states. The goal is to investigate optical excitation to Rydberg levels, with the aim of preparing states with large dipole moments, large optical excitation cross sections, and no close degeneracies with other states.

#### 4.1.2 Trap parameters

In the experiment, cold Rydberg atoms are excited via a stepwise narrow-band photo-excitation process in a high-field ( $\sim 2.6$  T) atom trap. Several tens of millions of  $^{85}\text{Rb}$  atoms are laser-cooled to the Doppler limit ( $\sim 150$   $\mu\text{K}$ ) and magnetically confined within the Ioffe-Pritchard trap. The trapped atom cloud is cigar-shaped, of axial full width at half maximum (FWHM) = 4.0 mm and transverse FWHM = 2.2 mm. At the location of the trap, the magnetic field is stable to  $< 1$  Gauss and can be varied in discrete steps of 10 Gauss by adjusting the current

through the superconducting set of dipole coils. Rydberg atoms are produced via two-photon excitation at 780 nm and 480 nm (laser linewidths  $\leq 1$  MHz) through the intermediate  $5P_{3/2}|m_{\ell} = 5/2, m_J = 3/2\rangle$  state. Using this scheme, states with energies ranging from  $\sim -90$  cm $^{-1}$  up into the ionization continuum are excited and then subsequently detected. The lower limit of this range is due to the maximal electric field that can be applied between the two electrodes surrounding the trap ( $F_{\max} = 2.24 \times 10^4$  V/m). This experimentally-accessible range overlaps well with the range of the  $n$ -mixing regime at  $B = 2.6$  T; from  $-108$  cm $^{-1}$  to  $-35$  cm $^{-1}$ .

#### 4.1.3 Rydberg atom characteristics

Only the low-field-seeking ground state atoms with  $m_J = m_s = +1/2$  are contained within the atom trap. Since Rydberg atoms are excited with a stepwise two-photon process via the intermediate  $5P_{3/2}|m_{\ell} = 5/2, m_J = 3/2\rangle$  state, the resulting possible change in  $m_J$  are  $\Delta m_J = \{0, \pm 1\}$  and there are only three optically accessible manifolds of Rydberg levels, namely  $m_J = 1/2, 3/2$  and  $5/2$ . These three accessible manifolds are independent of each other, since states of different  $m_J$  are not coupled by parallel magnetic and electric fields. Although the time-independent states are of constant  $m_J$  and can be expressed as linear combinations of basis states with well-defined  $m_{\ell}$  and  $m_s$ , for high-lying Rydberg levels in the  $n$ -mixing regime the strong magnetic field decouples the fine structure, and almost all time-independent states have expectation values of either  $\langle \hat{s}_z/\hbar \rangle \approx 1/2$  or  $\langle \hat{s}_z/\hbar \rangle \approx -1/2$ .

Since optical excitation from the intermediate  $5P$  level does not change the expectation value of the electron spin, only the states with  $\langle \hat{s}_z/\hbar \rangle \approx 1/2$  are accessible, only about half of the time-independent states in the manifolds  $m_J = \{1/2, 3/2, 5/2\}$  are experimentally excitable, with respective expectation values  $\langle \hat{\ell}_z/\hbar \rangle \approx \{0, 1, 2\}$ . Any state with  $\langle \hat{s}_z/\hbar \rangle \approx -1/2$  is effectively dark to this excitation process.

In addition, in the case of no electric field ( $F_{\text{el}} = 0$ ) the Rydberg levels have a well-defined parity  $\Pi$ . In this case, the axial parity  $\Pi_z$  of hydrogenic wavefunctions is also a conserved quantity, as seen by considering the angular part of the wavefunction:

$$\begin{aligned}
\Pi_z Y_{\ell,m}(\theta, \phi) &= Y_{\ell,m}(\pi - \theta, \phi) \\
&= P_{\ell}^{|m|}[\cos(\pi - \theta)] \Psi_m(\phi) \\
&= (-1)^{\ell-|m|} P_{\ell}^{|m|}[\cos(\theta)] \Psi_m(\phi) \\
&= (-1)^{\ell-|m|} Y_{\ell,m}(\theta, \phi)
\end{aligned} \tag{4.1}$$

For the trapped ground state,  $\ell = 0$  and  $|m| = 0$  ( $(-1)^{0-0} = 1$ ), giving a state that is  $\Pi_z = +1$  (even). Likewise, the intermediate  $5P_{3/2}|m_I = 5/2, m_J = 3/2\rangle$  state has  $\ell = 1$  and  $|m| = 1$  and so this state also has  $\Pi_z = \text{even}$ . Rydberg excitation from this state at electric field  $F_{\text{el}} = 0$  will result in a  $\Pi_z = \text{odd}$  state for  $\Delta m = 0$  (since  $\Delta\ell = 1$ ) when the 480 nm laser polarization aligned with the magnetic field axis, and a  $\Pi_z = \text{even}$  state in the cases of  $\Delta m = \pm 1$ . These parity conservation considerations yield, in our setup,  $\Pi_z = \{\text{even}, \text{odd}, \text{even}\}$  for the optically accessible Rydberg states with  $m_J = \{1/2, 3/2, 5/2\}$ , respectively. Hence, when parity and spin-selection considerations are combined, at  $F_{\text{el}} = 0$  only about one quarter of the time-independent states within the manifolds  $m_J = \{1/2, 3/2, 5/2\}$  have substantial excitation rates, and can be experimentally observed.

## 4.2 Rydberg Excitation

The excitation pulses used to probe the Rydberg states are of variable duration; from  $\sim 1 \mu\text{s}$  for excitation rate studies on resonance to  $100 \mu\text{s}$  for extended exploratory frequency scans. A sample timing diagram is displayed in Fig. 4.1. The

excitation beams are focused into the trap with respective FWHM of the intensity profiles of  $60 \mu\text{m}$  and  $20 \mu\text{m}$ , respectively. These two beams are crossed at the trap center, resulting in a small excitation region and ensuring that the Rydberg states are produced in a well-defined, uniform magnetic field. The resulting signal is shown in Fig. 4.2. The magnetic field varies by about 2 Gauss over the entire trapping region. A state with a magnetic moment of  $10 \mu_B$  excited throughout the trap will then see a broadening of  $(10\mu_B)B = h \times 28 \text{ MHz}$  due to this magnetic field inhomogeneity. Since the magnetic dipole moments vary widely from state to state and can be quite large in magnitude (on the order of  $20 \mu_B$  at  $\sim -55 \text{ cm}^{-1}$ ), reducing the excitation volume such that the variation within the Rydberg excitation region is only in the tens of mG range is necessary in order to ensure that this broadening effect remains small (much less than 1 MHz).

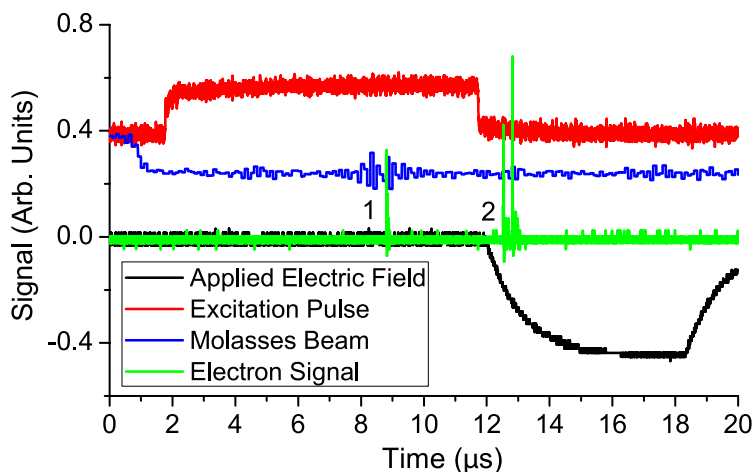


Figure 4.1: Timing schematic of the Rydberg excitation pulse. First the molasses light is turned off (blue line), followed by the two overlapped excitation pulses of variable length (red line). After a set delay, a strong electric field is rapidly applied between the electrodes (black line), up to a maximal electric field value of  $F_{\text{max}} = 2.24 \times 10^4 \text{ V/m}$ . This strong electric field ionizes the Rydberg atom population and directs the resulting free electrons toward the MCP detector. Free electrons (pulse at 1) or bound Rydberg states (2, showing two different  $m_J$  states) can then be detected.

The intensity of the lower (780 nm) excitation pulse is set to  $\sim 5 I_{\text{sat}}$  ( $I_{\text{sat}} = 1.6 \text{ mW/cm}^2$ ) as a compromise between count rate and power broadening, while the

upper (480 nm) pulse has a total power of 20 mW for an intensity maximum of  $2 \times 10^6$  mW/cm<sup>2</sup> at the focus. Excitation of the strongest lines is heavily saturated for these intensities. Observed Rydberg excitation lines have FWHM linewidths  $\sim 10$  MHz, as measured by scanning the upper (480 nm) transition laser frequency. These linewidths are limited by the power broadening of the  $5S \rightarrow 5P$  transition; there is no measurable power broadening due to the upper excitation stage. Since I use laser-cooled atoms, there is no line-broadening due to residual Doppler shifts and Lorentz electric fields ( $\mathbf{F}_{\text{el}} = \mathbf{v} \times \mathbf{B}$ ). Also, the ground-state atom sample is spin-polarized.

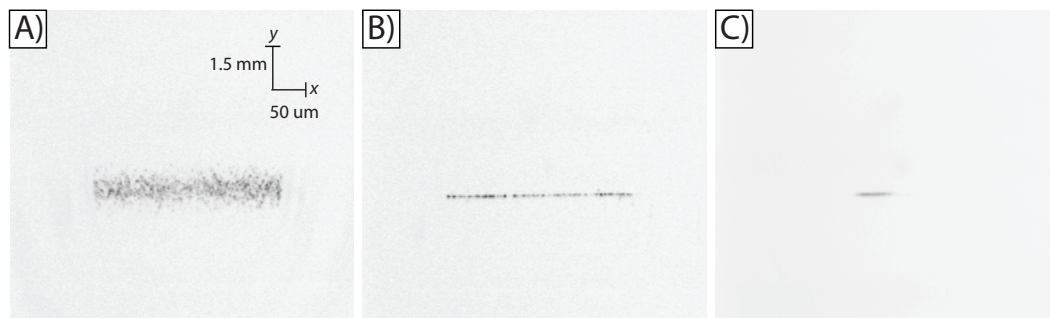


Figure 4.2: MCP phosphor screen images, showing the extent of the excitation region transverse to the magnetic field axis. The transverse scaling, shown as an inset, is the same for all three images. A) Excitation of the entire trapping region. The magnetic field lines cause magnification along one axis as the electrons exit the high-field region. B) With a large 780 nm excitation beam and a focused 480 nm beam, Rydberg atoms are created in a narrow column. C) With a crossed beam geometry with foci overlapped at the trap center, only a small volume ( $60 \mu\text{m}$  in length along the  $x$ -axis, and  $20 \mu\text{m}$  in the other directions) is excited within a constant magnetic field.

An electric field  $F_{\text{el}}$  parallel to  $B$  can also be applied throughout the excitation pulse by varying the relative potential between two electrodes surrounding the trap. The value of  $F_{\text{el}}$  can be controlled to within an accuracy of 0.2 V/m, limited by 60 Hz noise on the electrodes. Immediately following the excitation, a much stronger field ionization (FI) ramp of short duration ( $5 \mu\text{s}$ ) is applied to the electrodes. The resulting field-ionized electrons are directed toward a micro-channel plate (MCP) detector assembly located outside of the high-field region.

The lower transition 780 nm excitation pulse is frequency-stabilized to be on-resonant with the 5S-5P transition within the large magnetic field. This is accomplished by locking this laser to a home-built Fabry-Pérot interferometer, with a tunable scan range of several GHz and a long-term stability of  $\sim 8$  MHz over a 48 hour period [92]. Similarly, the upper transition 480 nm excitation pulse is locked to a second stabilized Fabry-Pérot. The frequency of this upper transition can be scanned by pressure tuning the Fabry-Pérot, with discrete steps of 0.5 MHz. More extensive frequency scans are taken by removing the frequency-stabilization circuit and directly applying a controllable bias voltage to the piezoelectric transducer. In this fashion, the laser frequency can be scanned over its entire mode-hop free range (typically 20-30 GHz) in steps of  $\sim 5$  MHz. The Fabry-Pérot transmission, with peaks separated by 500 MHz, can be monitored to provide a frequency reference.

#### 4.2.1 Penning ionization probabilities

One significant concern when preparing states with strong interactions is the possible presence of any free electrons. A free electron can mimic Rydberg-Rydberg interactions by shifting the energy levels of neighboring Rydberg atoms through the Coulomb interaction. Such electrons disturb the Rydberg atom sample and can destroy any coherence information imparted to the Rydberg atoms. Here I investigate the likelihood of such events in the high-field trap.

Free electrons can be created within the sample through Penning ionization [93]. Here, a collision between two Rydberg atoms results in a more deeply bound atom, as well as a more energetic electron that is no longer bound to its parent ion. Alternatively, free electrons can also be produced via thermal ionization, where background radiation ionizes the Rydberg atom. Such ionization is most probable at an energy of wavenumber  $\bar{\nu} = k_B T / (hc)$ , corresponding to the thermal background tempera-



ture. In the case of the high-field trap, optical access ports cause the background temperature to be higher than the 4 K walls of the Helium cryostat, but thermal ionization events will still be peaked at very high energies ( $\bar{\nu} \sim 10 \text{ cm}^{-1}$ ).

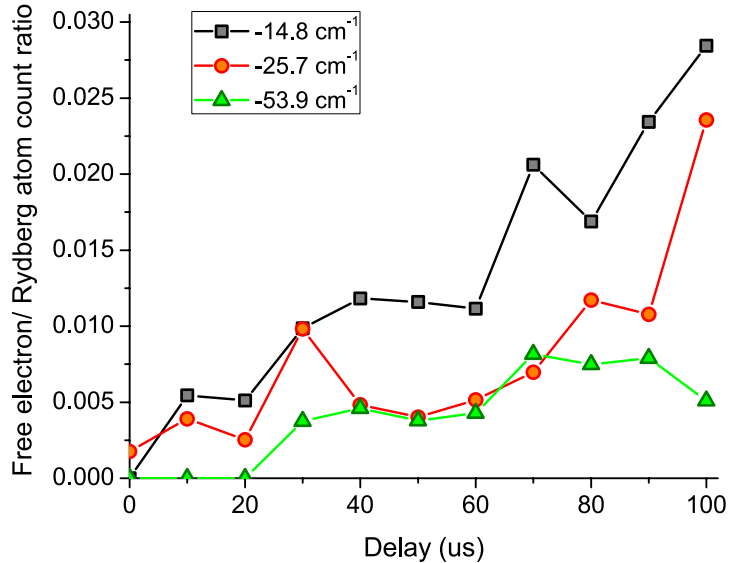


Figure 4.3: Fraction of counts from a  $10 \mu\text{s}$  Rydberg excitation pulse arriving as free electrons versus delay time, for various energy levels.

In order to determine whether the possible presence of free electrons are a concern in the high-magnetic-field Rydberg atom system I examined the likelihood of electron production events. By applying a small electric field throughout the excitation pulse as well as during a delay time immediately following the pulse, any free electrons will be directed toward the MCP, and be subsequently detected. After this variable delay, I then apply a strong electric field pulse to ionize the remaining Rydberg sample. Figure 4.3 shows the resulting signal fraction due to the electron signal as a function of delay time after the  $10 \mu\text{s}$  excitation pulse. Typical Rydberg detection rates are of 10 counts/shot, so a ratio of 0.01 would represent approximately one free electron event every tenth experimental repetition. At higher energy levels, both the absolute

number of detected electrons and the ratio increases with delay time, signifying that ionization is a concern. However, below  $-50 \text{ cm}^{-1}$  the free electron signal fraction is small and roughly constant. In this regime strongly-interacting Rydberg states can be created and held for long periods ( $\sim 100 \mu\text{s}$ ) without appreciable losses due to ionization events. I will therefore focus my investigation of strong Rydberg interactions on states around or below  $-50 \text{ cm}^{-1}$ , as detailed further in Sec. 4.5.

### 4.3 Overview of Rydberg Spectra and State Density

Figures 4.4 and 4.5 show some Rydberg excitation spectra throughout the  $n$ -mixing and chaotic regimes, taken with long excitation pulses of  $100 \mu\text{s}$ . Here the polarization of the upper transition 480 nm laser is set to excite  $m_J = 3/2$  states. However, because of the angle of incidence into the trap (a result of the optical access of the trapping apparatus) and the long pulse excitation times,  $m_J = 1/2$  and  $m_J = 5/2$  states are, to a lesser extent, also excited. As expected, the density of states increases dramatically with excitation energy. At the highest excitation energies, the density of detected states approaches the inverse excitation bandwidth, so that individual states can no longer be resolved. For this high energy range within the chaotic regime, periodic modulations of the density of states [94] related to the underlying classical physics of the system begin to emerge.

For the spectra to be suitable for studies involving coherent Rydberg-atom interactions, the average density of states should be lower than the inverse of anticipated Rydberg-atom interaction energies, so that off-resonant levels can be ignored. Since anticipated Rydberg-atom interaction energies are on the order of tens of MHz (see Sec. 5.7), densities of states well below  $\sim 100/\text{GHz}$  are desired. This is achievable in the high-magnetic-field system since states of different  $m_J$  are decoupled. The den-

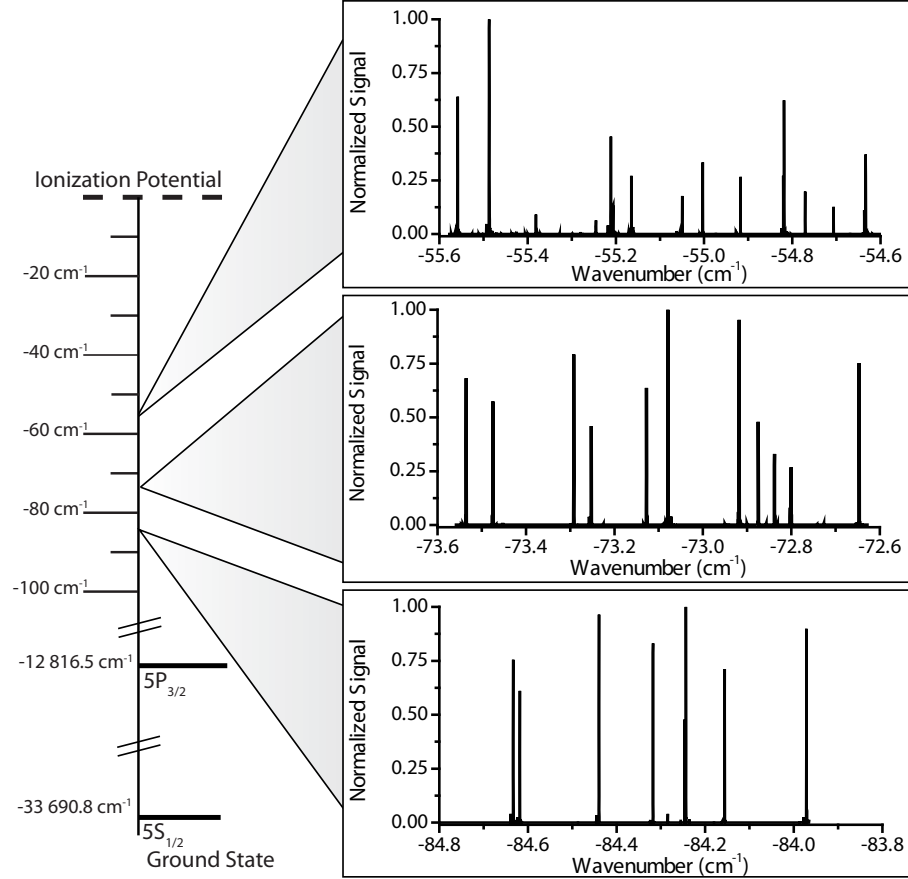


Figure 4.4: Sample Rydberg excitation spectra, with  $F_{el} = 0$ , for lower energy ranges. Rydberg atoms within the  $m_J$  manifolds with  $\{1/2, 3/2, 5/2\}$  are excited. Only one axial parity  $\Pi_z$  is excited for each  $m_J$ , and only states with  $\langle \hat{s}_z / \hbar \rangle \approx 1/2$  are optically accessible.

sity of states can be determined at various energies by investigating the experimental data for various energy ranges. At  $F_{el} = 0$ , only one parity for each  $m_J$  state can be excited, and all states have  $\langle \hat{s}_z / \hbar \rangle \approx 1/2$ . This means that in the absence of an electric field only a quarter of the energy levels can be experimentally observed.

From Figures 4.4 and 4.5 and similar data, for  $F_{el} = 0$  we determine average densities of states of 0.5/GHz and 1.9/GHz at energies about  $-55 \text{ cm}^{-1}$  and  $-19 \text{ cm}^{-1}$ , respectively. Figure 4.6 shows the observed density of states for a wide range of energy levels, ranging from  $\sim -85 \text{ cm}^{-1}$  to  $\sim -5 \text{ cm}^{-1}$ . The average density of states increases with excitation energy, but it is always well below 100/GHz over this entire

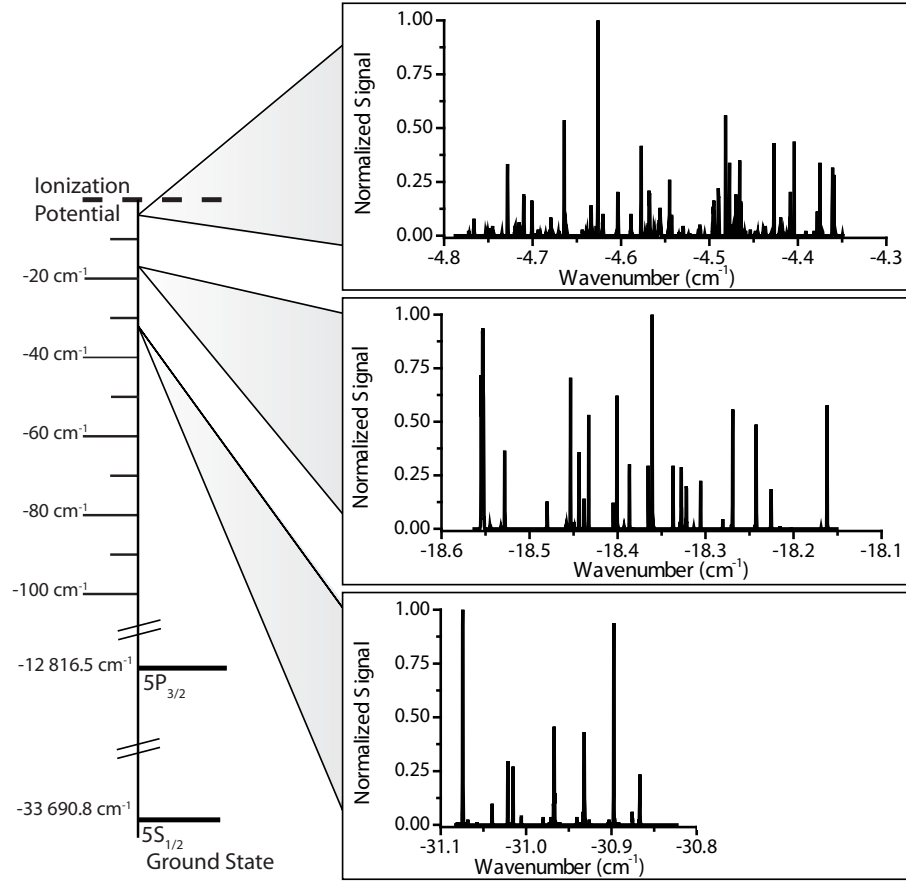


Figure 4.5: Sample Rydberg excitation spectra, with  $F_{\text{el}} = 0$ , for three higher energy ranges. As the energy is increased the Rydberg state density grows, until resolution of individual states is lost. At these higher energies a more regular structure begins to take shape.

energy range. Therefore, it should be possible to find quantum states that are far away from other levels and that are conducive to strong atom-atom interactions (by having large electric dipole moments, for instance, as discussed further in Chap. V).

The experimentally observed densities of states compare well with a semi-classical calculation. The energy-averaged average number of levels below energy  $E$  is  $\bar{N}(E) = \Omega(E)/(2\pi\hbar)^f$ , where  $\Omega(E)$  is the total volume of phase space for a given  $E$  and  $f$  is the number of degrees of freedom. From this, the average density of eigenstates per unit energy can be calculated using the Weyl theorem (as detailed in Eq. 16.4 in Ref. [94]):

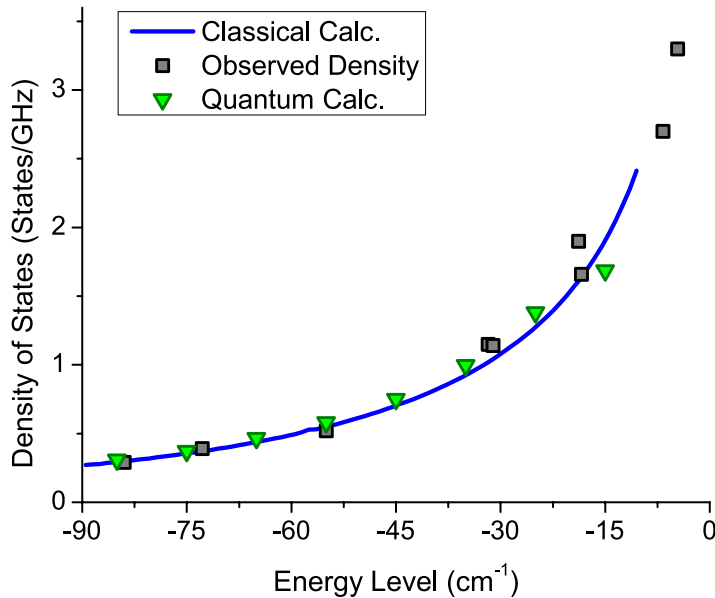


Figure 4.6: Comparison between observed and calculated density of states (in number of states per GHz) versus excitation energy. For the classical and quantum mechanical calculations, the number of observable states are shown (taking into account parity and spin conservation considerations). The quantum mechanical calculation is valid up to  $n \sim 90$ , or equivalently  $-15 \text{ cm}^{-1}$ .

$$\bar{\rho}(E) = \left(\frac{1}{2\pi\hbar}\right)^f \int d^f p d^f q \delta(E - H(\mathbf{p}, \mathbf{q})) \quad (4.2)$$

Here the integral occurs over the available phase-space, as determined by the Rydberg atom Hamiltonian. Counting only states of one  $\Pi_z$ -parity, the semiclassical calculation yields state densities of 0.57/GHz and 1.6/GHz for  $-55 \text{ cm}^{-1}$  and  $-20 \text{ cm}^{-1}$ , respectively. These results are sums over the three optically accessible manifolds, and compare well to the measured values as shown in Fig. 4.6. Here, the blue line shows the result of this Weyl calculation.

It is important to note that this calculation only gives an average density of states; the local density of states varies about the given average values in a manner that can only be revealed by measurements or calculations of the actual quantum spectrum described by the full Hamiltonian (Eq. 2.2). The level statistics and the level distribution also depend on how deep the system is into the “quantum-chaotic” regime,

where level repulsion occurs. For detailed discussions of this topic, see Refs. [44, 94] and references therein.

The measured results can also be compared to a full quantum mechanical treatment of the Rydberg atom Hamiltonian. This calculation, described fully in Sec. 5.1, involves a diagonalization of all states within the same  $m_J$  manifold from  $n = 10$  to 90. The results are fairly accurate within the initially-considered energy range (without the magnetic field being applied); from  $-1000 \text{ cm}^{-1}$  to  $-15 \text{ cm}^{-1}$ . Since the semi-classical calculation only determines the average density of states, to compare the two it is necessary to average the calculation over a large energy range, given by the characteristic cyclotron frequency ( $\bar{\nu} = 2.4 \text{ cm}^{-1}$ ). The quantum mechanical states are therefore summed into bins of  $10 \text{ cm}^{-1}$  to arrive at the average density of states (considering parity and spin considerations). The green triangles in Fig. 4.6 show close agreement to both the experimental observations and the Weyl state density calculation.

#### 4.4 Above-threshold excitation

The high-magnetic-field energy level structure also differs from the field-free case in the fact that the ionization threshold is dependent on the quantum numbers  $m_s$  and  $m_\ell$ . As described in Sec. 2.4, with a strong applied magnetic field the ionization threshold is:

$$\text{IP} = \left[ \frac{1}{2}(m_\ell + |m_\ell|) + m_s - \frac{1}{2} \right] \hbar\omega_c \quad (4.3)$$

Figure 4.7 shows two long frequency scans above the ionization threshold. Since the angle of the blue (480 nm) excitation beam always causes some direct excitation to  $m_\ell = 0, m_s = 1/2$  states, there will be some baseline ionization rate due to the

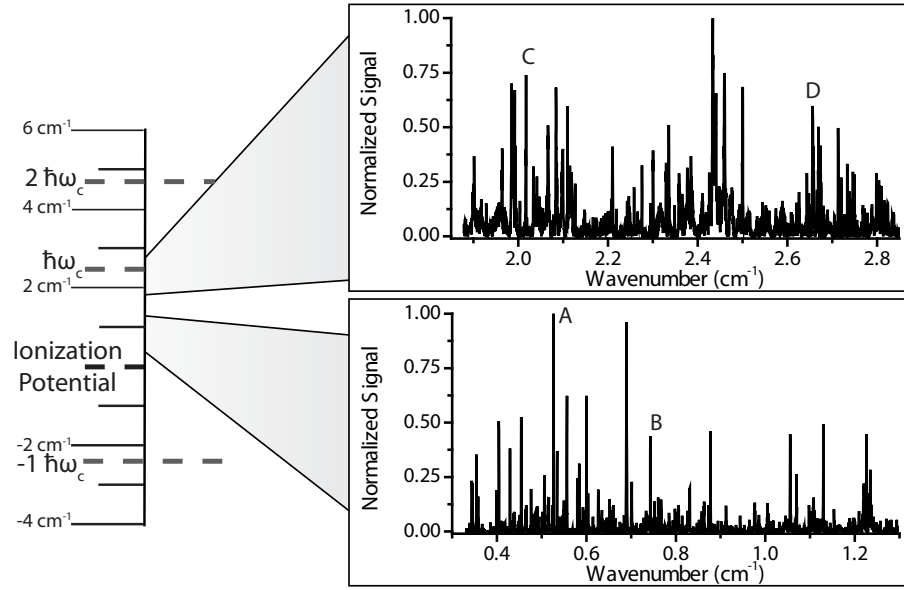


Figure 4.7: Sample Rydberg excitation spectra, with  $F_{\text{el}} = 0$ , above the field-free ionization threshold. The ionization thresholds steps (in  $\hbar\omega_c$ ) for the case of 2.6 T illustrated here are indicated on the left.

excitation of above-threshold states. Here there is a superposition of long-lived bound manifolds with  $m_\ell > 0$ , rapidly auto-ionization states, and direct ionization to the continuum. In Figure 4.8 I present time-resolved traces for a few selected strong energy resonances showing the different possible behaviors; these correspond to the states labeled A-D in Fig. 4.7. After a short  $5 \mu\text{s}$  excitation pulse, the Rydberg states are left to evolve for  $\sim 10 \mu\text{s}$ . During this time, any free electrons produced are directed toward the MCP by a very small applied electric field. After the delay period, a field ionization pulse is applied to the electrodes so as to ionize the remaining sample. Fig. 4.8 shows several different types of behavior: some strong resonances immediately auto-ionize, while the excited electrons of other states remain bound to the positive ionic core for quite some time.

Auto-ionization of Rydberg states above the field-free ionization threshold can occur through two different mechanisms. First, the spin-orbit interaction operator will couple states of  $[m_\ell, m_s = 1/2] \rightarrow [m_\ell + 1, m_s = -1/2]$ :

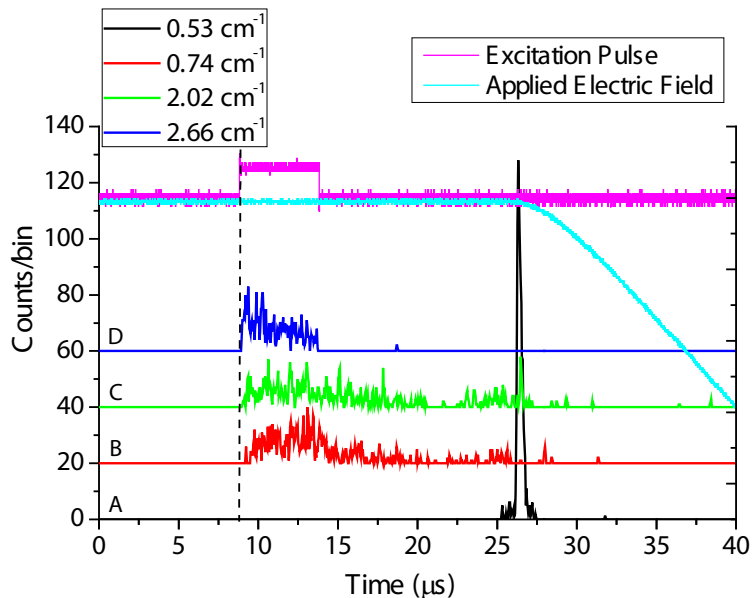


Figure 4.8: Time-resolved signal from several Rydberg resonances above the field-free ionization threshold, with a small electric field applied to collect any free electron signal. Traces labels correspond to the indicated energy levels in Fig. 4.7.

$$\hat{\mathbf{L}} \cdot \hat{\mathbf{S}} = \frac{1}{2}[\hat{L}_+ \hat{S}_- + \hat{L}_- \hat{S}_+] + \hat{L}_z \hat{S}_z \quad (4.4)$$

This will cause transfer into states with  $m_s = -1/2$ , but cannot cause auto-ionization on its own unless  $m_\ell < 0$ . Since only the  $m_\ell \approx \{0, 1, 2\}$  Rydberg manifolds are originally excited, this does not contribute directly to the observed auto-ionization.

A second process causing auto-ionization is  $m_\ell$ -mixing [95], which couples states with  $m_\ell \rightarrow m_\ell - 1$ . This is an energy-conserving coupling produced by the presence of small stray electric fields and residual motional electric fields. This results in resonant transfer from the bound excited state to an unbound level, giving a Feshbach-type decay [44]. As shown in Fig. 4.8, this coupling and the resulting auto-ionization can differ widely from state to state [96].

High-resolution frequency scans above the field-free ionization threshold show



somewhat of an ordered structure on a finer scale than the Landau resonances of  $\hbar\omega_c$ . This has previously been observed in lithium atoms [97], where it was suggested that the cause may be a separation of the electron motion into a fast transverse and a slow axial component.

#### 4.5 Level Structure at fixed magnetic and varied electric fields

Returning to the central topic of Rydberg-Rydberg interactions, I need to investigate the possibility of exciting strongly-interacting Rydberg states within a lower energy range ( $\sim -50 \text{ cm}^{-1}$ ), where Rydberg ionization is not a concern. To look for strong interactions, I compare Rydberg spectra taken with and without an applied DC electric field, and observe the corresponding energy shifts.

To measure the effect of an applied parallel electric field  $F_{\text{el}}$ , I consider spectra taken at fixed magnetic field  $B$  of approximately 2.58 T for conditions of  $F_{\text{el}}$  ranging from zero to 50 V/m. Figure 4.9A shows the Rydberg states observed as a function of frequency as the upper transition (480 nm) laser is scanned over several GHz at  $\sim -55 \text{ cm}^{-1}$  (corresponding to a scaled energy  $\epsilon \approx -0.51$ ), with excitation pulses of 100  $\mu\text{s}$  duration. Each vertical trace corresponds to a fixed electric field  $F_{\text{el}}$  being applied during the excitation pulse, as the 480 nm laser frequency is slowly varied in discrete steps after a series of experimental data collection cycles. This is then repeated for several values of  $F_{\text{el}}$  to determine the effect of the applied electric field. The polarization of the 480 nm laser is set mostly parallel to the  $B$ -field axis to excite  $m_J = 3/2$  states. Again, due to the beam's angle of incidence a small amount of the orthogonal polarization is also present so that  $m_J = 1/2$  and  $5/2$  states are also excited. Since this scan is recorded within the  $n$ -mixing regime, the observed Rydberg states are somewhat spread out in frequency and are, with a few exceptions,

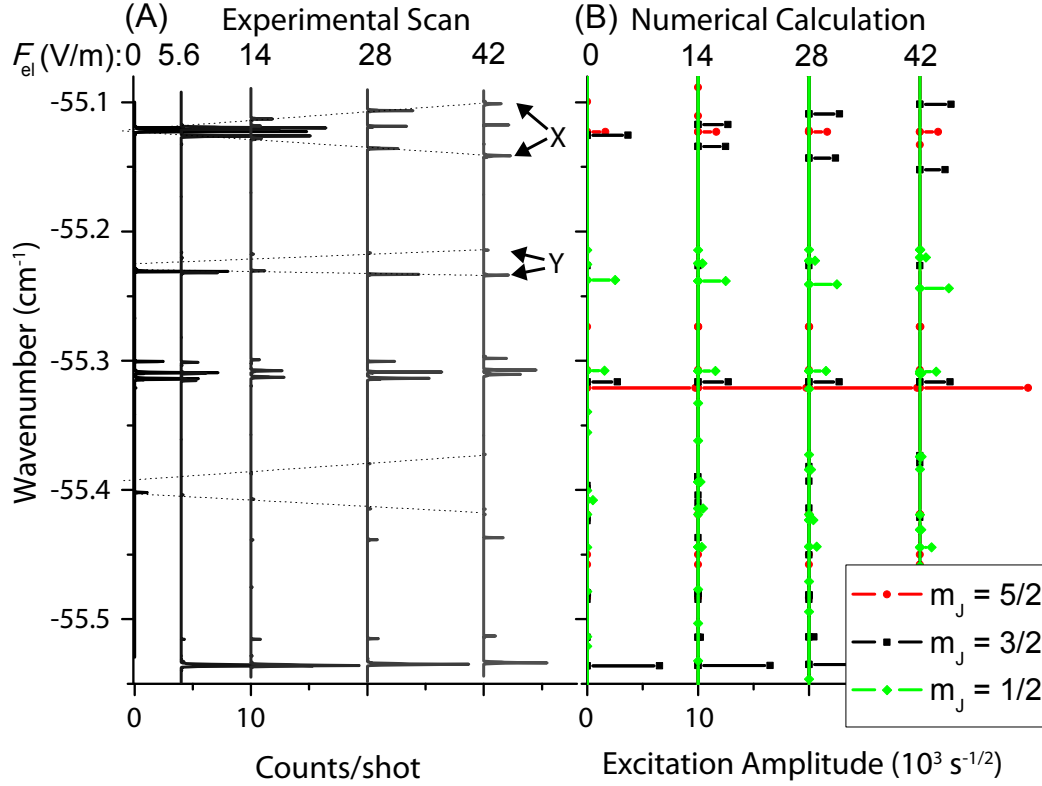


Figure 4.9: A) Rydberg levels observed in the vicinity of scaled energy  $\varepsilon \approx -0.51$ , probed by scanning the upper transition laser frequency, for  $B_{\text{exp}} = 2.577$  T, and at the indicated electric-field values. Level energies are shown with respect to the field-free photo-ionization threshold. Some close-lying level pairs of the same  $m_J$  exhibit large and opposite electric dipole moments (slopes of the dotted lines). B) Calculated line spectra, as detailed in Section 5.1, for  $B_{\text{th}} = 2.581$  T. In the calculations, states of both parities are shown for all optically accessible  $m_J$ -levels, and states with  $m_s = -1/2$  are also included. Hence, numerous calculated levels are experimentally undetectable.

non-degenerate.

While the above average densities of states are fairly low, near-degeneracies of states of the same  $m_J$  do occur. For the purpose of creating states with large electric dipole moments, the most interesting candidates occur when there are degeneracies between states of same  $m_J$  and opposite parity, which I refer to here as  $|1\rangle$  and  $|2\rangle$ . In that case, a weak parallel electric field  $F_{\text{el}}$  can be used to generate states with a permanent electric dipole moment,  $p_0 = -e\langle 1|z|2\rangle$ , and large linear Stark shifts. The detailed behavior depends on the overlap between  $|1\rangle$  and  $|2\rangle$ , and on the energy splitting at  $F_{\text{el}} = 0$ . In Fig. 4.9A I explore the effect of the applied parallel electric

field. Some energy levels shift strongly as a function of  $F_{\text{el}}$ , while others are largely unaffected. For instance, the level pair labeled “X” in Fig. 4.9 exhibits such a strong linear Stark shift. The “X” level pair represents a near-degenerate pair of vibrator states of opposite parity, as discussed in Sec. 2.5.

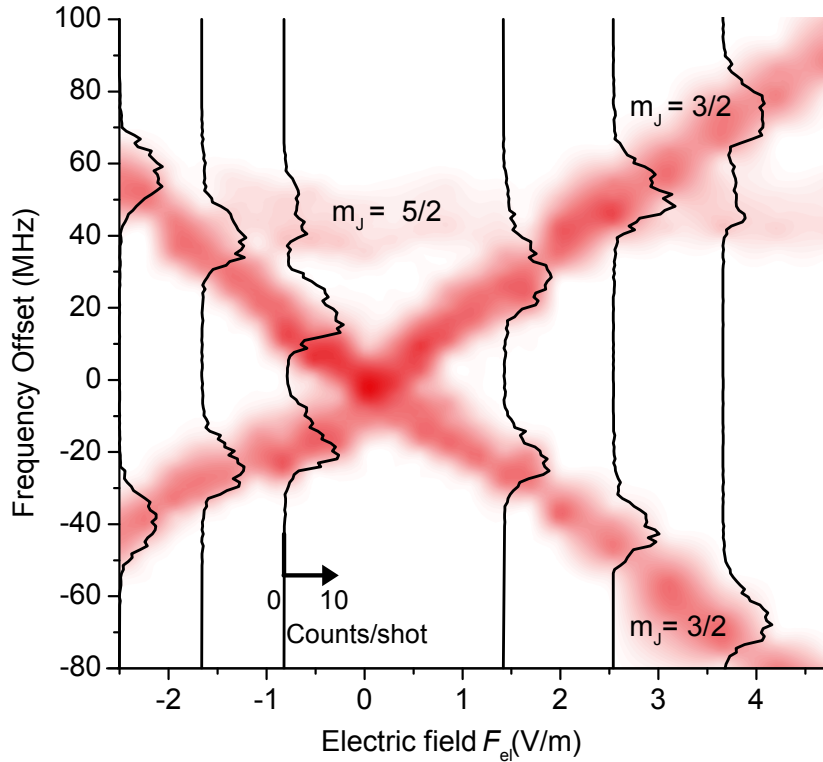


Figure 4.10: High-resolution contour plot showing the pair of Rydberg states labeled “X” in Fig. 4.9 at  $-55.1 \text{ cm}^{-1}$ , with  $B_{\text{exp}} = 2.576 \text{ T}$  and excitation pulse lengths of  $10 \mu\text{s}$ . Excitation frequency versus applied electric field (V/m) is plotted, with color representing the observed excitation rate (white = 0, red = 14 counts per shot). The electric field is varied in steps of  $0.3 \text{ V/m}$ , and a few selected scans are overlaid as black lines. The weak state at a fixed frequency offset of about  $40 \text{ MHz}$  has  $m_J = 5/2$ , and is excited due to imperfect polarization. The  $m_J = 5/2$  state has a negligible Stark shift and does not couple to the  $m_J = 3/2$  pair of states.

To reveal more detail near  $F_{\text{el}} = 0$ , in Fig. 4.10 I show a set of higher-resolution scans of the same pair over a much smaller range of  $F_{\text{el}}$ . From Fig. 4.10 the permanent dipole moment of the “X” pair of levels, given by the negative slope, is found to be  $\pm 1500 ea_0$ . A good comparison for the strength of these electric dipole moments would be to the absolute dipole moments of Stark states of Rydberg atoms in no

magnetic and weak electric fields [3]. To first order, this is:

$$W_{n,n_1,n_2} = \frac{-1}{2n^2} + \frac{3}{2}F_{\text{el}}(n_1 - n_2)n \quad (4.5)$$

Here  $n_1$  and  $n_2$  are the parabolic quantum numbers ( $n_1 + n_2 + |m| + 1 = n$ ). The extreme Stark states are given by maximal separation of  $n_1 - n_2 = n - 1$ :

$$p_{\text{max}} = \frac{3}{2}(n_1 - n_2)n = \frac{3}{2}n(n - 1) \approx \frac{3}{2}n^2 = -\frac{3}{4E} \quad (4.6)$$

In this case, for an effective quantum number of  $n = 45$  (corresponding to an energy of  $-55 \text{ cm}^{-1}$ ) the largest possible dipole moment is  $\sim 2900 ea_0$ . The magnitude of the electric dipole moments of the “X” pair is therefore quite large; it is about half the dipole moment of extreme Stark states of comparable energy. Such field-free extreme Stark states are difficult to isolate and use experimentally, as they lie at the edges of a fan of many states split only by the electric field. The presence of nearby states in the fan make such levels unsuitable for Rydberg atom interaction applications. As well, an additional perturbation, such as the presence of a magnetic field, will cause state-mixing. In contrast, in the high-magnetic-field trap within the  $n$ -mixing regime very few degeneracies remain, and we observe isolated pairs of states that could be used for quantum control experiments.

The “X” pair of levels has a local degeneracy at a local electric field of  $F_{\text{el}} = 0 \text{ V/m}$ , as shown in Fig. 4.10. Within the experimental apparatus, the degeneracy is observed at an applied voltage of 16 mV, corresponding to an offset field of  $F_{\text{el}} = 0.9 \text{ V/m}$ . The small offset is likely due to static patch or contact potentials, or caused by the analog control electronics. This observed offset is constant from day to day, and can therefore be compensated by applying a small bias field.

The “X”-pair of states in Figs. 4.9 and 4.10 are 50/50 mixtures of a  $\Pi_z$ -even and

a  $\Pi_z$ -odd state at all non-zero values of  $F_{\text{el}}$ . Since in the experiment only a single definite axial parity (odd parity for  $m_J = 3/2$ ) is excited, both components of the pair should exhibit equal line strength, regardless of  $F_{\text{el}}$ . Figures 4.9 and 4.10 show that for the “X”-pair of states this is indeed the case. It is noted that an exact crossing, as shown in Fig. 4.10, requires a well-tuned magnetic field. The resonant magnetic-field value is different for each individual set of near-degenerate states (see Sec. 4.6). The case of coupled vibrator states that are near-degenerate at  $F_{\text{el}} = 0$  is analogous to the one-dimensional double-well model detailed in Chapter II.

In the  $n$ -mixing regime, most electric-field-coupled pairs of vibrator states encountered are non-degenerate at  $F_{\text{el}} = 0$ , with an energy splitting on the order of  $\Delta E \sim 100$  MHz. An instance of that case is found in the “Y”-pair of lines in Fig. 4.9A. In that case, the time-independent states maintain opposite parities  $\Pi_z$  at small values of  $F_{\text{el}}$ . It takes a substantial field  $F_{\text{el}}$  for the Stark shifts to become comparable to the energy splitting  $\Delta E$  and for substantial state mixing to occur. Since in our experiment only one parity is optically excited, one observes highly asymmetric line strengths up to values of  $F_{\text{el}}$  at which the Stark shifts become larger the energy splitting  $\Delta E$ . If  $F_{\text{el}}$  is increased further, the line-strength ratio of such state pairs trends toward unity, as the time-independent states converge towards even and odd superpositions of the two  $F_{\text{el}} = 0$  states. Those characteristics are found in the “Y” pair of lines in Fig. 4.9A.

Figure 4.11A shows another data set for several applied electric field values, taken at a higher energy level of  $\sim -31$  cm<sup>-1</sup>. Here the states lie within the chaotic regime. The observed energy level structure under an applied electric field is more complex as a result of the higher density of states and stronger level repulsions that characterize this regime. Although there are several energy levels that show large electric dipole

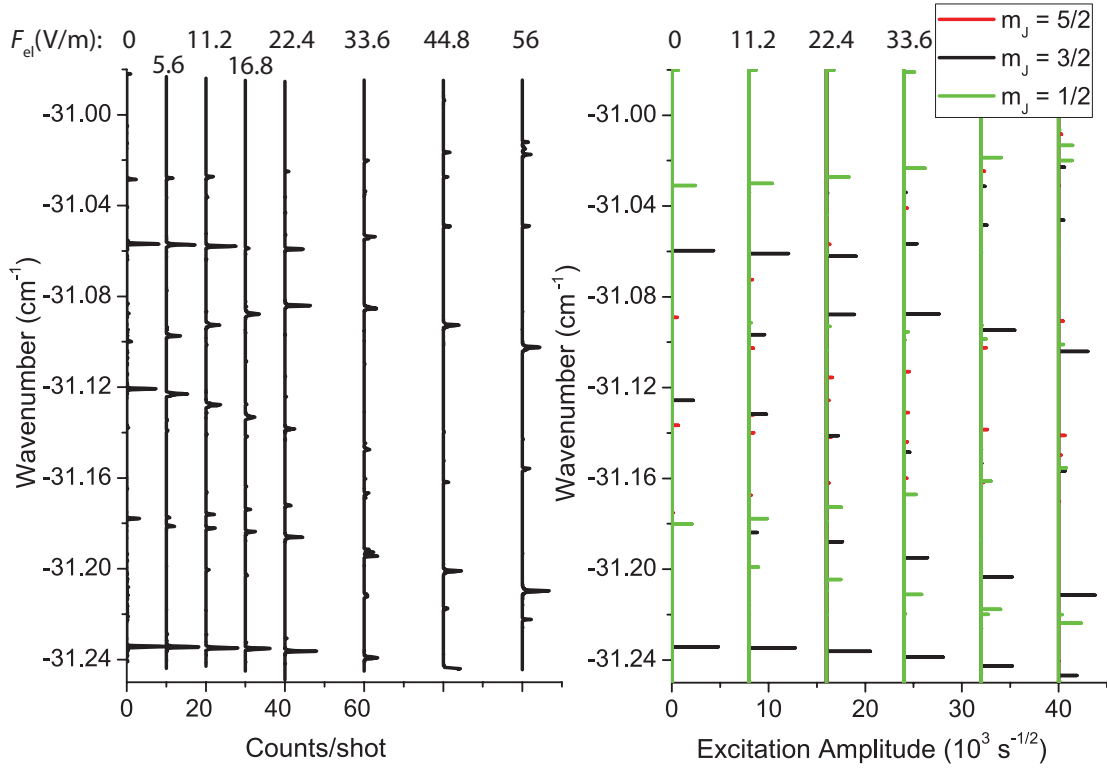


Figure 4.11: A) Rydberg levels observed in the vicinity of  $\sim -31 \text{ cm}^{-1}$  (corresponding to a scaled energy  $\varepsilon \approx -0.29$ ), probed by scanning the upper transition laser frequency, for  $B_{\text{exp}} = 2.577 \text{ T}$ , and at the indicated electric-field values. Level energies are shown with respect to the field-free photo-ionization threshold. B) Calculated line spectra, as detailed in Section 5.1, for  $B_{\text{th}} = 2.581 \text{ T}$ .

moments, the higher density of states makes it difficult to find isolated interacting pairs of states. Already at electric field values of  $\sim 10 \text{ V/m}$ , several energy levels of the same  $m_J$  are observed to be interacting, making the energy structure with respect to  $F_{\text{el}}$  much more complicated. This in turn renders such states less suitable for Rydberg-atom interaction experiments in which the internal-state structure remains confined to only a few states.

#### 4.6 Magnetic-field tuning of near-degenerate states

The magnetic-field-dependence of the Rydberg levels can be used to tune near-degenerate opposite-parity vibrators states into resonance, i.e. to tune their energy

splitting  $\Delta E$ . This enables the production of highly polar states by application of a weak parallel electric field  $F_{\text{el}}$ . As an example, in this Section I show that the “X”-pair of levels in Figs. 4.9 and 4.10 can be tuned through resonance at  $F_{\text{el}} = 0$  by exploiting the difference in their magnetic moments.

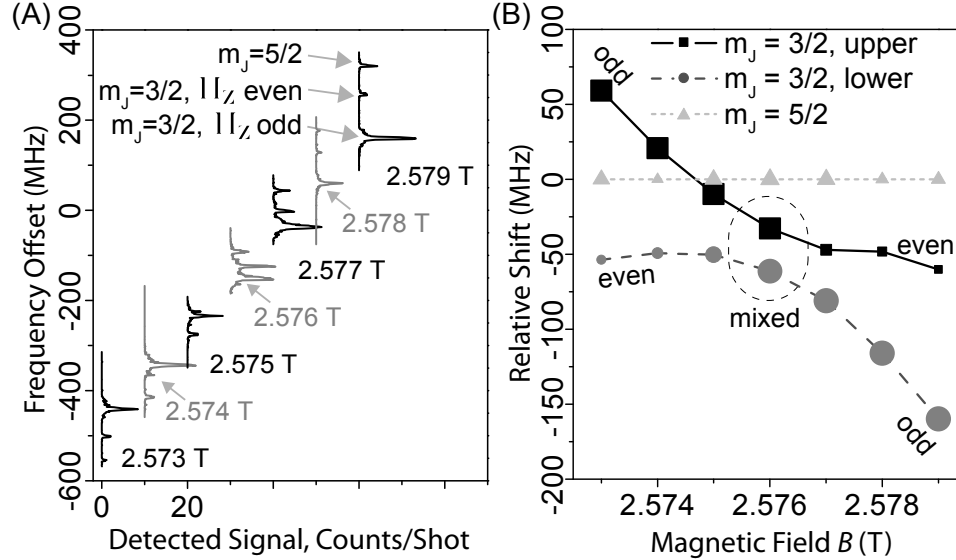


Figure 4.12: A) Scans of the state pair labeled “X” in Fig. 4.9 for the indicated magnetic field values and a weak parallel electric field  $F_{\text{el}} \approx 1$  V/m. The presented line shifts here are relative to that of the  $5P_{3/2}|m_l = 5/2, m_J = 3/2\rangle$  level. B) Levels of the “X”-pair of states, which both have  $m_J = 3/2$ , relative to the  $m_J = 5/2$  level, which is used as a convenient reference line. Symbol size qualitatively represents line strength. The “X”-pair of states exhibits an anti-crossing (instead of an exact crossing) because of the coupling induced by the weak electric field  $F_{\text{el}}$ .

Since the diamagnetic shift depends on the transverse spread of the wavefunction, which varies from state to state, usually one can use the magnetic field to fine-tune the energy splitting  $\Delta E$  of any arbitrary level pair. Lines observed near  $-55$   $\text{cm}^{-1}$  and  $B \approx 2.6$  T bear a range of instantaneous magnetic dipole moments varying from 0 to about  $-20 \mu_B$ . The magnetic dipole moments are measured by incrementing the magnetic field by a small amount  $\Delta B = 10$  G, corresponding to a 0.04 % change of the 2.6 T field, and then measuring the corresponding energy shifts of the Rydberg states of interest. Fig. 4.12A shows the response of the same level pair marked “X” in Fig. 4.9 to a change of the bias magnetic field. A slight electric field,  $F_{\text{el}} \approx 1$  V/m, is

applied to resolve the two states in the crossing region. It is noted that in Fig. 4.12A all three observed energy levels exhibit a large common shift as a function of magnetic field, indicating that all three states have similar magnetic dipole moments.

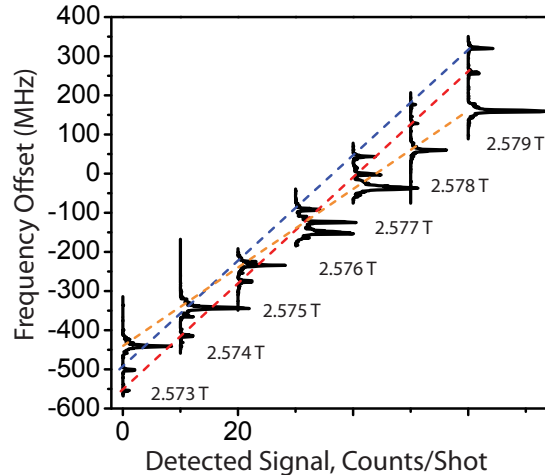


Figure 4.13: Magnetic field scan from Fig. 4.12, with colored lines (red and orange for the  $m_J = 3/2$  line pair, blue for the  $m_J = 5/2$  line) drawn to guide the eye. The lines match up well to the scans, making it fairly easy to identify the corresponding states for the various magnetic fields. Fits give magnetic dipole moments of  $-9.2 \mu_B$  and  $-11.7 \mu_B$  for the odd and even parity  $m_J = 3/2$  levels, respectively. The non-interacting  $m_J = 5/2$  state has a magnetic dipole moment of  $-11.7 \mu_B$  as well.

In identifying which Rydberg levels correspond to each other in the displayed scans, it helps to note that the three levels fall on three approximately straight lines, indicating that the individual magnetic dipole moments of the three levels are fairly constant throughout the displayed magnetic field range; fits give magnetic dipole moments of  $-9.2 \mu_B$  for the odd  $m_J = 3/2$  state, and  $-11.7 \mu_B$  for the even  $m_J = 3/2$  state. The non-interacting  $m_J = 5/2$  state present has a fitted magnetic dipole moment of  $-11.7 \mu_B$ . The difference in dipole moments is clearly seen in Fig 4.12B, with the measured frequency shifts of the two  $m_J = 3/2$  levels presented relative to the convenient  $m_J = 5/2$  reference line (which does not couple to  $m_J = 3/2$  levels). The observed line strengths of the states are visualized by the size of the plotted symbols. Away from the crossing region the applied electric field



is insufficient to couple the states. There, only the odd state is observed while the even one is (almost) undetectable, and both states have zero electric dipole moment. At resonance ( $B = 2.576$  T), the weak electric field couples the even- and odd-parity levels into highly polar states that have equal optical excitation cross sections.

#### 4.6.1 Comparison of coupling behavior with a two-level system

The width of the anti-crossing, measured to be 28 MHz in Fig. 4.12B, is in good qualitative agreement with a simple two-state Hamiltonian:

$$\begin{aligned} \hat{H}_{\text{two-level}} &= -\mu_1(B - B_0)|1\rangle\langle 1| - \mu_2(B - B_0)|2\rangle\langle 2| \\ &+ F_{\text{el}}p_0(|1\rangle\langle 2| + |2\rangle\langle 1|) \end{aligned} \quad (4.7)$$

Here,  $\mu_1$  and  $\mu_2$  are the magnetic dipole moments of states  $|1\rangle$  and  $|2\rangle$ , respectively.  $B_0$  is the magnetic field at which the levels are in resonance ( $\Delta E_{12} = 0$ ), and  $p_0$  is the electric dipole moment of the system ( $p_0 = -e\langle 1|z|2\rangle$ ). We can write the system in matrix form:

$$H = \begin{bmatrix} -(B - B_0)\mu_1 & p_0F_{\text{el}} \\ p_0F_{\text{el}} & -(B - B_0)\mu_2 \end{bmatrix} \quad (4.8)$$

For the case of  $B = B_0$  (resonance between the states), the eigenvectors of the system are then:

$$|\psi\rangle = \frac{1}{\sqrt{2}}(|1\rangle \pm |2\rangle) \quad (4.9)$$

Under applied electric and magnetic fields, the level splitting is:

$$\Delta E_{12} = 2\sqrt{(F_{\text{el}}p_0)^2 + \frac{1}{4}((\mu_1 - \mu_2)\Delta B)^2} \quad (4.10)$$

As sketched in Fig. 4.14, for the magnetic dipole moments given in Fig. 4.13, an electric dipole moment of  $p_0 = 1500 ea_0$  (as determined from Fig. 4.10), and with  $F_{\text{el}} = 1 \text{ V/m}$  the level separation at the resonant magnetic field ( $B = B_0$ ) is  $2F_{\text{el}}p_0 = h \times 38 \text{ MHz}$ . This is in good qualitative agreement with the measured separation of 28 MHz for  $F_{\text{el}} = 1 \text{ V/m}$ . The discrepancy is due to the experimental level resolution (10 MHz), the electric-field uncertainty (0.2 V/m, *i.e.* 20 % of the field applied in Fig. 4.12), and the uncertainty of the measured electric dipole moment ( $\sim 100 ea_0$ ). It is possible to reduce the applied electric field  $F_{\text{el}}$  such that the two  $m_J = 3/2$  states in Fig. 4.12 exactly cross to within the experimental level resolution of 10 MHz.

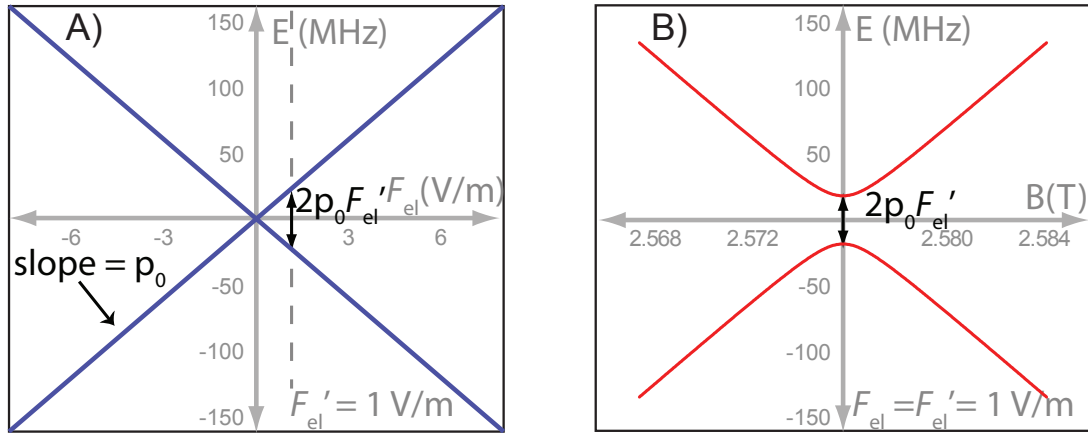


Figure 4.14: A) Energy levels of the simplified two-level Hamiltonian versus electric field, for  $B = B_0$ . B) Energy levels versus magnetic field, under an applied electric field  $F_{\text{el}} = 1 \text{ V/m}$ . Here for a universal slope of  $1.46 \times 10^{11} \text{ Hz/T}$  (or  $-10.45 \mu_B$ ) has been subtracted from both levels to more clearly show the anti-crossing behavior. The level splitting is  $\Delta E = 2F_{\text{el}}p_0$ .

It is also instructive to compare this two-level model Hamiltonian to the full quantum mechanical calculation (as detailed in Chap. V). This calculated splitting, shown in Fig. 4.15, matches the model splitting of 36 MHz exactly at a magnetic field value of  $B = 2.581 \text{ T}$ . This is indicative that this is truly an isolated two-level interaction; all other  $m_J$  are far detuned and do not affect the level splitting. Away

from the  $B = B_0$  resonance conditions the two-level model and the full calculation begin to diverge. This is because the magnetic dipole moments are not truly constant as assumed in the simple model, but will both vary independently with respect to an increasing magnetic field. The observed splitting between the state pair closely matches the expected trend.

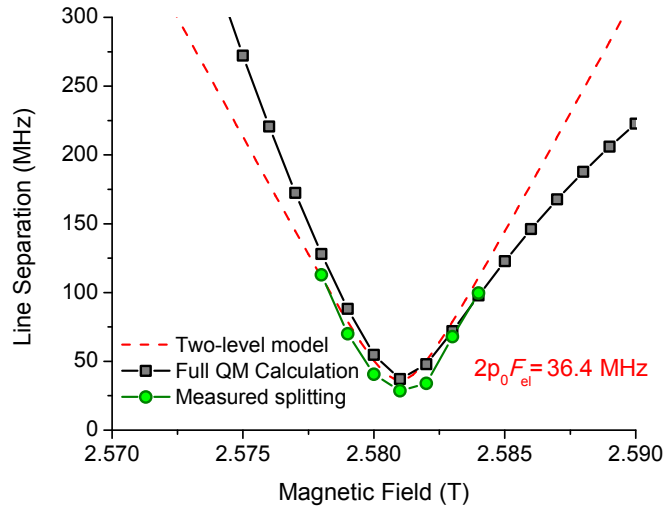


Figure 4.15: Comparison between observations, the two-level model and the full quantum mechanical calculation of the line splitting between the even and odd states, as a function of applied magnetic field. Here the observed  $B_0 = 2.576$  T has been shifted to matched the calculated  $B_0 = 2.581$  T.

Finally, comparing the observed ratio of count rates for the two levels in question ( $\Pi_z$ -even over  $\Pi_z$ -odd) versus magnetic field value shows a similarly close agreement. As shown in Fig. 4.16, the ratio trends towards equal excitation when the dipole interaction term is the dominant component of the level splitting. Once again, the observed values match up well with the results of the full quantum mechanical treatment.

This magnetic-field control allows one to shift pairs of remaining vibrator-state pairs of the same  $m_J$  but opposite  $\Pi_z$  into resonance with one another. These states, now in exact resonance, can then be subjected to a parallel electric field  $F_{el}$  in order

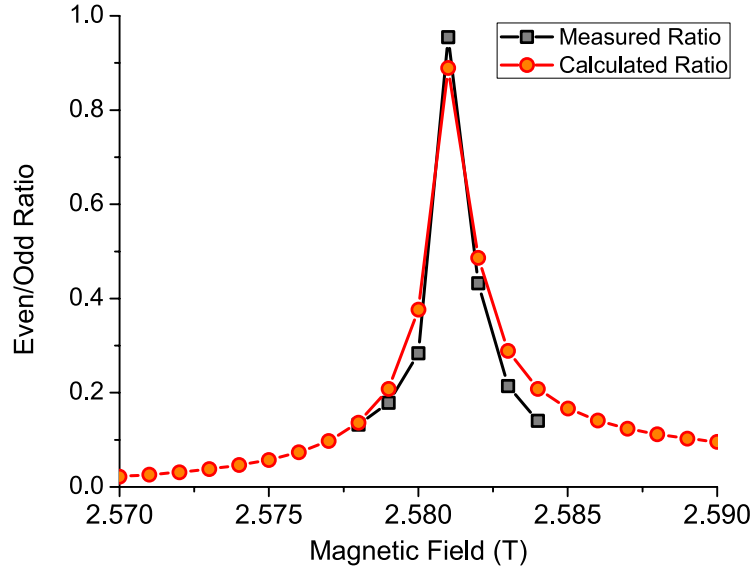


Figure 4.16: Comparison between experimentally-measured ratio of the  $m_J = 3/2$ ,  $\Pi_z = \text{even}$  peak and the  $\Pi_z = \text{odd}$  peak versus magnetic field offset  $B_0$ , with an applied electric field of  $F_{\text{el}} = 1 \text{ V/m}$ .

to form highly polar non-degenerate states with large electric dipole moments that are fairly insensitive to  $F$  due to their large detuning from other levels. Choosing an electric field  $F_{\text{el}}$  of a few 10 V/m separates the polar states shown here by several 100 MHz. This scale of splitting, under an experimentally-achievable electric field, is ideal for Rydberg-atom interaction schemes that require atoms in well-defined, non-degenerate and highly polar states. Potential applications, including the Rydberg excitation blockade and the development of a phase gate, are discussed in Sec. 5.6 of the following Chapter.

## CHAPTER V

### Rydberg atom calculations

#### 5.1 Level calculations

The presented experimental results can be better understood by conducting numerical calculations to determine the Rydberg spectra and wavefunctions in parallel electric and magnetic fields. The electric-dipole and the diamagnetic matrix elements required for the diagonalization of the Hamiltonian in Eq. 2.2 are computed with numerically obtained Rydberg electron wavefunctions. Previously published values [3, 98] are used for the fine structure parameters and the quantum defects.

Since only parallel electric fields are included here, the  $m_J$  manifolds can be treated separately. For each possible  $m_J$  value of  $1/2$ ,  $3/2$  or  $5/2$ , a separate spherical basis set that includes all states with principal quantum numbers between 10 and 90 is used. The value of  $m_J$  is thus fixed for any given diagonalization. The Hamiltonian matrix is numerically diagonalized for given field value parameters  $B$  and  $F_{el}$  using Lapack routines. Energy levels and excitation amplitudes from the intermediate  $5P_{3/2}|m_I = 5/2, m_J = 3/2\rangle$  state are calculated for the optically accessible manifolds  $m_J = \{1/2, 3/2, 5/2\}$ . Figures 4.9B and 4.11B show the resulting calculated spectra and transition amplitudes over the same spectral region that was used in the experiment (part A of the Figures). Here, the transition amplitude into a Rydberg state  $|\psi\rangle$  is

defined as the square root of the non-saturated excitation rate,  $4\Omega_R^2/\Gamma$ , where the parameter  $\Gamma$  is the effective bandwidth of the optical excitation (in  $\text{s}^{-1}$ ), and  $\Omega_R$  is the Rabi frequency (in  $\text{s}^{-1}$ ):

$$\Omega_R = -\frac{eF_0\hat{\epsilon}}{\hbar} \cdot \langle\psi|\hat{\mathbf{r}}|5P_{3/2}, m_J = 3/2\rangle \quad (5.1)$$

Here the laser field amplitude is denoted as  $F_0$ , the electric dipole operator as  $-e\hat{\mathbf{r}}$ , and the polarization unit vector as  $\hat{\epsilon}$ . By plotting the square root of the excitation rate, a wider range of values can be plotted, and the amplitudes shown in Figures 4.9B and 4.11B are proportional to the Rabi frequency. For the manifolds  $m_J = \{1/2, 3/2, 5/2\}$ , the polarization unit vectors in the calculation are set to  $\hat{\epsilon} = \{\hat{x}, \hat{z}, \hat{x}\}$ , respectively. The effective level width is set to  $\Gamma = 2\pi \times 10$  MHz, according to typical experimentally observed linewidths. The laser electric field  $F_0$  is set in accordance with an intensity of  $I = 2 \times 10^6$  mW/cm<sup>2</sup>, as used in the experiment.

The resulting energy level structure can be compared to experimental data, as shown in both Figs. 4.9B and 4.11B in Chap. IV. These plots reveal excellent agreement between calculated and experimental results, both in terms of absolute frequency and relative line strengths. Further, by comparing several calculations of varying basis size and looking at the resulting discrepancies, we find our simulated spectra for the given basis size of  $n = 10$  to 90 to be useful up to energies of about  $-20$  cm<sup>-1</sup>. Best agreement between experimental and simulated spectra is obtained when the simulated magnetic fields are taken to be 0.005 T higher than the ones used in the experiment, corresponding to a discrepancy of 0.2 %. This magnetic-field offset is consistent from day to day, and is believed to be due either to a calibration error in the magnet system, or due to a minor variation of the main trap magnet over about ten years of use.

## 5.2 Magnetic and electric dipole moment statistics

These calculations can also be used in order to obtain the distributions of electric and magnetic dipole moments of Rydberg levels in selected spectral regions. In particular, we are interested in examining the abundance of state pairs similar to the one labeled “X” in Fig. 4.9. Such otherwise-isolated pairs with strong electric dipole moments are Rydberg-Rydberg interaction candidates.

The instantaneous magnetic dipole moments are calculated by slightly incrementing the magnetic field by a small step of  $\Delta B = 0.001$  T at  $F_{\text{el}} = 0$ , and comparing the resulting change in energy of each individual state. The results can be used to predict the magnetic trapping behavior of the Rydberg levels. For  $B = 2.581$  T, there are 697 total states ( $\{248, 232, 217\}$  in each respective sublevel) between the interval from  $-60$   $\text{cm}^{-1}$  to  $-50$   $\text{cm}^{-1}$ . This is all within the  $n$ -mixing regime, representing the region about the experimentally-observed lines at  $\sim -55$   $\text{cm}^{-1}$ . As shown in the histograms in Fig. 5.1A, within this interval the probability distributions of the magnetic moment exhibit fairly well-defined bell-shaped maxima. The magnetic dipole moments are quite large, with means  $\{-10.8 \mu_{\text{B}}, -12.1 \mu_{\text{B}}, -13.3 \mu_{\text{B}}\}$  for the respective optically accessible manifolds  $m_{\text{J}} = \{1/2, 3/2, 5/2\}$ . The standard deviations are  $\{4.0 \mu_{\text{B}}, 4.8 \mu_{\text{B}}, 5.5 \mu_{\text{B}}\}$ . The extreme values are  $0 \mu_{\text{B}}$  and  $-27 \mu_{\text{B}}$ .

Knowledge of the electric dipole moments is important, for instance, to estimate the permanent-electric-dipole interaction between Rydberg atom pairs. The permanent electric dipole moments of the states are determined by performing two calculations with parallel electric fields  $F_{\text{el}} = 3$  V/m and  $F_{\text{el}} = 3.3$  V/m, and calculating the energy shift of each state. As shown in Fig. 5.1B, the distributions of magnitudes of the electric dipole moments are peaked at values below  $100 ea_0$ , while

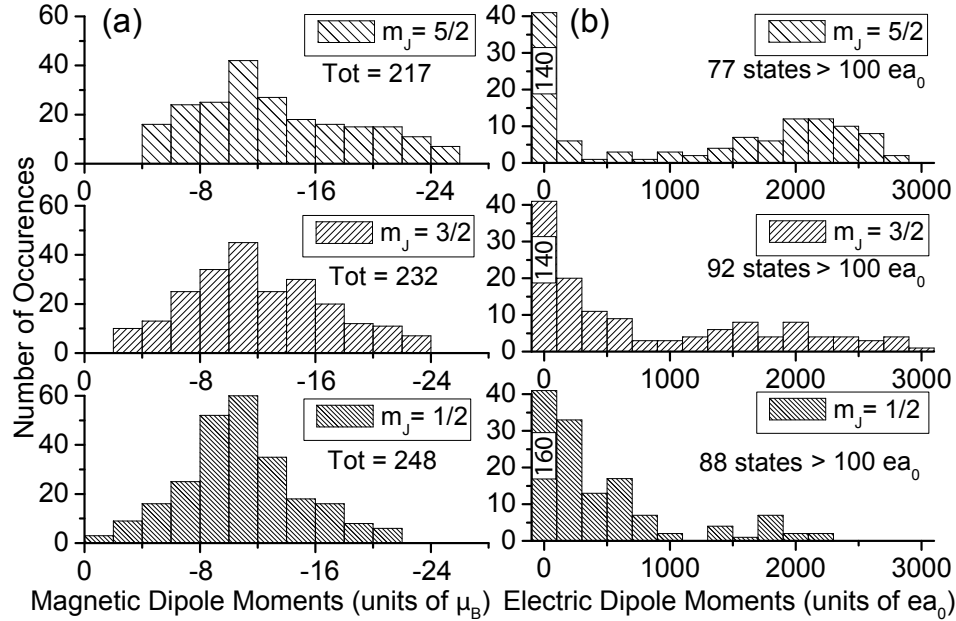


Figure 5.1: A) Histograms of all magnetic dipole moments in the interval from  $-60 \text{ cm}^{-1}$  to  $-50 \text{ cm}^{-1}$ , for  $B_{\text{th}} = 2.581 \text{ T}$ . For each value of  $m_J$ , the total number of Rydberg states in this interval is indicated below the legend. B) Histograms of all electric dipole moment magnitudes, for the same energy interval and magnetic field value, with an applied electric field of  $F_{\text{el}} = 3 \text{ V/m}$ . For clarity, the bars with dipole moments  $< 100 ea_0$  are cut off at height 40, with the number of occurrences indicated on the bar.

typical averages are  $400 ea_0$  and standard deviations  $800 ea_0$ . The distributions of the electric-dipole magnitudes tend to have bi-modal shapes, with a dominant first group of states close to zero and a second group with electric dipole moments up to a few thousand  $ea_0$ . Most energy levels in the  $n$ -mixing regime are clearly non-degenerate, resulting in small electric polarizabilities and small electric dipole moments at low values of  $F_{\text{el}}$ . This majority of levels gives rise to the first group in the electric-dipole distributions. The second group is due to remnant pairs of near-degenerate vibrator states of opposite parity and similar overall shape, such as the state pair “X” observed in Figs. 4.9 and 4.10. While the number of states in the second group is much smaller than in the first, their large electric dipole moments drive up the magnitudes of the averages and standard deviations.



### 5.3 Interacting line pair statistics

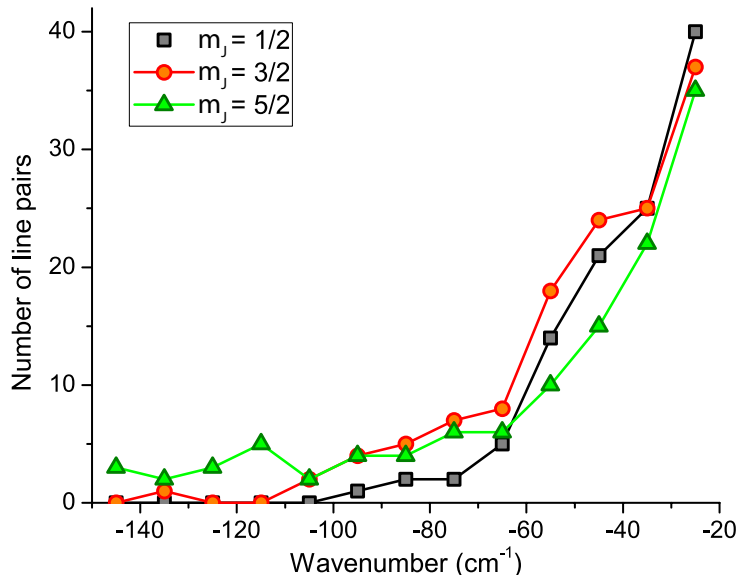


Figure 5.2: Number of interacting state pairs with electric dipole moments  $|p| > 100ea_0$  and of similar magnitude (within 30 %), binned in increments of  $10 \text{ cm}^{-1}$ . The three optically-available  $m_J$  states are shown.

The abundance of state pairs with large and approximately opposite electric dipole moments, such as the “X” and “Y” pairs in Fig. 4.9, is of primary interest for applications that involve electric-dipole Rydberg atom interactions. I determine the number of such pairs by parsing the computed spectra for pairs of neighboring lines with same  $m_J$  and large, opposite electric dipole moments of similar magnitude (to within 30 %). The abundance of line pairs is shown in Fig. 5.2, binned into increments of  $10 \text{ cm}^{-1}$ . Such pairs are a rare occurrence at energies below  $\sim -65 \text{ cm}^{-1}$ , owing to the small size of the atoms and the lower density of states. Above  $-65 \text{ cm}^{-1}$  the number of line pairs rapidly increases in number. Within the considered energy range  $-60 \text{ cm}^{-1}$  to  $-50 \text{ cm}^{-1}$ , the manifolds  $m_J = \{1/2, 3/2, 5/2\}$  include a total of 697 levels. The numbers of pairs with electric dipole moments greater than  $100 ea_0$  and with excitation amplitudes larger than  $0.3 \times 10^3 \text{ s}^{-1/2}$  (corresponding to the

experimental excitation limit) are  $\{14, 17, 10\}$ . Figure 5.3 shows the distribution of these pairs versus dipole moment and excitation amplitude. One can observe a weak trend in Fig. 5.3 that excitation amplitude diminishes with dipole moment. However, even for the highest dipole moments, which are of order  $2000 ea_0$ , one can still find state pairs with fairly large excitation amplitudes (states within the dotted region in Fig. 5.3).

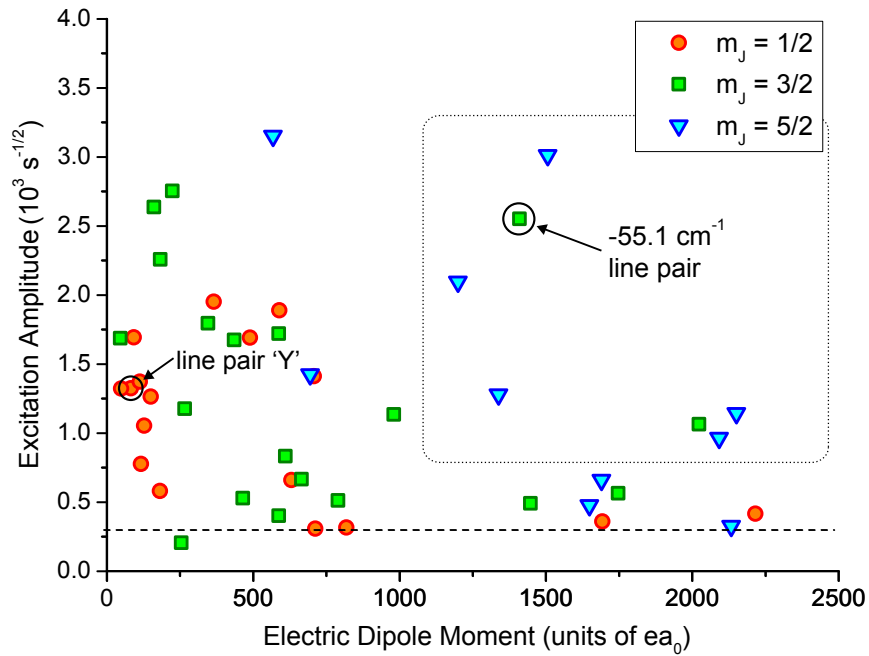


Figure 5.3: Scatter plot of line pairs with electric dipole moments  $> 100 ea_0$  at  $B_{\text{th}} = 2.581$  T and  $F_{\text{el}} = 3$  V/m, for the energy range between  $-60 \text{ cm}^{-1}$  and  $-50 \text{ cm}^{-1}$ . The pairs are plotted versus dipole moment and excitation amplitude. The dashed line indicates our experimental excitation-amplitude limit above which lines can be easily observed.

I have used the calculations to test our detailed experimental analysis of the “X” pair of states. Using a procedure equivalent to the one used in Fig. 4.12, by varying the magnetic field we obtain the resonant magnetic field value at which the level pair is degenerate. For this state pair, the theoretical resonant magnetic field value of  $B_{\text{th}} = 2.581$  T. As mentioned above, this value differs by  $0.005$  T from the experimentally observed one ( $B_{\text{exp}} = 2.576$  T). The calculated magnetic

dipole moments of the  $\Pi_z$ -odd and  $\Pi_z$ -even states of the “X” pair are  $-9.4 \mu_B$  and  $-11.6 \mu_B$ , respectively. These values agree well with the measured values of  $-9.2 \mu_B$  and  $-11.7 \mu_B$  from Fig. 4.12. Further, the calculations yield an average electric dipole moment of  $1410 ea_0$  for the “X” pair. This value compares well to the measured value of  $1500 ea_0$ . The 7 % discrepancy arises from the uncertainty of the exact position of the excitation region within the inhomogeneous applied electric field. Also, in the experiment the electric field might have a very small component transverse to the magnetic field, which is not included in the calculations.

In this Section I have shown that there exist several state pairs that show both high excitation amplitudes and strong coupling as manifested by the large and opposite electric dipole moments. These pairs are otherwise isolated and non-degenerate, making them ideal for interaction applications. Control over the large bias magnetic field allows us to tune any particular pair into exact degeneracy. In this case, the states will become mixed and manifest strong electric dipole moments already at low electric field values.

#### 5.4 Wavefunction overlap

In order to further explore the nature of these state pairs that show large electric dipole moments, we have calculated and plotted the wavefunctions of the Rydberg line pairs at  $-55 \text{ cm}^{-1}$ . Figure 5.4 shows a plot of the wavefunction probabilities for the “X” pair of states at  $B_{\text{th}} = 2.589 \text{ T}$  and  $F_{\text{el}} = 0$ . Here, the blue/red color scheme has been added in to show the sign of the wavefunction amplitudes, indicating whether the state is  $\Pi_z$ -even or  $\Pi_z$ -odd. The wavefunction structures reiterate that the “X”-pair represents an instance of a remnant pair of vibrator states in the  $n$ -mixing regime. The wavefunctions of both states have closely matched spatial

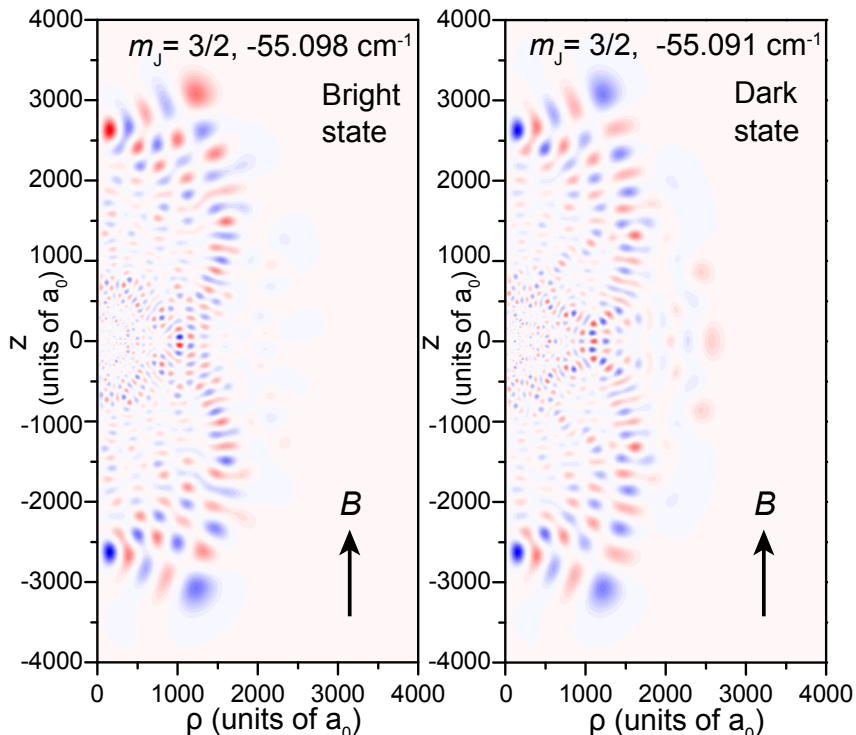


Figure 5.4: Calculated normalized electron wavefunction probabilities  $P = |\psi(\mathbf{r})|^2 r \sin \theta$  for the X line pair at  $-55.1 \text{ cm}^{-1}$  with  $B_{\text{th}} = 2.589 \text{ T}$  and  $F_{\text{el}} = 0 \text{ V/m}$ . The color scale is added to indicate whether the wavefunction is  $\Pi_z$ -even or odd.

distributions, being relatively constrained within the  $xy$ -plane and elongated along the  $z$ -axis. Close inspection reveals that the two wavefunctions differ slightly in the exact amount of admixtures of states that extend in the  $xy$ -plane (region near  $z = 0$  and  $\rho \gtrsim 2000 a_0$ ). This difference gives rise to the discrepancy between the two magnetic dipole moments ( $-9.4 \mu_B$  versus  $-11.6 \mu_B$ ), which in the experiment I have employed to tune the level pair into resonance at  $F_{\text{el}} = 0$  (see Sec. 4.6). The large size of the electric dipole moments that result from the  $F_{\text{el}}$ -induced coupling between these two states stems from the fact that their wavefunctions have similar spatial extents and node line patterns. The probability distributions of the wavefunctions of the coupled states under an applied electric field of  $F_{\text{el}} = 3 \text{ V/m}$  are shown in Fig. 5.5. The coupled states are the symmetric and anti-symmetric superpositions of the two initial state wavefunctions at  $F_{\text{el}} = 0$ . It is clear from Fig. 5.5 that in the

presence of an electric field the coupled states have large and opposite permanent electric dipole moments.

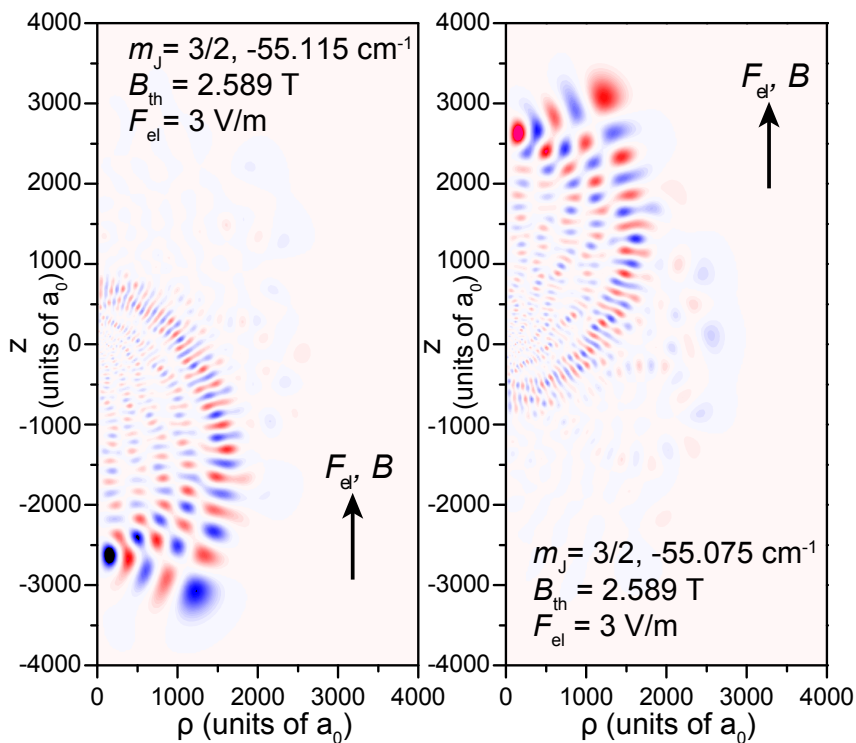


Figure 5.5: Calculated normalized electron wavefunction probabilities  $P = |\psi(\mathbf{r})|^2 r \sin \theta$  for the  $X$  line pair at  $\sim -55.1 \text{ cm}^{-1}$  with  $B_{\text{th}} = 2.589 \text{ T}$ , with a weak parallel electric field of  $F_{\text{el}} = 3 \text{ V/m}$ . The  $F_{\text{el}}$ -induced coupling leads to the displayed states with large permanent electric dipole moments.

## 5.5 Classical trajectory calculations

To conclude our theoretical considerations, we have also performed a set of classical trajectory calculations that demonstrate the vibrator character of the “X”-pair of levels. The trajectory calculations also show that the “X”-pair and other remnant vibrator states in the  $n$ -mixing regime are associated with a classically regular domain of phase space, where classical and quantum dynamics exhibit close correspondence. Figure 5.6A displays two trajectories of a classical Rydberg electron at  $B = 2.580 \text{ T}$ , energy  $-55.1 \text{ cm}^{-1}$  and electric field  $F_{\text{el}} \approx 0$ . Initial conditions are chosen such that the trajectories mimic the wavefunction probabilities in Figs. 5.4

and 5.5. Over short time scales, the trajectories are Kepler-like. Over longer times the eccentricity and alignment of the electron orbit vary in a periodic fashion. The alignment wobbles about the  $z$ -direction, which is why such quantum states have been labeled as “vibrator states”. At  $F_{\text{el}} = 0$ , the trajectories displayed in Fig. 5.6A are exactly equivalent. The wavefunction probabilities of corresponding quantum states must mimic the sum of the point densities of the two equivalent trajectories. Figure 5.6A indeed closely resembles the wavefunction probabilities in Fig. 5.4. If a weak parallel electric field is added, both classical and quantum degeneracies are lifted. In that case, the wavefunction probabilities of corresponding quantum states mimic the point density of only one of the two trajectories. This applies to the wavefunction probabilities shown in Fig. 5.5, which closely resemble Figs. 5.6B and 5.6C. This is a demonstration of the quantum-classical correspondence [94], where the spatial distribution of the quantum mechanical wavefunction coincides with a projection of the classically-calculated phase space of the same potential.

## 5.6 Applications

### 5.6.1 Excitation blockade

Dipolar states of Rydberg atoms in strong magnetic and weak parallel electric fields are good candidates for Rydberg-atom interaction studies and applications thereof. They are non-degenerate and have high optical excitation rates from low-lying atomic states. The “X”-pair states serve as a good example, and have dipole moments of  $p_0 \approx 1500 ea_0$ . The electric-dipole interaction energy between two such atoms,  $E_{\text{dd}} \sim p_0^2/(4\pi\epsilon_0 d^3)$ , amounts to several tens of MHz at a distance  $d = 5 \mu\text{m}$ . This level of interaction strength is within the desirable range for quantum information applications. For instance, the implementation of a C-NOT gate akin to Ref. [55] would require optical excitation pulses of less than about  $1 \mu\text{s}$  in duration,

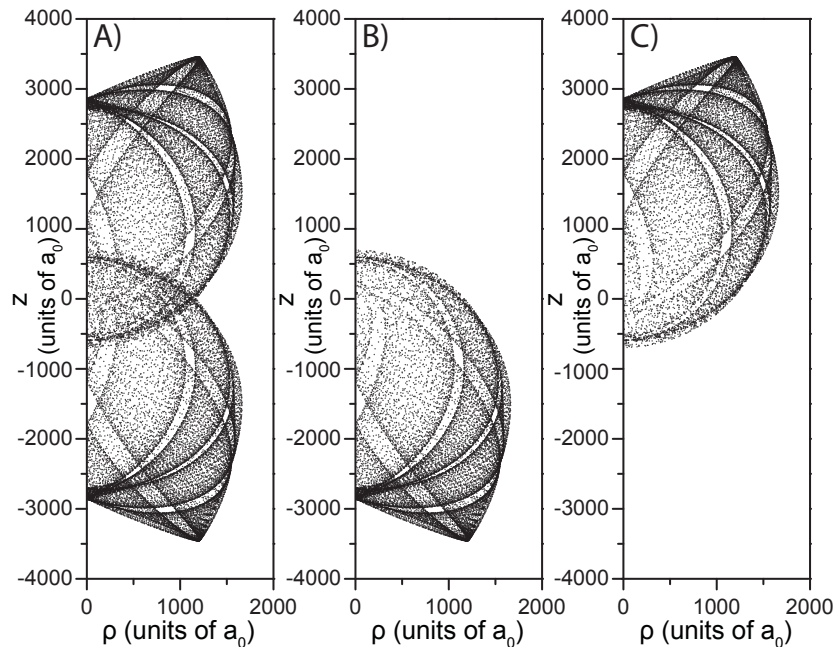


Figure 5.6: Classical electron trajectories at an energy of  $\sim -55.1 \text{ cm}^{-1}$ ,  $B_{\text{th}} = 2.580 \text{ T}$ . The simulated trajectory duration is 137 ns and the electron position is plotted every 8.2 ps. At  $F_{\text{el}} = 0$ , the sum of the point densities of two equivalent trajectories (A) mimics the wavefunction probabilities in Fig. 5.4. At small but non-zero  $F_{\text{el}}$ , the point densities of individual, slightly non-degenerate trajectories (B and C) mimic the wavefunction probabilities in Fig. 5.5.

leading to total gate times of a few  $\mu\text{s}$ . This is fast enough that atomic decay can largely be neglected.

### 5.6.2 Phase Shift

As a second example of quantum control, consider a pair of Rydberg atoms in one of the “X”-pair levels at a distance  $d = 10 \mu\text{m}$ , in a magnetic field where the two states are non-degenerate and separated by an energy defect  $\Delta E = h \times 100 \text{ MHz}$  at  $F_{\text{el}} = 0$ . A smooth electric-field pulse  $F_{\text{el}}(t)$  that begins and ends at  $F_{\text{el}} = 0$  is applied. The time-dependent electric-dipole moment is then:

$$p(t) = \frac{F_{\text{el}}(t)p_0^2}{\sqrt{\Delta E^2/4 + F_{\text{el}}(t)^2 p_0^2}} \quad (5.2)$$

The acquired interaction-induced phase is:

$$|\Delta\phi| \sim \int \frac{p^2(t)}{(4\pi\epsilon_0\hbar d^3)} dt \quad (5.3)$$

As shown in Fig. 5.7, to implement a  $2\pi$  phase shift with an electric dipole moment of strength  $p_0 \approx 1500 ea_0$ , an electric-field pulse with a peak field of several V/m and a duration of about  $1 \mu\text{s}$  would be needed. This is short compared to the atomic lifetime, but long enough to ensure adiabatic evolution (which requires a ramp duration  $t_{\text{ramp}} \gg \hbar/(\Delta E) = 10 \text{ ns}$ ). With the addition of individual site control, it would be possible to effect such a phase shift scheme within the present experiment.

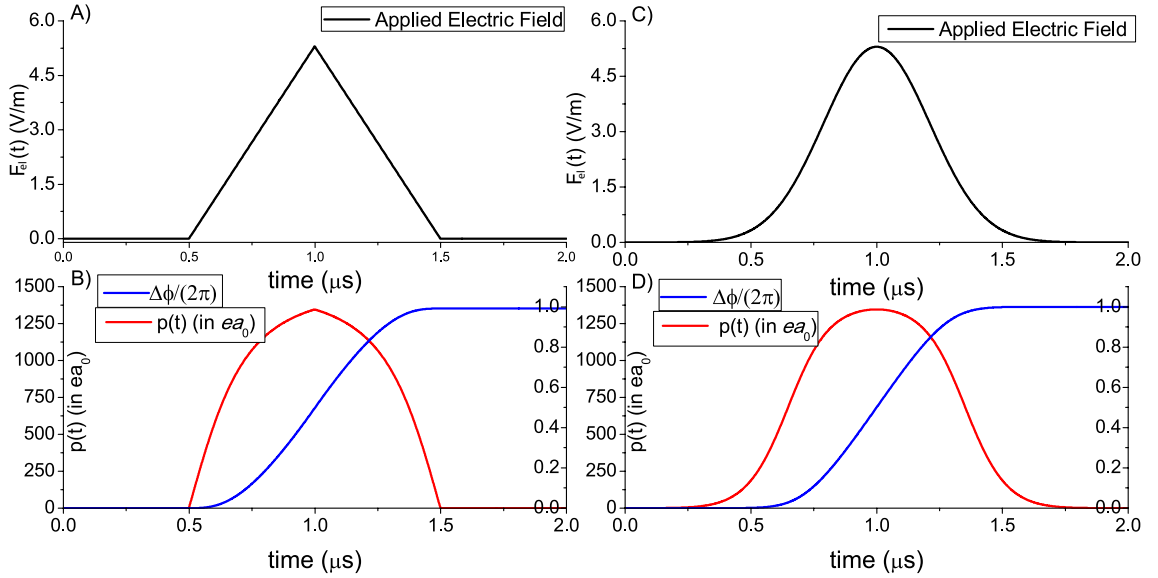


Figure 5.7: Applied electric field pulse versus time, and resulting dipole moment  $p(t)$  and phase shift  $\Delta\phi$ . A) and B) show the case of a triangle pulse of maximal electric field  $F_{e1} = 5.3 \text{ V/m}$ , while C) and D) show a more realistic Gaussian pulse shape, with  $\sigma = 212 \text{ ns}$  at the same height as in A).

## 5.7 Summary

In the previous Chapter, I presented experimental studies of rubidium Rydberg states in parallel electric and magnetic fields, in the  $n$ -mixing regime. The energy



level distribution contains residual pairs of near-degenerate vibrator states embedded in an otherwise non-degenerate spectrum. Small changes of the  $B$ -field have been used to tune a sample pair of such states into resonance. An additional weak, parallel electric field has then been applied to prepare states with large electric dipole moments.

To provide a theoretical framework for these experimental observations, the experimentally observed spectra are reproduced here by calculating the states via the high-magnetic-field Hamiltonian. The resulting energy levels show excellent agreement with the observed Rydberg levels, in terms of the energy levels within each Rydberg manifold, the relative excitation rates, and the magnetic and electric dipole moments. The presented wavefunction calculations in this Chapter also confirm our understanding of the cause of the strong electric dipole moments within the interacting line pairs.

Our calculations reveal that within the  $n$ -mixing regime, there exist several such line pairs with strong permanent electric dipole moments in the presence of a small electric field  $F_{\text{el}}$ . With known state level behavior with respect to the magnetic field  $B$ , the resonance magnetic field condition  $B_0$  can be identified for each near-degenerate line pair within the Rydberg manifolds. Moreover, a large change in  $B$  by several hundred Gauss has the effect of completely changing the Rydberg spectrum at these higher energy levels, detuning some interacting line pairs and bringing other states of the same  $m_J$  and opposite axial parity into resonance. As shown in Chapter III, the high-field trap can operate over a wide range of magnetic field values by controlling the dipole field coil current. The state level calculations can therefore be used to identify the exact experimental parameters that would produce a line pair for the given electric dipole moment strength, or within the desired energy

range. This gives Rydberg-Rydberg interactions studies a great deal of flexibility; using an additional tuning parameter in the magnetic field  $B$  offers a much larger degree of control over the specific properties of the interacting system.

## CHAPTER VI

### Trap limitations and future directions

#### 6.1 Summary

In this work, I have investigated the cooling and trapping dynamics of both common isotopes of rubidium ( $^{85}\text{Rb}$  and  $^{87}\text{Rb}$ ) within a high-magnetic-field trap. The trap performance has been characterized in magnetic fields ranging from 1-3 Tesla, and the loss mechanisms have been studied. Currently, within a magnetic field of 2.6 T the trap can hold up to  $2 \times 10^7$  atoms, contained within an elliptically-shaped potential well. The trap's typical axial and transverse FWHM is  $4.0 \text{ mm} \times 2.2 \text{ mm}$ , giving a resulting density of  $10^9 \text{ atoms/cm}^3$ . These atoms are cooled down to temperatures approaching the Doppler limit of  $\sim 150 \mu\text{K}$ . The trap lifetime is dependent on the magnetic field (and potential well depth), but for a field of 2.6 T has a typical value of  $\tau \sim 20 \text{ s}$ . This is caused by imperfections and power imbalances within the low-intensity molasses or cooling beams.

I demonstrated that such dense cold atom samples are an ideal platform for Rydberg atom interaction experiments. Using a two-step excitation process with narrow-band pulsed lasers, atoms are excited to Rydberg states within large magnetic fields of  $\sim 2.6 \text{ T}$ . The observed Rydberg spectrum agrees well with state-level calculations over a large energy range, as well as in the presence of a weak parallel electric field

$F_{\text{el}}$ . Auto-ionization levels above the field-free ionization threshold have also been investigated.

Within the  $n$ -mixing regime, I have observed the presence of strongly-interacting near-degenerate state pairs of the same  $m_J$  quantum number, and have examined their abundance and typical characteristics. Such pairs of states with opposing axial parity (one  $\Pi_z$ -even, one  $\Pi_z$ -odd) can have wavefunctions that are extended in the axial directions. The presence of an applied electric field then forms symmetric and anti-symmetric linear combinations, resulting in the formation of highly-polar states. As shown in subsequent calculations, this strong polar character is due to the similar extent and node line patterns of the original wavefunctions. Near-degenerate state pairs can also be selectively tuned into exact resonance via careful control of the large applied offset magnetic field  $B_0$ . This gives a much greater degree of experimental control as compared to low-field systems in terms of the energy range involved (through selection of a particular state pair), as well as the interaction strength.

### 6.1.1 Current trap limitations

The high-magnetic-field trap is an important achievement, giving access to a new regime for cold atom studies. However, the current-generation apparatus can be improved upon. Presently, one major limitation is the atom density. Under optimal conditions at 2.6 T,  $\sim 2 \times 10^7$  are trapped in a volume with an axial FWHM of 4 mm, and a transverse FWHM of 2.2 mm. This gives a density of  $n_{\text{at}} \sim 10^9 \text{ atoms/cm}^3$ , which falls on the lower end of the typical density spectrum for low or zero magnetic field atom traps such as MOTs. This also corresponds to a Wigner-Seitz radius  $[(4\pi/3)n_{\text{at}}a_{\text{WS}}^3 = 1]$  of approximately  $6 \mu\text{m}$ . In order to investigate and study atom-atom interactions, the Wigner-Seitz radius would need to be below the ‘blockade

radius’, or radius within which the Rydberg-Rydberg interactions cause a large energy detuning of the Rydberg level and therefore inhibit multiple excitations. As seen in Eq. 1.1, the dipole-dipole interaction scales as the square of the dipole moment divided by the distance cubed. Assuming a permanent dipole of  $p_0 = 1500ea_0$  as observed within the experiment for energies of  $-55 \text{ cm}^{-1}$  (seen in Section 4.5), an inter-atom separation of less than  $6 \text{ }\mu\text{m}$  is needed to achieve an energy shift of 10 MHz. For these interaction strengths, our maximally-achievable experimental densities places the Rydberg atom density just below that of the desired blocked regime.

## 6.2 Trap Improvements

### 6.2.1 Dipole trap

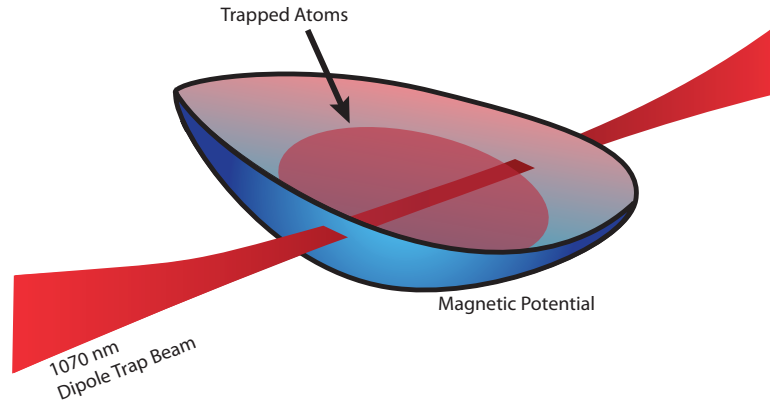


Figure 6.1: Sketch of a dipole trap overlapped with the magnetic potential minimum. The dipole trap crosses the trapped atoms along the transverse plane, focused at the center of the potential.

One possible method of achieving the desired atom density range would be to increase the curvature or ‘steepness’ of the confining potential. Although along the transverse directions ( $x$ - $y$  plane) this is governed by the current in the quadrupole coils, at our current operating limits the trap still falls short of the desired density. An increase in density on the order of 5-10 is desired. As diagrammed in Fig. 6.1, by

applying a focused off-resonant laser beam it is possible to add a second conservative potential to the trapping region and generate an effectively steeper potential well for ground state atoms at the center of the high-field trap. Preliminary efforts in this direction are already underway, with the injection of a 1070 nm beam (maximal power  $\sim 6$  W) through one of the transverse ports, such that it crosses the trap in a perpendicular fashion to the  $B$ -field axis. The resulting dipole trap has a maximal depth of [99]:

$$W = \frac{3\pi c^2 \Gamma}{2w_0^3 \delta} I_0 \text{Exp}\left[-2\frac{r^2}{w_0^2}\right] \quad (6.1)$$

Here,  $w_0$  is the angular frequency of the transition,  $w_0 = 27\mu\text{m}$  is the beam waist,  $\Gamma = 2\pi \times 6.066$  MHz is the natural linewidth of the 5S-5P transition,  $\delta = w_0 - w$  is the detuning of the laser frequency  $w$ , and  $I_0$  is the laser intensity at the focus [ $2P/(\pi w_0^2)$ ]. For 5 W of power at  $\lambda = 1070$  nm, this gives a depth of 11.5 MHz.

At the applied wavelength of 1070 nm of the dipole trap, the 5S-5P cooling transition will see a further shift as the dynamic polarizabilities of the two states are both different and opposite in sign:  $\alpha_\nu(5\text{S}) = 770$  and  $\alpha_\nu(5\text{P}) = -600$  in atomic units [ $\alpha_{\text{SI}} = (4\pi\epsilon_0)a_0^3 \alpha_{\text{au}}$ ] [100]. This means that the 5P level is similarly shifted within a 5 W dipole trap, but blue detuned by  $11.5 \text{ MHz} \times (600/720) = 9.5$  MHz. The total transition shift is then of approximately 20 MHz.

Figure 6.2 shows the resulting potential of a 5 W optical dipole trap being overlapped with the high-magnetic-field trapping potential, operating at a field of  $B_0 = 2.6$  T. The shape of the potential shows a significant drawback to this approach. Since the Rayleigh length of the beam is quite long ( $z_{\text{R}} = \pi w_0^2/\lambda = 2$  mm), the resulting potential allows the cooled atoms to drift much further out from the trap center. Because of the large transverse magnification along the  $x$ -direction,

only the central portion of the trap with  $r_x < 0.5$  mm is detected. For the case of dipole traps overlapped with a MOT, the high-intensity molasses beams (of several  $I_{\text{SAT}}$  each) add a large restoring force to the system. Here, the low beam intensities ( $I \approx 0.02 I_{\text{SAT}}$  per beam) within the high-magnetic-field trap work put it at a significant disadvantage compared to MOTs. This intensity is about 100 times less than in a typical low-field MOT, and the resulting single-beam scattering rates are only  $\sim 4000 \text{ s}^{-1}$  at this intensity and detuning.

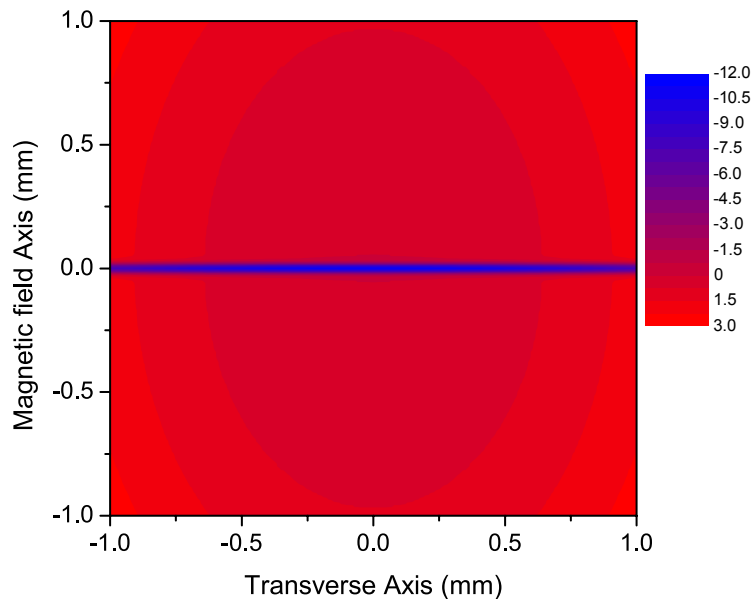


Figure 6.2: Contour plot of the trapping potential (in MHz) with the addition of a dipole trap with  $P = 5 \text{ W}$ ,  $w_0 = 27 \mu\text{m}$ . The presence of the dipole trap adds a small confining potential of 11 MHz depth at the center of a broad local minimum.

In order to solely excite atoms located within the dipole trap, rather than the entire  $4 \text{ mm} \times 2.2 \text{ mm}$  elliptical trapping region, a separate 780 nm 5S-5P excitation beam was co-propagated with the 1070 nm dipole trap beam and simultaneously focused into the trap with a beam waist of  $w_0 \approx 30 \mu\text{m}$ . Similarly the 479 nm ionization laser was focused down to a small size ( $w_0 \approx 30 \mu\text{m}$ ) and overlapped at a slight angle. This resulted in a small excitation volume overlapped with the dipole

trap beam. I then performed a pulsed experiment where short simultaneous pulses ( $20 \mu\text{s}$ ) of 780 nm and 479 nm light gave a free-electron signal via direct ionization. The 5S-5P transition laser was then scanned over across the transition, for several dipole beam power values. Figure 6.3A shows the effect of applying the focused dipole beam to the high-magnetic-field trap; the strength of the 5S-5P transition resonance diminishes in proportion to the applied dipole beam power. However, no blue-detuned (high-frequency) increase in signal is observed. Although it is possible in this manner to detect the presence of the dipole potential via the reduction in signal, atoms are not being trapped within the optical potential. Instead, either the atoms are traveling through the steep conservative potential without losing enough kinetic energy to become trapped, or they are even being lost in the transverse direction, as the dipole trap lowers the total potential along the channel of the optical dipole trap. As an example of a dipole trap, Fig. 6.3B shows the case of dipole trap aligned onto a low-field MOT; a second peak on the high frequency side of the transition signal the presence of atoms trapped within this steeper potential.

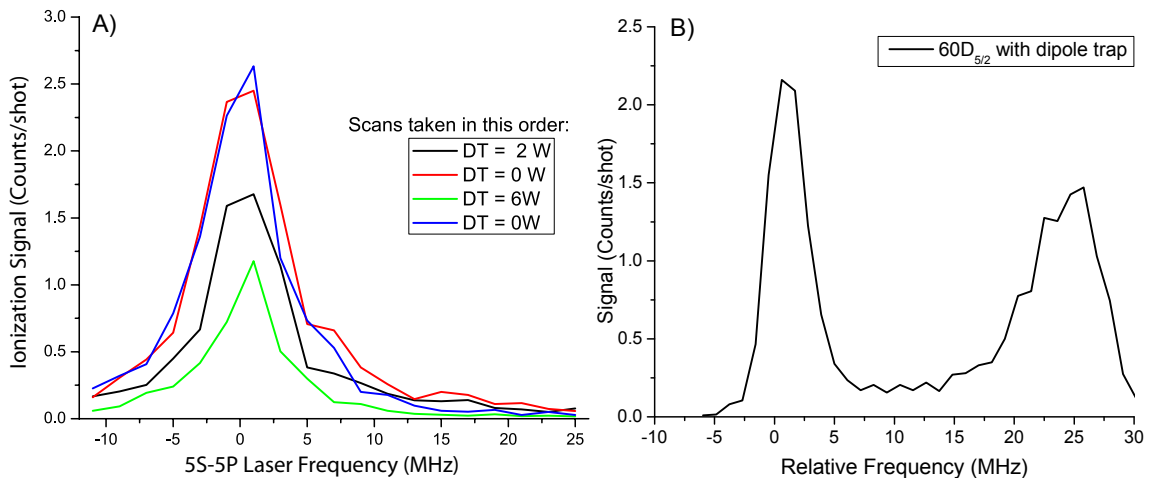


Figure 6.3: A) Scan taken with the dipole trap being applied, at 2 W and 6 W. The dipole trap lowers the atom density, since no additional transverse confinement is provided with this additional detuning. B) Sample scan from a low-field MOT, with an optimized dipole trap. The second peak on the blue-detuned side of the transition arises from the presence of the dipole trap.



### 6.2.2 Dipole trap schemes

There are a couple possible methods to improve upon this dipole trap and enable increased atom confinement within the dipole trap. A dipole trap beam with a smaller beam waist would have a corresponding smaller Rayleigh length, resulting in a shorter dipole trap focus. This is currently limited by the combined factors of the physical chamber size (the closest position for optical components is at a distance of 35 cm), and the small size of the optical ports ( $d \approx 1$  cm). A second approach would be to apply an additional focused cooling beam with independent frequency control, incident from both directions and aligned with the dipole trap beam. This would provide increased confinement along the dipole beam axis and provide a cooling mechanism for atoms within the dipole trap. However, this focused cooling beam would be blue-detuned for the rest of the high-magnetic-field trap, so any misalignment would heat the trapped atoms and eject them from the trap. Additionally, such an approach would require careful intensity and polarization equilibrations of this pair of focused cooling beams, so as to avoid a net directional force that would rapidly deplete the trap.

Another tactic would be to apply two crossed dipole beams. This would give steep confinement along all three axes. However, this approach still does not account for the additional detuning of the cooling transition that effectively prevents atoms from being captured within the steeper well.

One final approach would be to overlap two dipole trap laser beams of separate wavelengths. The 5P state polarizability, which creates the additional detuning, is also dependent on the frequency of the dipole laser beam. Though the 5P polarizability is negative for a wavelength of 1070 nm, it is positive for other wavelength accessible with commercially-available high-power lasers, such as a CO<sub>2</sub> laser at 10.8  $\mu\text{m}$ .

By using both dipole traps at once, through careful selection of the individual beam powers the upper-transition detuning can be canceled out, while maintaining a large effective 5S ground-state potential well depth. This would mean that atoms in the dipole trap would still be cooled by the trap's six-beam optical molasses.

### 6.2.3 Zeeman slower

The primary purpose of the low-field pyramidal MOT is simply to provide an incident flux of collimated atoms with an average velocity of 20 m/s, directed toward the central high-field chamber. The measured flux out of this setup is  $5 \times 10^8$  atoms/s. In contrast, a rubidium Zeeman slower is capable of producing a flux of  $\sim 10^{12}$  atoms/s, cooled to a longitudinal mean speed of  $\sim 45$  m/s [101]. Additional cooling could be provided to reduce the atom speed down to the desired 20 m/s with minimal atom loss. Such a Zeeman slower injection system would give an overall increase of up to three orders of magnitude over current system input flux. Since currently our trap is limited by loss mechanisms unrelated to the atom density (beam imperfections and background collisions, as detailed in Chap. III), until spin-changing cold atom collisions become an appreciable effect the number of trapped atoms should increase linearly with the incident flux of atoms. Atoms from the Zeeman slower, with their larger transverse kinetic energy ( $\sim 3$  mK compared to  $\sim 0.1$  mK from the PMOT source), will have a correspondingly lower recapture efficiency, but a total improvement in the number of trapped atoms by a factor of 100 is expected. This change would represent a substantial improvement to the high-field trap, and could be accomplished without altering any of the high-magnetic-field cryogenic or vacuum chamber components. Even a density increase by a factor of 10 would allow for Rydberg-Rydberg interaction studies and observation of spatial correlations.

## 6.3 Future studies

### 6.3.1 Blockade Statistics

Achieving higher densities would allow for observation of the dipole blockade within a high-magnetic-field system. This could be accomplished through excitation-counting statistics; by looking for a plateau in the number of excitations due to the presence of blockaded ‘bubble regions’ in the system. Within each bubble, the presence of a single Rydberg excitation causes energy shifts and inhibits the formation of a second Rydberg excitation. The number of Rydberg excitations is thus no longer limited by the atom density and the laser intensities, but rather by the number of bubbles that can be packed into the excitation region. Since this excitation volume is invariant, Rydberg excitations in a blockaded sample will follow a sub-Poissonian number distribution [102].

### 6.3.2 Spatial imaging

Additionally, the high-magnetic-field trap benefits from a strong magnification of the trapping or excitation region along the  $x$ -axis, transverse to the magnetic field direction. As the electrons travel from the trap location to the MCP (located in a region with a much lower magnetic field) they adiabatically follow the magnetic field lines. This preserves the transverse spatial information, while giving a strong magnification of the trap as the electrons are mapped onto the MCP phosphor screen. As previously demonstrated in a low-field blockade experiment [103], under appropriate conditions the blockade effect can be visually observed via analysis of the spatial correlations of count positions. Such a potential experiment in the high-magnetic-field system is outline in Fig. 6.4. At a field of 2.9 T, the high-magnetic-field trap system gives a magnification of 40.4 in the  $x$ -direction, and 1.7 in the  $y$ -direction. This re-

solving power can also be amplified by artificially lowering the magnetic field at the location of the MCP by applying a reverse bias field at that location, increasing the transverse magnification by an additional factor of two. This means that the MCP, with a spatial resolution of  $\geq 10$  lines/mm ( $100 \mu\text{m}$ ), gains a corresponding total increase of 80 in resolution along the  $x$ -axis. The resulting spatial resolution would be  $1.3 \mu\text{m}$ . By exciting a single sheet or line of atoms transverse to the magnetic field direction, with a higher density sample it would be possible to detect spatial correlations within a blockaded sample.

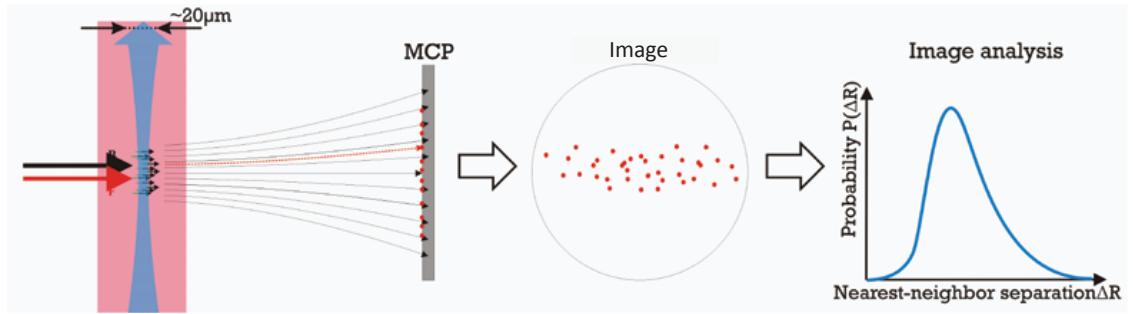


Figure 6.4: Possible Experiment investigating the presence of spatial correlation within a sample of excited Rydberg atoms. Atoms are excited to states with strong permanent dipole moments, creating blockading regions in which at most one excitation is observed. The resulting image on the MCP recovers this information with the strong magnification in the transverse direction.

### 6.3.3 Quadrupole Interactions

Further, Rydberg atoms in the high-magnetic-field trap also bear more exotic characteristics, such as permanent quadrupole moments. These quadrupole moments are formed at higher energies from the transverse constraint of the wavefunction. The higher the energy of the Rydberg atom, the larger is this diamagnetic effect. A quadrupole-quadrupole interaction would result in an energy shift in the same manner as the dipole-dipole interaction. It would, however, be distinguishable by its scaling: while the dipole-dipole interaction scales as  $N^4/r^3$ , the quadrupole-quadrupole interaction would bear a different scaling:

$$\Delta E_{qq} = \frac{1}{4\pi\epsilon_0} \left[ \frac{1}{2} \sum_{i,j} Q_{ij} \frac{x_i x_j}{r^5} \right] \quad (6.2)$$

$$Q_{ij} = \int (3x'_i x'_j - r' \delta_{ij}) \rho(\mathbf{x}') d^3 x' \quad (6.3)$$

For highly excited states, this would result in Rydberg-Rydberg interactions with a unique scaling dependence, proportional to  $N^8/r^5$  [104]. This resides between the scalings of dipole-dipole interactions ( $N^4/r^3$ ) and van der Waals interactions ( $N^{11}/r^6$ ). Another advantage of the quadrupole-quadrupole interaction in the high-field trap is that these quadrupoles are all aligned with the strong magnetic field. Exciting a string of atoms with a narrow transverse beam would give a series of Rydberg atoms with a well-defined alignment with respect to each other.

#### 6.3.4 Magnetic trapping

Magnetic-dipole interactions between pairs of diamagnetic Rydberg atoms are in the sub-Hz range and are negligible. However, the strength of the magnetic dipole moments determines the suitability for magnetic trapping of Rydberg atoms. Values in the range  $\lesssim -10 \mu_B$ , as encountered in the “X”-pair of levels presented in Chap. IV, are ideal for that purpose. Although Rydberg atom trapping has previously been accomplished using optical and electrostatic interactions, magnetic trapping of individual well-defined Rydberg states is still to be demonstrated. Diamagnetic Rydberg levels in the  $n$ -mixing regime are suitable for this purpose due to their combination of high optical excitation rates and large magnetic dipole moments.

#### 6.3.5 Plasma studies

Another capability of the high-magnetic-field trap is the ability to create plasmas. One longstanding goal of plasma physics has been to achieve and study plasmas

within the strong-coupling regime, where the Coulomb interaction energy is greater than the thermal energy of the plasma. The coupling strength is measured by the parameter  $\Gamma$ , which is the ratio of the Wigner-Seitz radius to the Coulomb distance of closest approach:

$$a_{\text{dca}} = \frac{e^2}{4\pi\epsilon_0} \frac{1}{k_B T} \quad (6.4)$$

When the coupling parameter significantly exceeds unity ( $\Gamma = a_{\text{dca}}/a_{\text{WS}} \gg 1$ ), the plasma is said to be in the strong-coupling regime.

Plasma formation in the high-magnetic-field trap occurs through photo-ionization of an atomic sample, resulting in charged electron and ion components. The high-magnetic field trap provides the additional benefit of being able to simultaneously trap both components in a nested Penning trap configuration. The four-component electrode package is used to provide a confining potential in the longitudinal direction for both an inner region of positively-charged ions, and an outer region of faster-moving electrons. Transverse confinement is provided by the large magnetic field, which induces a magnetron motion for the charged particles. The high-magnetic-field trap has been used to successfully trap and study the dynamics of two-component plasmas [39]. Previous efforts [95] with this trap have also shown indications of short-range order within the electron cloud.

An extension of this work would be to improve and increase the electron and ion densities. For the current trap density of  $10^9$  atoms/cm<sup>3</sup>, a plasma temperature of  $\sim 3$  K or less would reach the regime of strong coupling. However, electron temperatures of 250 K are observed [39]. This temperature stems from exciting and ionizing atoms throughout the trapping volume, which results in a high initial electron potential energy and quickly heats up the electrons as they equilibrate within the well.

Several possible improvements could be made to the current experiment. Any density increase, as detailed above, would serve to increase the coupling parameter. Effort can also be made to decrease the kinetic energies involved: by using a crossed-beam geometry, only the electrons at the center or bottom of the well would be excited, leading to lower plasma temperatures. A more drastic change would involve modifying the inner chamber to allow for a rotating-wall cooling technique in order to achieve colder temperatures.

### 6.3.6 Three-body recombination

Another area of significant research interest is three-body recombination. Three-body recombination occurs via the simultaneous collision of two electrons and an ion, and results in a high-energy electron and a bound electron-ion pair (a Rydberg atom). Three-body recombination is used as the formation mechanism in the anti-hydrogen production experiments [105, 106] at CERN. Although this process has been extensively studied in low-field plasmas [107, 108], extensions to high-magnetic-field conditions have only been calculated [76, 109]. The high-field trap represents a unique opportunity for conducting low-temperature three-body recombination studies. Extraction of the density and temperature scalings would further our understanding of the anti-hydrogen formation process, and possibly serve to increase yields in such experiments.

Currently, such experiments are once again limited by the lower trap density, and the creation of initial Rydberg atoms during the ionization process. Although the pulsed upper-transition  $\sim 480$  nm laser has a bandwidth of  $\approx 10$  GHz (giving an electron temperature range of  $T_e \approx 1$  mK), the presence of a large low-power spectral background extending several nm creates unwanted Rydberg atoms. One possible avenue would be to seed the dye laser with a narrow-band cw pulse instead of using

a pulsed ND:YAG as in the current setup. This would result in bandwidth-limited pulses with powers on the order of 3 W for a continuous beam.

Alternatively, another approach would be to use a microwave-ionization technique to clear the sample of any initial Rydberg atoms before waiting for the formation of further Rydberg atoms. Currently, because of the large cryogenic chamber size and small ( $\sim 1$  cm) access ports it is not possible to inject the microwaves into the vacuum cavity from an external horn with enough power to efficiently ionize the Rydberg atoms. A next-generation apparatus would have an internal microwave horn, allowing direct application of the microwave power to the trapped sample.

### 6.3.7 Quantum excitation transport

An additional application of Rydberg excitation within the high-magnetic field trap is the investigation of quantum state diffusion. It is possible to populate two different Rydberg states of the same  $m_J$  and  $\Pi_z$  character, by using two narrow linewidth cw 480 nm lasers. The spatial extents of these populations can be controlled independently via separate optical alignment. An experimental realization of such a double-excitation is shown in Fig. 6.5. The two states can also be experimentally distinguished by applying a field ionization pulse such that only the most energetic one is ionized and subsequently detected.

Since cold Rydberg atoms in the trap move at low speeds of  $\sim 0.1$  m/s, over the course of a few  $\mu$ s the motion is  $< 1$   $\mu$ m, giving a ‘frozen Rydberg gas’. In this gas, the two excited states cannot diffuse through Brownian motion. However, the quantum character of the excitations will migrate, or ‘hop’, throughout the Rydberg excitations [110–112]. An analysis of how the excitations of different character diffuse throughout the sample over such short time frames would give insight into dynamics of quantum state diffusion.



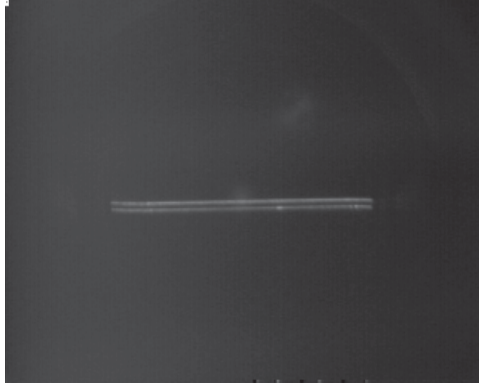


Figure 6.5: Sample averaged image of simultaneous excitation of two different Rydberg states. Two independently-controlled narrow-linewidth cw 480 nm lasers are focused into the trap with FWHM  $\sim 20 \mu\text{m}$ , transverse to the magnetic field axis, to excite a string of Rydberg atoms.

## 6.4 Conclusion

The high-magnetic-field trap is a novel apparatus that allows for precision spectroscopy in fields of up to 3 T. Previously, experiments within such fields were confined to atomic beams, and precision studies were limited by the resulting Lorentz broadening. The high-magnetic-field trap opens up new avenues of study, such as the discussed Rydberg atom interaction experiments. Additionally, the ability to create and study two-component ultracold plasmas opens up new avenues of study such as three-body recombination processes. The high-magnetic-field trapping experiment is a veritable workhorse, and further improvements to the apparatus will increase its effectiveness in the years to come.



## APPENDICES

## APPENDIX A

### Derivation of the magnetic-field Hamiltonian

With the magnetic field pointing along the  $z$ -direction, we may use the symmetric gauge by choosing the vector potential such that

$$\vec{A}(\vec{r}) = -\frac{1}{2}(\vec{r} \times \vec{B}) = -\frac{1}{2}(yB_z\hat{x} - xB_z\hat{y}) \quad (\text{A.1})$$

This satisfies the (Coulomb gauge) condition  $\vec{\nabla} \cdot \vec{A} = \frac{-1}{2}\left(\frac{\partial(yB_z)}{\partial x} + \frac{\partial(-xB_z)}{\partial y}\right) = 0$

We can use the Dirac equation to describe a particle within a static potential:

$$\begin{aligned} \hat{\sigma} \cdot \left(\hat{p} + \frac{e}{c}\vec{A}\right)\psi_B &= \frac{1}{c}[E - m_0c^2 - V(\vec{r})]\psi_A \\ \hat{\sigma} \cdot \left(\hat{p} + \frac{e}{c}\vec{A}\right)\psi_A &= \frac{1}{c}[E + m_0c^2 - V(\vec{r})]\psi_B \end{aligned}$$

Here,  $\psi_A$  and  $\psi_B$  are two-component spinors. Approximating the equation A.2 as:

$$\begin{aligned} \hat{\sigma} \cdot \left(\hat{p} + \frac{e}{c}\vec{A}\right)\psi_A &\simeq \frac{1}{c}[2m_0c^2]\psi_B = [2m_0c]\psi_B \\ \psi_B &\simeq \frac{1}{2m_0c}\hat{\sigma} \cdot \left(\hat{p} + \frac{e}{c}\vec{A}\right)\psi_A \end{aligned}$$

We can then substitute this into equation A.1, and write  $\varepsilon = E - m_0c^2$ , to arrive at:

$$\frac{1}{2m_0}[\hat{\sigma} \cdot \left(\hat{p} + \frac{e}{c}\vec{A}\right)][\hat{\sigma} \cdot \left(\hat{p} + \frac{e}{c}\vec{A}\right)]\psi_A = (\varepsilon - V(\vec{r}))\psi_A$$

The Hamiltonian for the problem is thus:

$$\hat{H} = \frac{1}{2m_0} [\hat{\sigma} \cdot (\hat{p} + \frac{e}{c} \vec{A})] [\hat{\sigma} \cdot (\hat{p} + \frac{e}{c} \vec{A})] - e\Phi - \frac{e^2}{\hat{r}} \quad (\text{A.2})$$

We can expand the left-hand side of this equation. Looking at this more closely, we arrive at:

$$\begin{aligned} & [\hat{\sigma} \cdot (\hat{p} + \frac{e}{c} \vec{A})] [\hat{\sigma} \cdot (\hat{p} + \frac{e}{c} \vec{A})] \\ &= (\hat{\sigma} \cdot (\vec{C})) (\hat{\sigma} \cdot (\vec{C})) \\ &= \hat{\sigma}_x^2 C_x^2 + \hat{\sigma}_y^2 C_y^2 + \hat{\sigma}_z^2 C_z^2 \\ &\quad + \hat{\sigma}_x \hat{\sigma}_y C_x C_y + \hat{\sigma}_y \hat{\sigma}_z C_y C_z + \hat{\sigma}_z \hat{\sigma}_x C_z C_x \\ &\quad + \hat{\sigma}_y \hat{\sigma}_x C_y C_x + \hat{\sigma}_z \hat{\sigma}_y C_z C_y + \hat{\sigma}_x \hat{\sigma}_z C_x C_z \\ &= \vec{C}^2 + i\hat{\sigma}_z (C_x C_y - C_y C_x) \\ &\quad + i\hat{\sigma}_x (C_y C_z - C_z C_y) \\ &\quad + i\hat{\sigma}_y (C_z C_x - C_x C_z) \\ &= \vec{C}^2 \\ &\quad + i\hat{\sigma}_z [p_x p_y - p_y p_x + (\frac{e}{c})^2 (A_x A_y - A_y A_x) + \frac{e}{c} (A_x p_y + p_x A_y - p_y A_x - A_y p_x)] \\ &\quad + i\hat{\sigma}_x [p_y p_z - p_z p_y + (\frac{e}{c})^2 (A_y A_z - A_z A_y) + \frac{e}{c} (A_y p_z + p_y A_z - p_z A_y - A_z p_y)] \\ &\quad + i\hat{\sigma}_y [p_z p_x - p_x p_z + (\frac{e}{c})^2 (A_z A_x - A_x A_z) + \frac{e}{c} (A_z p_x + p_z A_x - p_x A_z - A_x p_z)] \\ &= \vec{C}^2 + i\hat{\sigma}_z (\frac{e}{c}) (A_x p_y - A_y p_x) + i\hat{\sigma}_z (\frac{e}{c}) (p_x A_y - p_y A_x) \\ &\quad + i\hat{\sigma}_x (\frac{e}{c}) (A_y p_z - A_z p_y) + i\hat{\sigma}_x (\frac{e}{c}) (p_y A_z - p_z A_y) \\ &\quad + i\hat{\sigma}_y (\frac{e}{c}) (A_z p_x - A_x p_z) + i\hat{\sigma}_y (\frac{e}{c}) (p_z A_x - p_x A_z) \\ &= (\hat{p} + \frac{e}{c} \vec{A})^2 + (\frac{e}{c}) [i\hat{\sigma} \cdot (\vec{A} \times \hat{p}) + i\hat{\sigma} \cdot (\hat{p} \times \vec{A})] \\ &= (\hat{p} + \frac{e}{c} \vec{A})^2 + (\frac{e}{c}) i\hat{\sigma} \cdot [(\vec{A} \times \hat{p}) + (\hat{p} \times \vec{A})] \end{aligned}$$

We can simplify the latter part of this equation by using the product rule:

$$\begin{aligned}\vec{\nabla} \times (\vec{A}\psi) &= (\vec{\nabla} \times \vec{A})\psi - \vec{A} \times \vec{\nabla}\psi \\ &= \frac{\hbar}{i} \frac{i}{\hbar} [(\vec{\nabla} \times \vec{A})\psi - \vec{A} \times \vec{\nabla}\psi] \\ &= \frac{i}{\hbar} [(\hat{p} \times \vec{A})\psi - \vec{A} \times \hat{p}\psi]\end{aligned}$$

This gives:

$$\begin{aligned}\vec{A} \times \hat{p}\psi + \hat{p} \times \vec{A}\psi &= \frac{i}{\hbar} (\vec{\nabla} \times \vec{A})\psi \\ &= \frac{\hbar}{i} \vec{B}\psi\end{aligned}$$

The Hamiltonian is now:

$$\hat{H} = \frac{1}{2m_0} \left[ \left( \hat{p} + \frac{e}{c} \vec{A} \right)^2 + \frac{e}{c} (i\hat{\sigma} \cdot \left( \frac{\hbar}{i} \vec{B} \right)) \right] - e\Phi - \frac{e^2}{r} \quad (\text{A.3})$$

The first part of the above equation can also be expanded:

$$\left( \hat{p} + \frac{e}{c} \vec{A} \right)^2 = \hat{p}^2 + \frac{e}{c} (\hat{p} \cdot \vec{A} + \vec{A} \cdot \hat{p}) + \left( \frac{e}{c} \right)^2 \vec{A}^2$$

We note that:

$$\vec{A}^2 = \left[ \frac{1}{2} (\vec{r} \times \vec{B}) \right]^2 = \frac{1}{4} [r^2 B^2 - (\vec{B} \cdot \vec{r})(\vec{r} \cdot \vec{B})] = \frac{1}{4} (r^2 B^2 - z^2 B^2) = \frac{1}{4} \rho^2 B^2$$

Also:

$$\vec{\nabla} \cdot (\vec{A}\psi) = \vec{A} \cdot \vec{\nabla}\psi + (\vec{\nabla} \cdot \vec{A})\psi = \vec{A} \cdot \vec{\nabla}\psi$$

$$\begin{aligned}
(\hat{p}\vec{A} + \vec{A}\hat{p}) &= \frac{\hbar}{i}\vec{\nabla} \cdot \vec{A} + \frac{\hbar}{i}\vec{A} \cdot \vec{\nabla} \\
&= \frac{2\hbar}{i}\left[\frac{-1}{2}(\vec{r} \times \vec{B}) \cdot \vec{\nabla}\right] \\
&= \frac{\hbar}{i}[(\vec{B} \times \vec{r}) \cdot \vec{\nabla}] \\
&= \frac{\hbar}{i}[\vec{B} \cdot (\vec{r} \times \vec{\nabla})] \\
&= \vec{B} \cdot (-i\hbar\vec{r} \times \vec{\nabla}) \\
&= \vec{B} \cdot \vec{L} \\
&= B_z L_z
\end{aligned}$$

We can now reconstruct the Hamiltonian:

$$\begin{aligned}
\hat{H} &= \frac{1}{2m_0}\left[\left(\hat{p} + \frac{e}{c}\vec{A}\right)^2 + \frac{e}{c}(i\hat{\sigma} \cdot \left(\frac{\hbar}{i}\vec{B}\right))\right] - e\Phi - \frac{e^2}{\hat{r}} \\
\hat{H} &= \frac{1}{2m_0}\left(\hat{p} + \frac{e}{c}\vec{A}\right)^2 + \frac{1}{2m_0}(i\hat{\sigma} \cdot \left(\frac{\hbar}{i}\vec{B}\right)) - e\Phi - \frac{e^2}{\hat{r}} \\
\hat{H} &= \frac{1}{2m_0}\hat{p}^2 + \frac{e}{2m_0c}[B_z L_z] + \frac{1}{2m_0}\left(\frac{e}{c}\right)^2\left[\frac{1}{4}\rho^2 B^2\right] + \frac{1}{2m_0}\left(\frac{e}{c}\right)[2\vec{S} \cdot \vec{B}] - e\Phi - \frac{e^2}{\hat{r}} \\
\hat{H} &= \frac{\hat{p}^2}{2m_0} + \frac{e}{2m_0c}[L_z + 2S_z]B_z + \frac{e^2}{m_0c^2}\left[\frac{1}{8}\rho^2 B^2\right] - e\Phi - \frac{e^2}{\hat{r}}
\end{aligned}$$

Noting that  $\Phi = -\hat{z}F_z$ , we can finally write our Hamiltonian as:

$$\hat{H} = \frac{\hat{p}^2}{2m_0} - \frac{e^2}{r} + \frac{1}{2m_0c}[L_z + 2S_z]B_z + \frac{e^2}{m_0c^2}\left[\frac{1}{8}\rho^2 B^2\right] + e\hat{z}F_z \quad (\text{A.4})$$

Or, in atomic units:

$$\hat{H} = \frac{\hat{p}^2}{2} - \frac{1}{\hat{r}} + \frac{B_z}{2}[L_z + 2S_z] + \frac{1}{8}\rho^2 B^2 + \hat{z}F_z \quad (\text{A.5})$$

$$(\text{A.6})$$

## APPENDIX B

### Rubidium hyperfine structure

The isotope rubidium 85 has a nuclear angular momentum quantum number of  $I = 5/2$ . The ground state of  $^{85}\text{Rb}$  is  $5\text{S}_{1/2}$ , with  $J = 1/2$ . In a low magnetic field regime, this gives two levels with a total atom angular momentum quantum number  $\mathbf{F} = \mathbf{I} + \mathbf{J} \rightarrow \{2, 3\}$ . The level splitting can be described in terms of the  $F$  quantum number and the sub-levels  $m_F$ :

$$\Delta E(F, m_F) = \mu_B g_F m_F B_0 \quad (\text{B.1})$$

As the magnetic field is increased from zero, the  $I$  and  $J$  become increasingly decoupled. Once they are completely decoupled, the good or diagonal basis is now  $|I, m_I\rangle|J, m_J\rangle$ . States are then organized into groups of the same  $m_J$ , that each carry the same dependence on  $B_0$ . Within each such group, there are  $(2I + 1)$  states of even separation:

$$\Delta W_{m_I, m_J} = \mu_B g_J m_J B_0 + A_{n\ell} m_I m_J. \quad (\text{B.2})$$

To calculate the  $5\text{S}_{1/2}$  ground states as a function of magnetic field, we can use the Breit-Rabi formula [113]:

$$\Delta E(F = I \pm 1/2, m_F) = -\frac{E_{hfs}}{2(2I + 1)} \pm \frac{1}{2} \sqrt{E_{hfs} + \frac{4m_F}{2I + 1} g_J \mu_B B E_{hfs} + (g_J \mu_B B)^2} \quad (\text{B.3})$$

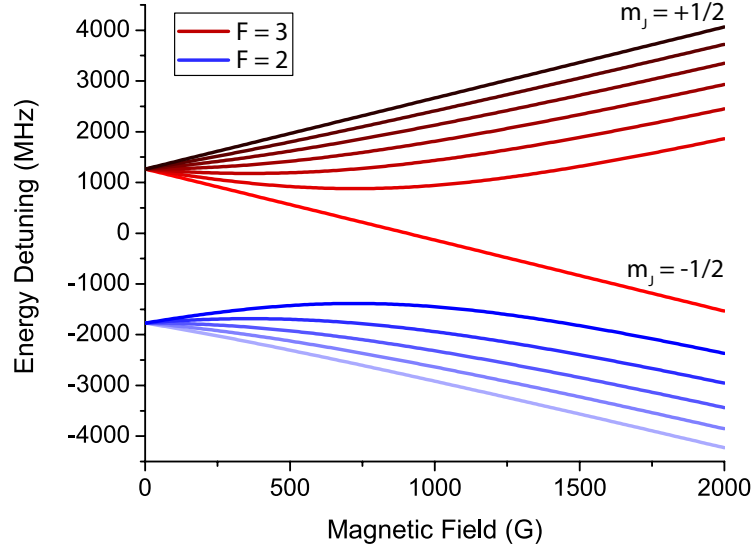


Figure B.1:  $^{85}\text{Rb}$  hyperfine structure of the  $5\text{P}_{3/2}$  state within a magnetic field. In low-field conditions  $|F, m_F\rangle$  is a good basis, as indicated by the color groupings. As the magnetic field increases, the states pass through an intermediate region, until finally the  $I$  and  $J$  quantum numbers become decoupled, and the states are organized in groups of the same  $m_J$ .

Here,  $E_{hfs}$  is the splitting at zero magnetic field ( $E_{hfs}(^{85}\text{Rb}) = 3.036$  GHz,  $E_{hfs}(^{87}\text{Rb}) = 6.834$  GHz),  $g_J = 2$  is the electron total angular momentum g-factor, and  $\mu_B$  is the Bohr magneton. Figures B.1 and B.3 show this structure for the two most common isotopes of rubidium.

For more general cases, the problem can be solved by diagonalizing the magnetic-field perturbation component of the Hamiltonian:

$$H' = Ah\mathbf{I} \cdot \mathbf{J} + g_J \mu_B \mathbf{J} \cdot \mathbf{B}_0 - g_I \mu_B \mathbf{I} \cdot \mathbf{B}_0 \quad (\text{B.4})$$

Here  $A$  is the hyperfine structure constant [114, 115], which varies for each state:



Isotope	Constant	MHz
$^{85}\text{Rb}$	$A_{5S_{1/2}}$	1011.91
	$A_{5P_{3/2}}$	25.002
$^{87}\text{Rb}$	$A_{5S_{1/2}}$	3417.341
	$A_{5P_{3/2}}$	84.718

Table B.1: Hyperfine structure constant for the ground and first excited states of  $^{85}\text{Rb}$  and  $^{87}\text{Rb}$ .

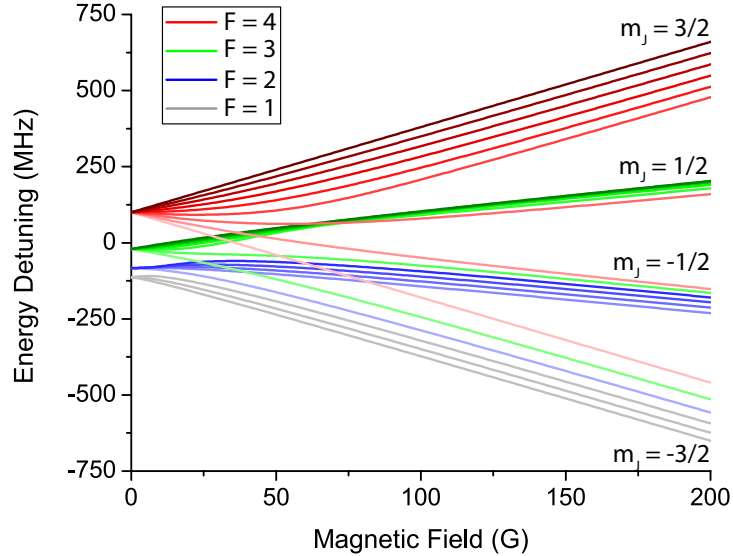


Figure B.2:  $^{85}\text{Rb}$  hyperfine structure of the  $5P_{1/2}$  state versus magnetic field. Under low-field conditions the states are organized into groups with  $\mathbf{F} = \{1, 2, 3, 4\}$ . In a large magnetic field, we have groups of the same  $m_J$  ( $-3/2$  to  $3/2$ ), each with the same slope. Within each individual  $m_J$  set there are 6 states, one for each of the possible  $m_I$  values:  $m_I = \{-5/2, -3/2, -1/2, 1/2, 3/2, 5/2\}$ .

Figures B.2 and B.4 show this hyperfine structure of the  $5P_{3/2}$  states for  $^{85}\text{Rb}$  and  $^{87}\text{Rb}$ . Again, at low field values of  $B_0$  states are divided into groups of the same total angular momentum  $F$ , as indicated by the colors. As the field is gradually increased, the  $m_J$  character of each sub-level (roughly represented by the shading) has a larger effect. Finally, for large values of  $B_0$ , the states are again divided into groups of the same  $m_J$ . Each such group contain  $(2I + 1)$  states.

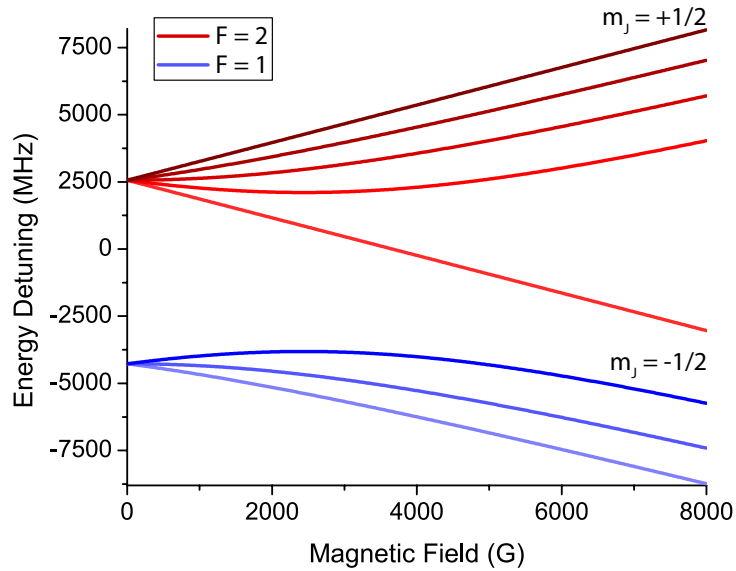


Figure B.3:  $^{87}\text{Rb}$  hyperfine structure of the  $5S_{1/2}$  ground state versus magnetic field. This can be calculated using the Breit-Rabi formula.

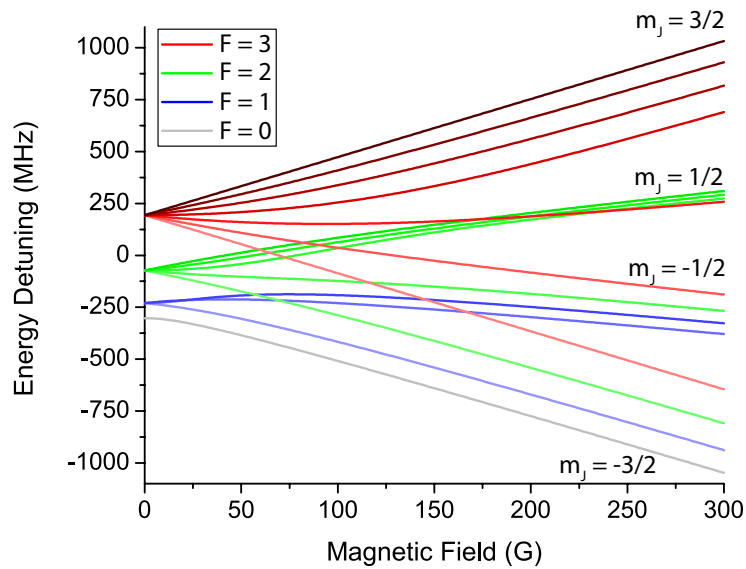


Figure B.4:  $^{87}\text{Rb}$  hyperfine structure of the  $5P_{1/2}$  state versus magnetic field. Under low-field conditions the states are organized into groups with  $\mathbf{F} = \{0, 1, 2, 3\}$ . In a large magnetic field, we have groups of the same  $m_J$  ( $-3/2$  to  $3/2$ ), each with the same slope. In each individual  $m_J$  set there are 4 states, one for each of the possible  $m_I$  values:  $m_I = \{-3/2, -1/2, 1/2, 3/2\}$ .

## APPENDIX C

### Electron motion in a Penning trap

A free electron within static electric and magnetic fields can be described by the following equation:

$$\frac{d\mathbf{v}}{dt} = \frac{q}{m_e}(\mathbf{F}_{\text{el}} + \mathbf{v} \times \mathbf{B}) \quad (\text{C.1})$$

For a strong magnetic field along the  $z$ -axis, we can separate the velocity vector and the electric field into components parallel and perpendicular to the magnetic field:

$$\frac{dv_{\parallel}}{dt} + \frac{dv_{\perp}}{dt} = \frac{q}{m_e}(F_{\parallel} + F_{\perp} + v_{\perp}B)$$

We can then separate this into two equations:

$$\begin{aligned} \frac{dv_{\parallel}}{dt} &= \frac{q}{m_e}F_{\parallel} \\ \frac{dv_{\perp}}{dt} &= \frac{q}{m_e}(F_{\perp} + v_{\perp}B) \end{aligned} \quad (\text{C.2})$$

Equation C.2, or the motion parallel to the magnetic field axis, corresponds to the  $z$ -bounce motion. If the electric field strength corresponds to a harmonic potential with  $F_{\parallel} = -\alpha z$ , then we can calculate the frequency of oscillation:

$$\begin{aligned}
m \frac{dv_{\parallel}}{dt} &= m\ddot{z} = -q\alpha z \\
\omega &= \sqrt{\frac{k}{m}} = \sqrt{\frac{q\alpha}{m}}
\end{aligned} \tag{C.3}$$

Here,  $\alpha$  is a parameter describing the curvature or ‘steepness’ of the harmonic well. In the case of the high-magnetic-field trap, the four-component electrode package can be set up such that the electrons, created at the center between the four longitudinal electrodes, will see a roughly harmonic potential. We can then estimate the approximate oscillation frequency along the axial direction of the trap. For an electric potential configuration of -50 V/-50 V/0 V/-50 V (such that the electrons are trapped within a well between electrodes two and four), we arrive at  $\alpha \simeq 2.2 \times 10^5 \text{ V/m}^2$ . This gives an oscillation frequency of:

$$\omega = \sqrt{\frac{q\alpha}{m}} = 20 \times 10^8 \text{ s}^{-1}$$

This gives an oscillation period of 30 ns. Although we do have the time resolution to observe such a signal, the confining potentials can only be changed on a much longer timescale ( $\sim 1 \mu\text{s}$ ). Detection of the  $z$ -bounce signal will only be possible with faster electronics.

Returning to our system of equations, we can now look at the motion in the plane perpendicular to the magnetic field direction:

$$\begin{aligned}
\frac{dv_{\perp}}{dt} &= \frac{q}{m_e}(F_{\perp} + v_{\perp}B) \\
\frac{d(v_D + v')}{dt} + &= \frac{q}{m_e}(F_{\perp} + (v_D + v')B)
\end{aligned}$$

Were we describing a free particle in a magnetic field, the electric field would go to zero, and the motion would be characterized by the cyclotron frequency:

$$\begin{aligned}\frac{dv_{\perp}}{dt} &= \frac{q}{m_e} v_{\perp} B \\ \frac{v_{\perp}^2}{r} &= \frac{qB}{m_e} v_{\perp} \\ \omega_c &= \frac{v_{\perp}}{r} = \frac{qB}{m_e}\end{aligned}\tag{C.4}$$

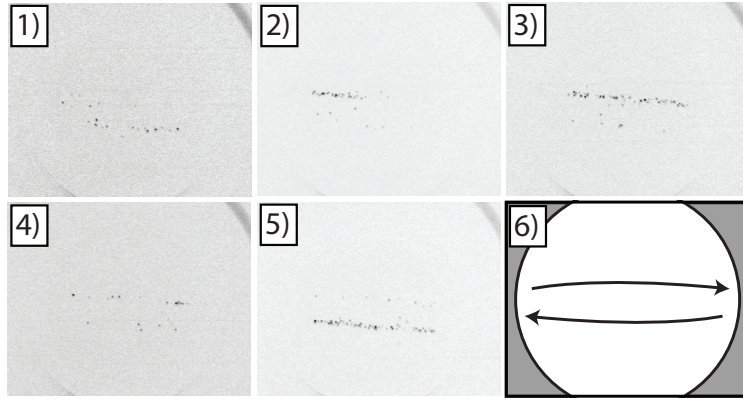


Figure C.1: 1)  $\rightarrow$  5): Pictures of electron signal impinging upon the MCP detector, for subsequent steps of the delay time. 6) Diagram showing the (mirror-image) motion of the electrons within the Penning trap. The horizontal axis motion is exaggerated due to our image system, giving an aspect ratio of 20 : 1.

For an electron in a 2.6 T field, the cyclotron frequency is  $\omega_c = 4.5 \times 10^{11} \text{ s}^{-1}$ , corresponding to a period of 13.7 ps. This is much too fast to be experimentally observed, as free electrons in the trap travel in tight small circles on the nanometer scale. In the equations above, the fast-moving cyclotron component will be changing much faster than the slower drift velocity ( $\frac{dv_D}{dt} \ll \frac{dv'}{dt}$ ). In this case we can separate the equation, to arrive at:

$$\begin{aligned}\frac{dv'}{dt} &= \left(\frac{qB}{m_e}\right)v_{\perp} \\ 0 &= \frac{q}{m_e}(F_{\perp} + v_D B)\end{aligned}$$

We recognize  $v'$  as the cyclotron frequency. For the second equation, since the electric field has been described by a harmonic potentials, we note that  $F_{\perp} = +(\alpha/2)\rho$ . Solving for  $v_D$ , we see that:

$$\begin{aligned} v_D &= \frac{F_{\perp}}{B} = \frac{\alpha\rho}{2B} \\ \omega_D &= \frac{\alpha}{2B} \end{aligned} \tag{C.5}$$

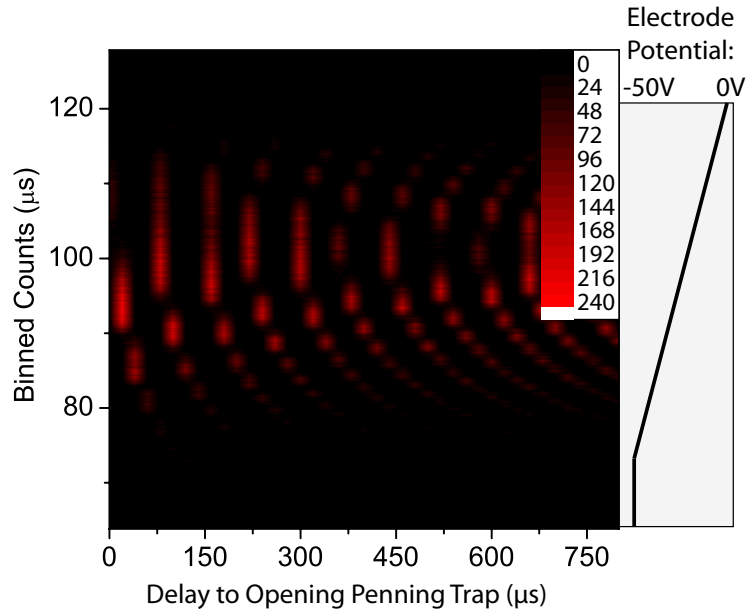


Figure C.2: Two-dimensional plot of time-resolved signal from the Penning Trap versus hold time within the trap (i.e. delay time before ejection). Each vertical cut corresponds to an averaged signal of several shots for a fixed delay time. The delay time is then varied from 0 to  $\sim 750 \mu\text{s}$ .

Using the same harmonic well and a field of 2.6 T, we arrive at a slow drift frequency of  $\omega_D = 4.2 \times 10^4 \text{ s}^{-1}$ , corresponding to an oscillation period of  $150 \mu\text{s}$ . This is the slower magnetron motion, as electron orbit along a larger radius about the central electric field saddle point. The interesting point about this last motion is that it is easily experimentally observable: ionizing an atom trap located slightly off-center from the saddle point causes a circular drift motion. When MCAP potential is suddenly raised the electrons are directed toward the MCP in a much faster timescale

( $t \sim 10 - 100$  ns) than the magnetron motion, so that information is preserved.

Because the MCP does not detect counts from the entire trapping region, the repeating this experiment results in a signal that appears and disappears off of the phosphor screen. This is shown in Fig. C.1. However, because the motion is periodic, we can detect the signal oscillation and extract a measured magnetron motion. Figure. C.2 and C.3 show Doing so results in a magnetron period of  $2 \times 72 = 144 \mu\text{s}$ , quite close to our calculated value.

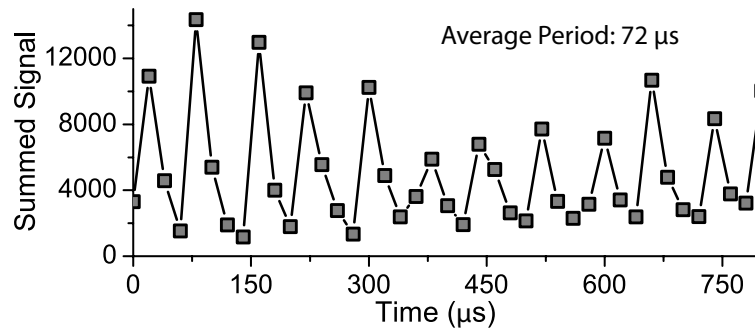


Figure C.3: Summed signal, for each set delay time, from the data in Fig. C.2. The signal decreases as the ‘group’ of electrons disappears from the field of view, then peaks again when it re-appears. The peak spacing represents half of the magnetron oscillation period.

## APPENDIX D

## Optical injection into the high-field trap

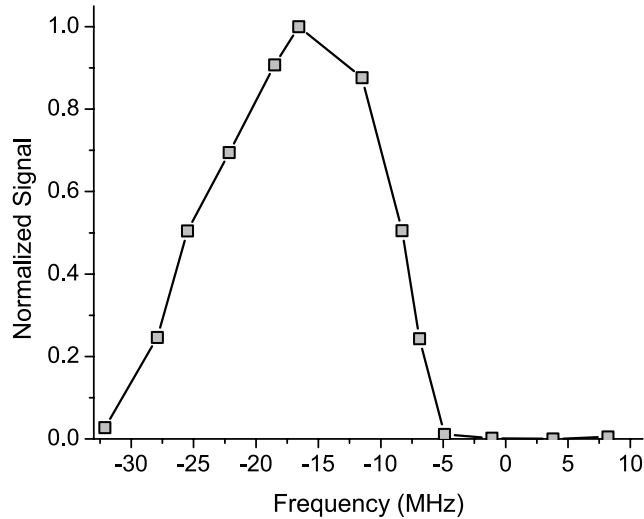


Figure D.1: Pyramidal trap performance versus applied  $5S_{1/2} \rightarrow 5P_{3/2}$  molasses frequency, as monitored via the trap fluorescence signal. During normal operation, this laser frequency is locked to optimize the trap performance, at  $\sim -15$  MHz.

Optical injection into the high-magnetic-field trap occurs via radiation pressure imbalance, as a small hole at the apex of the pyramidal MOT allows the atoms to leak out along that direction when the trapped atoms are aligned with it. However, as shown in Fig. D.1, this primary atom trap is optimized when the trapping frequency is about two linewidths red-tuned from the trapping resonance. This results in a greater number of atoms within the primary trap. However, because of this red-detuning output stream of atoms only has a mean speed of  $\sim 10$  m/s. This means that the



large majority of the atoms would have insufficient kinetic energy to overcome the large magnetic potential (18 m/s needed for a 2.6 T field) and reach the center of the high-field trapping region.

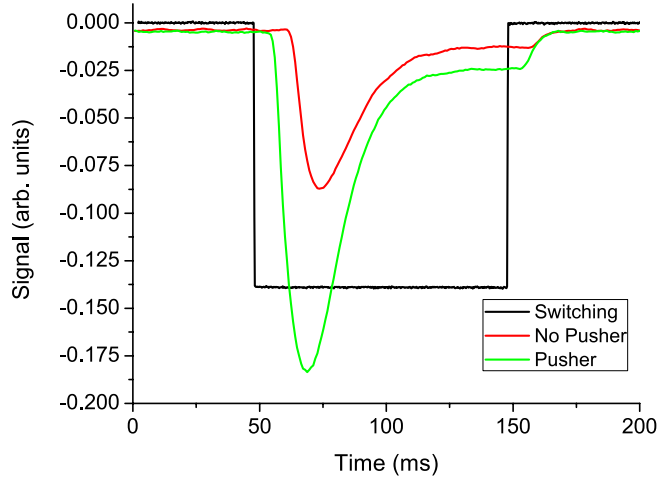


Figure D.2: Sample time-resolved data of the atom flux being suddenly turned on/off via magnetic field coil switching. With the pusher beam on and aligned, the atomic beam density increases.

In order to overcome this difficulty, we use a second small collimated beam of several  $I_{\text{SAT}}$  on the scale of the pinhole (beam intensity FWHM = 0.7 mm). We align this ‘pusher’ beam such that it overlaps both the atom trap, and the center of the high-field trap located 68 cm downstream. Atoms gain kinetic energy through radiation pressure imbalance, and are directed into the high-field region. We can profile the change in flux by performing an absorption measurement: we pass a low-intensity probe beam perpendicularly through the atom flux 15 cm downstream from the pyramidal MOT. The change in absorption for an unsaturated probe beam relates to the atomic flux. As shown in Fig. D.2, we also performed a timed experiment by rapidly switching a magnetic field coil at the trap location, effectively turning the trap on and off. The pusher beam has a strong effect, resulting in both more probe absorption (through a higher atomic density in the beam) and an increased mean

atomic speed.

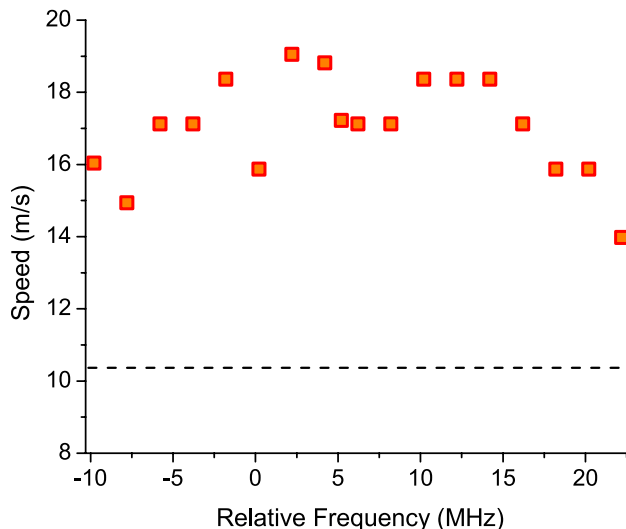


Figure D.3: Mean speed versus pusher beam frequency. For the optical beam density values (at a frequency offset of +10.5 MHz), the speed is measured to be  $\sim 18$  m/s (with a root-mean-square spread of  $\sigma \sim 5$  m/s), compared to 10 m/s in the absence of the pusher beam (dashed line).

In Figure D.3, we investigate the relation between the frequency and of the applied pusher beam and the resulting the mean speed of atomic beam. We find a weak correlation between the two (the dominant effect is rather due to the strong intensity imbalance within the MOT). The absorption, on the other hand, was strongly dependent on the pusher beam frequency, with a maximal measured density at a relative frequency of +10.5 MHz from the MOT cooling frequency. Since the MOT beams are  $\sim 2\Gamma$  red-detuned, this corresponds to a beam that is resonant with the 5S-5P optical transition.

From the absorption measurements, we can then calculate the atomic flux. We find a peak measured flux of  $5 \times 10^8$  s $^{-1}$  (over a full divergence angle of 50 mrad) at a relative detuning of +10.5 MHz. As shown in Fig. D.4, this gives a net flux increase of  $\sim 7$  as compared to the case with no pusher beam present.

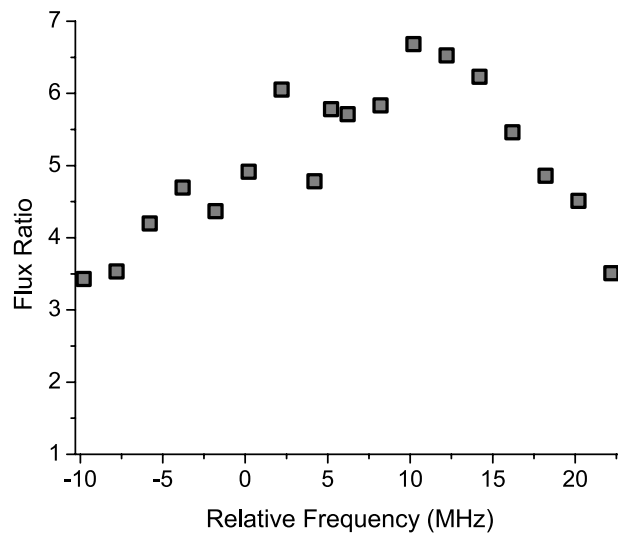


Figure D.4: Calculated ratio of the atomic beam flux versus pusher beam frequency, as compared to the case of no pusher beam.

## APPENDIX E

### High-B: a How-to Guide

#### E.1 Introduction

This appendix provides a practical overview on how to manage the high-magnetic field trapping apparatus throughout a data run, ranging from pre-run preparation to optimizing the trapped atoms number and trap lifetime. Although this is mostly presented in chronological order, it would be best to read the guide completely through before starting a data run.

#### E.2 Coils

The primary component of the high-B trap is the set of superconducting coils. In order to run the coils, we first need to order liquid helium from Linde. The inner jacket can be filled with approximately 60 liters of helium at a time, and has an evaporation rate of 1.5 L/hour. This is shown in Fig. E.1 There are two input ports on the top of the chamber, as well as an exhaust port. About  $\sim 160$  liters is standard for a  $\sim 3$  day run, although more can be ordered. Helium comes in 40, 60, 100 and 200 liter dewars. Standard delivery days are monday nights/tuesday mornings (as of 2012), and thursday night/friday morning. The exact time of delivery is not really determined, as the truck makes rounds throughout Ohio and Michigan, and the exact

route depends on which universities have placed helium orders. Cost is subject to change, of course, but is roughly  $\sim 400$  \$ for a 60 L dewar, and 650 \$ for a 100 L dewar. The order needs to be placed through physics requisition two business days in advance.

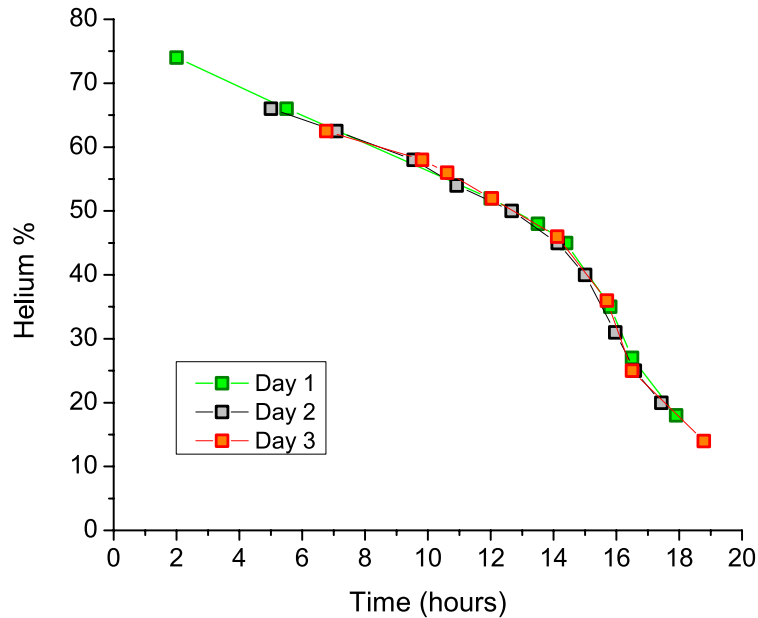


Figure E.1: Helium loss rate from the inner dewar during operation. The  $y$  axis here, in percent, refers to the fill height of the dewar, which is equal to 60 L when completely full. The non-linear part at around 40 % occurs because the magnet occupies a certain volume within the dewar.

Before the chamber is filled with liquid helium, it needs to be pre-cooled with liquid nitrogen. This can be done a couple days beforehand. Physics supplies the liquid nitrogen, and we regularly fill up our large lab dewar at the loading dock. To pre-cool the chamber, we need to fill both inner and outer jackets, which will take about a full dewar's worth of nitrogen ( $\sim 200$  lbs). The order of fill is not important. The outer jacket has three 'spouts', any of which can be used to fill. Place the fill tube in, and make sure the other spouts are not covered to allow outgassing. It will take about an hour or more to fill the outer jacket. Toward the end, pay close attention to the other spouts: nitrogen droplets will start to spray upward when it

is full. Try to minimize this; the droplets can damage the mirrors on the chamber. For the inner chamber, use the fill port closest to the east wall, which leads down all the way to the base of the inner chamber. Figure E.2 shows the location of the ports and release valves. When filling, also be sure to remove the pressure release valve on the front of the chamber. There are two resistors inside the chamber which can be used to acquire a level reading: 300 K is about 1 k $\Omega$ , 78 K is 1.5 k $\Omega$ , and 4 K is 37 k $\Omega$ . Also, 1.7 K (63 K) is nitrogen freezing temperature...this will be important later. Fill the chamber until the ‘top of magnet’ resistor reads a steady value of 1.5 k $\Omega$ . You only need to cover the magnet and a little bit more, there is no need to completely fill the inner chamber with 60 L of nitrogen. The value will drop when you stop pouring nitrogen in if the level is not above the top of the magnet. Once the inner chamber is filled, stopper up the fill port and close off the pressure release valve again to avoid any water from entering into the inner jacket and freezing.

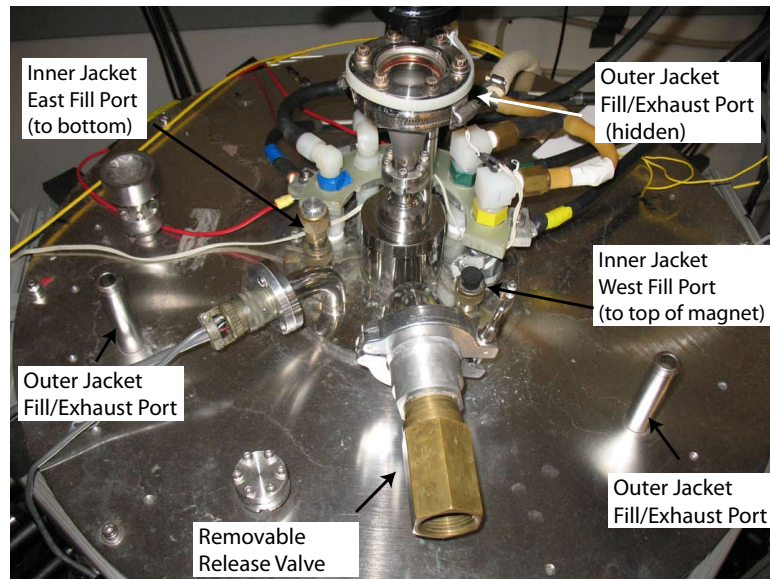


Figure E.2: Top of the high-magnetic field apparatus, showing the access ports for the inner and outer jackets.

The morning of the run, the inner chamber needs to be completely emptied of

nitrogen. It's important not to leave any at the bottom, as the energy cost of freezing this remnant nitrogen will in all likelihood completely deplete your helium supply. That would be bad. In order to remove the helium, use the small rubber transfer tube, located in the northeast corner of the room, leading it from the previously-used inner chamber fill port to the outer jacket spout. Then attach the nitrogen plastic hose, which comes from the building supply, to the rubber exhaust tube at the back of the inner chamber. Turn the nitrogen gas on, and increase the pressure to about 20 psi. Leave the removable pressure release valve at the top of the apparatus on during this step. This will back-pressure the inner chamber and force the nitrogen out into the outer jacket. Monitor this process in order to ensure that you don't over-pressure the inner chamber too much. You can tell the nitrogen is being transferred by seeing if the rubber transfer tube freezes over. You can also feel the liquid pulsing through it by touching it (careful though, it's cold). The inner chamber will empty out before either resistor value changes appreciably. You want to catch it when the chamber is empty, but hasn't started heating up yet. You can double-check that the inner chamber is empty by taking the nitrogen transfer tube, and directing the outflow towards a styrofoam bucket. If only gas is coming out (and the tube is at the bottom of inner jacket!), the inner chamber is empty. It may be necessary to do this anyway, if the outer jacket starts overflowing (depending on how full it was to begin with, this can occur). If this is the case, just fill the styrofoam buckets, and transfer that nitrogen into the big metal dewar under the laser table...that nitrogen will eventually evaporate, and for now that's a fairly safe storage place. Once the inner chamber is empty, turn off the nitrogen gas as soon as possible...we don't want to heat up the chamber any more than necessary.

Alright, the chamber is cold but empty and needs to be filled with helium. Unless

the next graduate student is excessively tall and flexible, this is a two-person job. Remove the pressure release valve and place it to the side for now. For the fill on the first day, use the east-port leading to the bottom of the chamber. On subsequent days, this port will probably be frozen up with ice from any remnant water vapor that was in the air within the tube, so the west-access port leading to the top of the inner chamber needs to be used. Bring in the dewar and attach the helium fill line to it, with the adapter piece. We'll use this pure helium to back-pressure the dewar and force the liquid out through the transfer line. When doing this, be careful not to excessively pressure the dewar, or some of the fail-safe release valves will rupture, at considerable expense. Once the fill line is attached (dewar not pressured yet), have someone help you bring over the helium transfer tube (careful, replacement is 1500 \$) shown in Fig. E.3. This transfer tube consists of a metal tube which is surrounded by a vacuumed jacket. A few times a year, the pressure of this jacket should be checked and pumped down with a roughing pump, to ensure good thermal isolation. Returning to our helium fill, open up the helium dewar and slide in the transfer tube, with the fittings already placed on it. Tighten them down to create a good seal. Make sure that the pressure release valve is completely detached from the chamber; adding liquid helium for the first time will cause a large amount to be boiled off, and it needs an escape route. Have one person let in some helium to back-pressure the dewar while the other holds the transfer tube, not yet placed into the chamber. Once the transfer tube is fully cooled and liquid starts to flow instead of the relatively hotter gas, the tube can be lowered into the central chamber. It is not really necessary to tighten the fittings too much on the chamber side to create a complete seal on the output end. You can now monitor the temperature of the inner chamber by measuring the resistance again. Once it is at helium temperature, the



level gauge above the chamber should start to rise.



Figure E.3: Picture of the liquid helium transfer tube.

When the chamber is full, simply remove the transfer tube and seal up the chamber by replacing the stoppers and pressure release valve. Before turning on the magnet, be sure to close off the turbo valve, then turn off the turbo pump, then the roughing pump, and finally the fan for the turbo pump. This reduces vibrations to the chamber, which lessens the chance of a quench. Turn the center tap on first (for 2.6 T center tap = 1 A), then the quadrupole coils (for 2.6 T anywhere 45-80 works well, depending on your desired trap shape). Once the quadrupole coils current reaches steady-state, you can begin to ramp up the main dipole coils. For reference, while running the dipole coils at 2.6 T (corresponding to 43 A), I usually set the center tap at 1 A and the quadrupole coils to 65.1 A.

### E.3 Lasers

There are three separate lasers required for running the high-magnetic-field trap, as well as a fourth Rydberg/ionization laser. The first two lasers are used to create the primary atom trap outside of the high-field region for  $^{85}\text{Rb}$ . A part of the main trapping beam is also pieced off, and then blue-shifted by about 10 MHz and collimated as a small 1 mm beam before being recombined with the trapping beam. This ‘pusher’ beam is used to eject the atoms out the primary and into the high-B trap, giving the atoms enough kinetic energy. The molasses lasers forms the trap in the high-magnetic field, and is locked to the Fabry-Pérot on the table.

Before the data run, make sure all the lasers are locking to the proper frequencies. The frequency shift of the high-B trap is a net 14 GHz/T, so at 2.6 T this corresponds to 36.4 GHz. Use the wavemeter to make sure that the molasses laser is in the proper range. Note that the last digit of the wavemeter varies a little from day to day, so you’ll need to scan throughout that range to find the transition. Ensure that the power is optimized through the molasses fiber and that the polarization isn’t drifting: since we split this beam up on the output using beam cubes and the trap is highly sensitive to any intensity asymmetries, any drift will negatively affect the trap.

The lengthiest preparation is to ensure that all six molasses beams are going through the chamber properly. Visually inspect all the mirrors and dust/clean them if necessary. Follow the beams along their paths, making sure that they are not missing or being clipped by any mirror. Place a CCD camera looking at an index card after the chamber, to inspect the beams through the chamber. The beam profile should be circular and have a uniform intensity profile. This will have a huge effect on trap lifetime, so spend some time on this step. Figure E.4 demonstrates examples

of misaligned and optimized molasses beams, after a pass through the chamber.

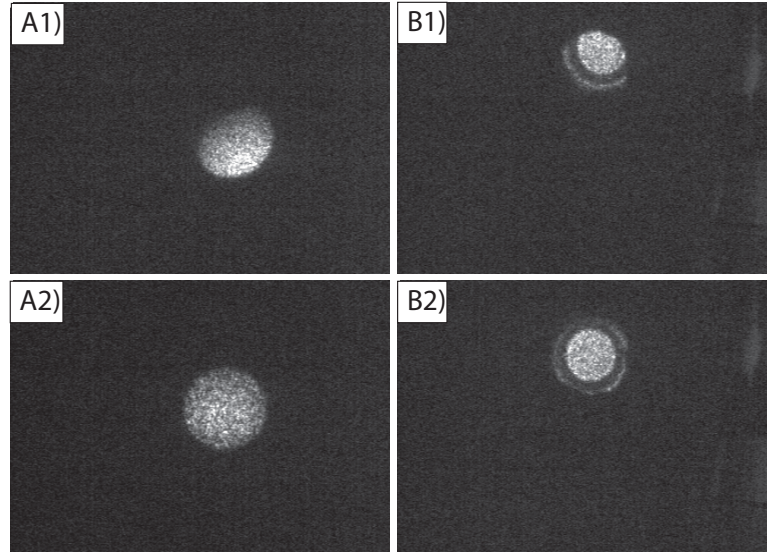


Figure E.4: Sample molasses beam profiles, for the case of transverse (A) and longitudinal (B) molasses beams once they have traveled through the chamber. (A1) and (B1) are examples of misaligned beams, while (A2) and (B2) are reasonably-well optimized. In the case of the axial molasses beams, when optimized a symmetric ‘halo’ can be seen around the central beam profile, as a result of the beam clipping on the optical ports.

The pusher beam also needs to be aligned through the center of the high-field chamber to the back MCP. Turn up the pusher beam power by splitting off more light into it on the main optics table. Even with the MCP power off, you can detect fluorescence from the phosphor screen. Note that to do this, the primary trap gate valve needs to be opened. Align the beam to the center of the MCP, using the last two mirror/glass plate before the pusher beam joins the main trapping beam path.

Finally, the excitation laser should be prepared. For this, you have the choice of the high-B cw laser (max power tot trap 2-5 mW), the Cryomot cw laser (max power to trap 30 mW), or the pulsed dye laser (PDL), which has  $\sim 2-3$  mJ per pulse, and runs at 10 Hz. Whatever the case, ensure that the laser is running properly and at the proper frequency before the run starts. For the Cryomot laser, which I’ve been using recently, make sure that the coupling through the fiber is optimized, and that

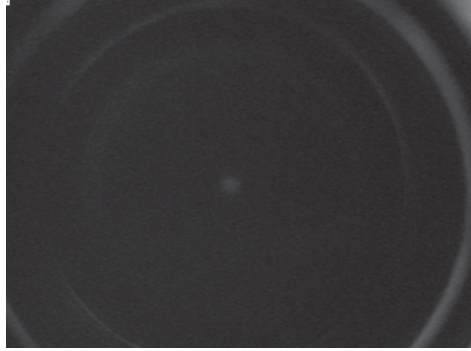


Figure E.5: Sample image showing the pusher beam centered upon the MCP and phosphor screen. Here the power in the pusher beam has been increased to be able to align the beam.

the polarization is not drifting. Polarization drifts occur when the laser polarization is either drifting on the input side, or isn't aligned correctly with the fiber axis. This can present a significant problem in the high-magnetic-field trap, as even above the ionization threshold the ionization rate depends strongly on the laser polarization. Take some time to make sure about this before the run.

#### E.4 Counts

Once the magnet is on, and all the lasers locked and ready, the next step is to look for counts or a signal out of the trap. In order to do this, we need to direct any ionized electrons out of the central region and towards the MCP. We need to set the electrodes such that there is a negative voltage on the LVIS side, and a positive increasing voltage towards the MCP side. From LVIS to MCP, the electrodes go: LCAP-LFI-MFI-MCAP-Tube1-Tube2-(MCP). The two 'tubes' should be pretty much preset, I don't usually change them throughout runs. If using the PDL, apply 0 electric field throughout the excitation pulse, then a negative pulse on the LFI to direct the electrons to the MCP. When using either 480 nm cw lasers, I usually try to increase the detected signal by running with a Penning trap: apply strong negative voltages (-400) to both MCAP/LCAPs in order to 'trap' the electrons for

an indefinite period of time with both the LFI/MFIs at 0 V, then simultaneously bring the MCAP to 0V and the LFI to a large negative voltage. This will give a sharper pulsed signal instead of a slow steady count rate out of the trap, which means that this pulse can then be integrated to get a more quantitative feel for the trap strength.

Turn the MCP up (both dials, at the same time) to around 8 turns or so. Whenever you turn the MCP up, make sure that the MCP screen isn't being saturated (blinding white light bleeding into neighboring camera cells, etc), as this can damage the MCP. Note that there's already a tiny blip or 'blind spot' on the MCP. What we're initially looking for is just a few scattered counts. Now is also a good time to double-check that you opened up the primary gate valve...many tears of frustration if you forget that step. With the valve open and the pusher having an effect on the primary trap, we know that we're pushing the atoms into the central chamber. Turn up the molasses to a fairly high value (a few mW out of the fiber, which translates to  $\sim 1 I_{\text{SAT}}$ ). Block the two transverse high-field molasses beams with a card. Visually check that your blue ionization beam is roughly aligned with the trap by checking that it is centered on both input and output ports (if using PDL- goggles! Safety first!). Double-check that your electric field pulse timing is correct, and that the camera gate is aligned with the time in which the electrons should hit the MCP, only a few ns after your LFI pulse.

It is usually easiest at first to manually scan the molasses frequency grating knob and watch the phosphor screen for counts. Once you find the trapping transition resonance, lock the molasses laser to the closest Fabry-Pérot peak, and use one of the Labview programs to scan the Fabry-Pérot peak back to frequency resonance. A quick aside: the Fabry-Pérot does have a temperature-stabilization PID box, located

right below the table. You can check its stability by measuring the current being sent to the heating tape within the box; there's a ammeter in series. It normally runs at 0.50 A, but should be fine as long as the current output is steady, and it is not at the output current limit of the circuit ( $\sim 1$  A).

Once you've found the resonance, stay just to red-detuned side of the peak count rate. This ensures that when you optimize the various parameters, you are optimizing the trapped atom signal (from the atoms lying at the potential), and not the atomic beam signal.

The first set of parameters to adjust are associated with the input flux of atoms. These include both frequency locks for the PMOT trapping and repump beams, the two PMOT transverse coil currents (to adjust the  $x-y$  position of the primary trap), the pusher power splitting on the main optics table, and the direction of the pusher beam (last mirror before joining the large PMOT trap beam). Optimize the position of the blue ionization beam, to ensure that it is hitting the center of the trap. Now optimize the splitting of the longitudinal high-field molasses beams. Note that this splitting is very sensitive.

Once this set of optimizations has been completed, scan through the molasses frequency peak again to make sure that you're still on the red-detuned side. Run through the entire set of parameters a second or a third time. If the MCP is becoming saturated, turn it down slightly, note the new signal level, and continue with this pattern. You can also begin to turn down the molasses beam power, which is controlled by a MUX in the main equipment rack. Attached is a voltmeter for a more quantitative measurement of the molasses beam power. I usually start at molasses beam power corresponding to 0.5 V on this voltmeter, eventually lowering it down to 0.1 V for a fully optimized trap. The exact intensity will depend on the fiber

coupling, but correspond to a total intensity of  $\sim 0.1 I_{\text{SAT}}$  for the best traps.

After several iterations, remember that we have previously blocked the transverse molasses beams. If atoms are at the center of the high-field trap, unblocking these beams (make sure that the retro-reflections were also properly aligned) will result in a marked jump in the trap signal. Letting these beams in also gives us a new set of parameters to optimize. The trap is highly sensitive to these beam positions, and will be harmed if there's a power asymmetry between the incident and retro-reflected beams. Optimize the transverse beams one at a time by blocking the other one. The retro-reflection is optimized by adjusting that mirror while looking at the trap signal strength. You can also optimize the incident beam by blocking the retro-reflection with a card, and then carefully playing with the last mirror before the trap, looking to decrease the signal strength as much as possible ('killing' the trap through beam asymmetry). For this, it might be necessary to turn the MCP up (remember to turn it back down before removing the card blocking the retro-reflection). This optimization technique isn't terribly sensitive, so it might only be useful if something is quite misaligned.

If you have a detectable trap lifetime (you can estimate this by blocking the PMOT beams and watching the rate at which the signal level decreases), you can also adjust the angle of the two longitudinal molasses beams. Note that these are very sensitive, so make small adjustments.

Cycle through all this list of steps several times, while periodically lowering the molasses beam power. If the trap is well-balanced, lowering the molasses beam power will not actually decrease the observed signal strength: though you are effectively lowering the excitation rate, the lifetime increase corresponding to these lower powers means that more atoms are trapped, and so the resulting signal is roughly constant.

If for some reason there does not seem to be a trap lifetime, or it does not seem to extend beyond 2-3 s, take a step back and check that all the parameters are properly set. You can also double-check the molasses beam alignment with a CCD camera; it's very easy to accidentally bump a mirror during the fill or optimization process.

You will eventually reach a regime of diminishing returns, where the long trap lifetime (10-20 s) makes the trap excessively hard to optimize. This is generally a good point to stop optimizing, and move on to your planned experiments. With the trap performing well, despite the narrow trapping linewidth (3-4 MHz) the trap drifts are very small ( $\sim 2$  MHz/hour), and this gives you a very stable platform from which to work. If the counts do decrease, make sure that your laser locks have not drifted (molasses, PMOT main, PMOT repump) before touching anything else. If that does not solve the problem, check the longitudinal/transverse molasses beam splitting waveplates.

As a final note, if you are using either cw laser, be aware that in the high-magnetic-field resonances also exist above the ionization limit. These can significantly increase the count rate if you use the cw 480 nm laser, and your frequency resonant with one, but the downside is that they are also of course frequency and polarization-dependent. If you are on one of these resonances, any drift in the blue cw laser frequency or polarization can therefore cause signal drifts that look like a sudden change in your trap performance.



## E.5 Checklist

The following is a brief, non-exhaustive checklist of tasks that need to be done before a data run:

A week prior:

1. Order liquid helium.
2. Check that there is sufficient helium gas.
3. If using the Cryomot cw laser, book time with the other students.
4. If using the High-B cw laser, optimize its wavelength and power output.
5. If using the PDL, mix a new batch of dye. Replace the dye and check the pulsed output with the bolometer.
6. Check that the Fabry-Pérots (both cw blue, molasses) are all properly temperature-stabilized.
7. Check and tune all the laser frequencies.
8. Optimize the powers through all the fibers.
9. If some time has passed since the last run, switch the PMOT coils to the anti-Helmholtz configuration and create a standard MOT. If you do this, make sure that once done you switch these coils back to the standard Helmholtz configuration.
10. Check that the pusher beam is properly aligned through the PMOT apex, all the way to the center of the MCP phosphor screen.
11. Check all your pulse timing/excitation schemes.
12. Clean the lab before a run.

The day before:

1. Fill the outer jacket with liquid nitrogen.
2. Fill the inner jacket with liquid nitrogen.
3. Check and optimize all the high-field molasses beams.
4. If using the Cryomot cw laser, change the wavelength to the desired setting, optimize the power, and couple the beam properly through the fiber all the way to the high-B side. Note that this coupling efficiency is rather low ( $\sim 25\%$  to  $\sim 30\%$ ), and can be difficult to work with at times.
5. Refill the nitrogen dewar at the loading dock.
6. Make sure that the Helium dewars have arrived.

The first morning:

1. Turn on the large air conditioner in the corner of the lab. Make sure that the water input and return ports are open. They are located on the wall, where the transfer tube hangs.
2. Empty the inner jacket of nitrogen by back-pressuring the system, making sure that it's empty.
3. Top off the outer jacket with the nitrogen dewar.
4. Fill up the inner jacket with liquid Helium, using the east fill port. You will probably need a hand with this.
5. Make sure that the water cooling is on (this cools the main PMOT coils, as well as the zoom coil for the MCP).
6. Optimize laser frequencies, locks, and fiber couplings.

7. Close the turbo pump valve. Once this is closed, turn off the turbo pump. When this has finished spinning, turn off the turbo pump fan and the roughing pump.
8. Double-check the high-field molasses alignment.
9. Open up the PMOT gate valve.
10. Before turning on the high fields, make sure that everything else is ready.
11. Turn on the center tap coil first, then the quadrupole coils, and finally the main dipole coils.
12. If used, turn on the zoom coil last, after making sure that the water cooling is on.
13. Turn the MCP up (to around 8 turns to start, on both dials).
14. Optimize the trap as described in the text above.
15. At the end of the day, turn off the coils in the reverse order: first the dipole coil, then the quadrupole coils and finally the center tap.
16. Turn everything else off in the reverse order.
17. Make sure that both PMOT main coils and the zoom coil are all off before turning off the water cooling.
18. Top off the outer jacket with nitrogen to make sure that it stays cool overnight. Be very careful not to bump anything, your system is probably fully optimized at this point.

## BIBLIOGRAPHY

## BIBLIOGRAPHY

- [1] S. Haroche. Entanglement, coherence, and the quantum-classical boundary.
- [2] M. S. O'Sullivan and B. P. Stoicheff. Scalar polarizabilities and avoided crossings of high rydberg states in rb. *Phys. Rev. A*, 31:2718–2720, Apr 1985. doi: 10.1103/PhysRevA.31.2718. URL <http://link.aps.org/doi/10.1103/PhysRevA.31.2718>.
- [3] T.F. Gallagher. *Rydberg Atoms*. Cambridge Monographs on Atomic, Molecular and Chemical Physics. Cambridge University Press, 2005. ISBN 9780521021661. URL <http://books.google.com/books?id=8JIpEhHWT-cC>.
- [4] Ping Zhao, W. Lichten, Zhi-Xiang Zhou, H. P. Layer, and J. C. Bergquist. Rydberg constant and fundamental atomic physics. *Phys. Rev. A*, 39:2888–2898, Mar 1989. doi: 10.1103/PhysRevA.39.2888. URL <http://link.aps.org/doi/10.1103/PhysRevA.39.2888>.
- [5] Ulrich D. Jentschura, Peter J. Mohr, Joseph N. Tan, and Benedikt J. Wundt. Fundamental constants and tests of theory in rydberg states of hydrogenlike ions. *Phys. Rev. Lett.*, 100:160404, Apr 2008. doi: 10.1103/PhysRevLett.100.160404. URL <http://link.aps.org/doi/10.1103/PhysRevLett.100.160404>.
- [6] I. Mourachko, Wenhui Li, and T. F. Gallagher. Controlled many-body interactions in a frozen rydberg gas. *Phys. Rev. A*, 70:031401, Sep 2004. doi: 10.1103/PhysRevA.70.031401. URL <http://link.aps.org/doi/10.1103/PhysRevA.70.031401>.
- [7] Steven L. Rolston. Ultracold neutral plasmas. *Physics*, 1:2, Jul 2008. doi: 10.1103/Physics.1.2. URL <http://link.aps.org/doi/10.1103/Physics.1.2>.
- [8] J. M. Raimond, P. Goy, M. Gross, C. Fabre, and S. Haroche. Collective absorption of black-body radiation by rydberg atoms in a cavity: An experiment on bose statistics and brownian motion. *Phys. Rev. Lett.*, 49:117–120, Jul 1982. doi: 10.1103/PhysRevLett.49.117. URL <http://link.aps.org/doi/10.1103/PhysRevLett.49.117>.
- [9] S. Haroche and J.M. Raimond. *Exploring the Quantum: Atoms, Cavities, and Photons*. Oxford graduate texts in mathematics. OUP Oxford, 2006. ISBN 9780198509141. URL <http://books.google.com/books?id=QY6YuU-Qi-AC>.
- [10] B. Wyker, S. Ye, F. B. Dunning, S. Yoshida, C. O. Reinhold, and J. Burgdörfer. Creating and transporting trojan wave packets. *Phys. Rev. Lett.*, 108:043001, Jan 2012. doi: 10.1103/PhysRevLett.108.043001. URL <http://link.aps.org/doi/10.1103/PhysRevLett.108.043001>.
- [11] K.R. Overstreet, A. Schwettmann, J. Tallant, D. Booth, and J. P. Shaffer. Observation of electric-field-induced cs rydberg atom macrodimers. *Nature Physics*, 5:581, June 2009. doi: 10.1038/nphys1307. URL <http://dx.doi.org/10.1038/nphys1307>.
- [12] M. Saffman, T. G. Walker, and K. Mølmer. Quantum information with rydberg atoms. *Rev. Mod. Phys.*, 82:2313–2363, Aug 2010. doi: 10.1103/RevModPhys.82.2313. URL <http://link.aps.org/doi/10.1103/RevModPhys.82.2313>.

- [13] D. Jaksch, J. I. Cirac, P. Zoller, S. L. Rolston, R. Côté, and M. D. Lukin. Fast quantum gates for neutral atoms. *Phys. Rev. Lett.*, 85:2208–2211, Sep 2000. doi: 10.1103/PhysRevLett.85.2208. URL <http://link.aps.org/doi/10.1103/PhysRevLett.85.2208>.
- [14] Steven Chu, J. E. Bjorkholm, A. Ashkin, and A. Cable. Experimental observation of optically trapped atoms. *Phys. Rev. Lett.*, 57:314–317, Jul 1986. doi: 10.1103/PhysRevLett.57.314. URL <http://link.aps.org/doi/10.1103/PhysRevLett.57.314>.
- [15] David E. Pritchard. Cooling neutral atoms in a magnetic trap for precision spectroscopy. *Phys. Rev. Lett.*, 51:1336–1339, October 1983. URL [http://prl.aps.org/pdf/PRL/v51/i15/p1336\\_1](http://prl.aps.org/pdf/PRL/v51/i15/p1336_1).
- [16] S. Gupta, K. Dieckmann, Z. Hadzibabic, and D. E. Pritchard. Contrast interferometry using bose-einstein condensates to measure  $h/m$  and  $\alpha$ . *Phys. Rev. Lett.*, 89:140401, Sep 2002. doi: 10.1103/PhysRevLett.89.140401. URL <http://link.aps.org/doi/10.1103/PhysRevLett.89.140401>.
- [17] S. Aubin, E. Gomez, L.A. Orozco, and G.D. Sprouse. High efficiency magneto-optical trap for unstable isotopes. *Rev. Sci. Instrum.*, 74:4342, Sep 2003. URL <http://dx.doi.org/10.1063/1.1606093>.
- [18] X. Du, K. Bailey, Z.-T. Lu, P. Mueller, T.P. O’Connor, and L. Young. An atom trap system for practical  $^{81}\text{Kr}$  dating. *Rev. Sci. Instrum.*, 75:3224, Sep 2004. URL <http://dx.doi.org/10.1063/1.1790562>.
- [19] E. A. Cornell and C. E. Wieman. Nobel lecture: Bose-einstein condensation in a dilute gas, the first 70 years and some recent experiments. *Rev. Mod. Phys.*, 74:875–893, Aug 2002. doi: 10.1103/RevModPhys.74.875. URL <http://link.aps.org/doi/10.1103/RevModPhys.74.875>.
- [20] Kurt Gibble and Steven Chu. Laser-cooled cs frequency standard and a measurement of the frequency shift due to ultracold collisions. *Phys. Rev. Lett.*, 70:1771–1774, Mar 1993. doi: 10.1103/PhysRevLett.70.1771. URL <http://link.aps.org/doi/10.1103/PhysRevLett.70.1771>.
- [21] M. Takamoto, F.-L. Hong, R. Higashi, and H. Katori. An optical lattice clock. *Phys. Rev. Lett.*, 435:321–324, May 2005. doi: 10.1038/nature03541. URL <http://www.nature.com/nature/journal/v435/n7040/pdf/nature03541.pdf>.
- [22] Carl E. Wieman, David E. Pritchard, and David J. Wineland. Atom cooling, trapping, and quantum manipulation. *Rev. Mod. Phys.*, 71:S253–S262, Mar 1999. doi: 10.1103/RevModPhys.71.S253. URL <http://link.aps.org/doi/10.1103/RevModPhys.71.S253>.
- [23] Rudolf Grimm, Matthias Weidemller, and Yurii B. Ovchinnikov. Optical dipole traps for neutral atoms. volume 42 of *Advances In Atomic, Molecular, and Optical Physics*, pages 95 – 170. Academic Press, 2000. doi: 10.1016/S1049-250X(08)60186-X. URL <http://www.sciencedirect.com/science/article/pii/S1049250X0860186X>.
- [24] David E. Pritchard. Cooling neutral atoms in a magnetic trap for precision spectroscopy. *Phys. Rev. Lett.*, 51:1336–1339, Oct 1983. doi: 10.1103/PhysRevLett.51.1336. URL <http://link.aps.org/doi/10.1103/PhysRevLett.51.1336>.
- [25] H.G. Dehmelt. Radiofrequency spectroscopy of stored ions i: Storage. volume 3 of *Advances in Atomic and Molecular Physics*, pages 53 – 72. Academic Press, 1968. doi: 10.1016/S0065-2199(08)60170-0. URL <http://www.sciencedirect.com/science/article/pii/S0065219908601700>.

- [26] Lowell S. Brown and Gerald Gabrielse. Geonium theory: Physics of a single electron or ion in a penning trap. *Rev. Mod. Phys.*, 58:233–311, Jan 1986. doi: 10.1103/RevModPhys.58.233. URL <http://link.aps.org/doi/10.1103/RevModPhys.58.233>.
- [27] J.J. Bollinger, J.M. Kriesel, T.B. Mitchell, L.B. King, M.J. Jensen, W.M. Itano, and D.H.E. Dubin. Laser-cooled ion plasmas in penning traps. *J. Phys. B: At. Mol. Opt. Phys.*, 36:499–510, Jan 2003. doi: 10.1088/0953-4075/36/3/308. URL [http://iopscience.iop.org/0953-4075/36/3/308/pdf/0953-4075\\_36\\_3\\_308.pdf](http://iopscience.iop.org/0953-4075/36/3/308/pdf/0953-4075_36_3_308.pdf).
- [28] Daniel H. E. Dubin and T. M. O’Neil. Trapped nonneutral plasmas, liquids, and crystals (the thermal equilibrium states). *Rev. Mod. Phys.*, 71:87–172, Jan 1999. doi: 10.1103/RevModPhys.71.87. URL <http://link.aps.org/doi/10.1103/RevModPhys.71.87>.
- [29] Wolfgang Paul. Electromagnetic traps for charged and neutral particles. *Rev. Mod. Phys.*, 62:531–540, Jul 1990. doi: 10.1103/RevModPhys.62.531. URL <http://link.aps.org/doi/10.1103/RevModPhys.62.531>.
- [30] Z.-T. Lu and K.D.A. Wendt. Laser-based methods for ultrasensitive trace-isotope analyses. *Rev. Sci. Instrum.*, 74:1169, Mar 2003. doi: 10.1063/1.1535232. URL <http://dx.doi.org/10.1063/1.1535232>.
- [31] G. Andresen, W. Bertsche, A. Boston, P. D. Bowe, C. L. Cesar, S. Chapman, M. Charlton, M. Chartier, A. Deutsch, J. Fajans, M. C. Fujiwara, R. Funakoshi, D. R. Gill, K. Gomboroff, J. S. Hangst, R. S. Hayano, R. Hydromako, M. J. Jenkins, L. V. Jørgensen, L. Kurchaninov, N. Madsen, P. Nolan, K. Olchanski, A. Olin, A. Povilus, F. Robicieux, E. Sarid, D. M. Silveira, J. W. Storey, H. H. Telle, R. I. Thompson, D. P. van der Werf, J. S. Wurtele, and Y. Yamazaki. Antimatter plasmas in a multipole trap for antihydrogen. *Phys. Rev. Lett.*, 98:023402, Jan 2007. doi: 10.1103/PhysRevLett.98.023402. URL <http://link.aps.org/doi/10.1103/PhysRevLett.98.023402>.
- [32] G. Gabrielse, P. Laroche, D. Le Sage, B. Levitt, W. S. Kolthammer, I. Kuljanishvili, R. McConnell, J. Wrubel, F. M. Esser, H. Glückler, D. Grzonka, G. Hansen, S. Martin, W. Oelert, J. Schillings, M. Schmitt, T. Sefzick, H. Soltner, Z. Zhang, D. Comeau, M. C. George, E. A. Hessels, C. H. Storry, M. Weel, A. Speck, F. Nillius, J. Walz, and T. W. Hänsch. Antiproton confinement in a penning-ioffe trap for antihydrogen. *Phys. Rev. Lett.*, 98:113002, Mar 2007. doi: 10.1103/PhysRevLett.98.113002. URL <http://link.aps.org/doi/10.1103/PhysRevLett.98.113002>.
- [33] J. R. Guest, J.-H. Choi, E. Hansis, A. P. Povilus, and G. Raithel. Laser cooling and magnetic trapping at several tesla. *Phys. Rev. Lett.*, 94:073003, Feb 2005. doi: 10.1103/PhysRevLett.94.073003. URL <http://link.aps.org/doi/10.1103/PhysRevLett.94.073003>.
- [34] V. S. Bagnato, G. P. Lafyatis, A. G. Martin, E. L. Raab, R. N. Ahmad-Bitar, and D. E. Pritchard. Continuous stopping and trapping of neutral atoms. *Phys. Rev. Lett.*, 58:2194–2197, May 1987. doi: 10.1103/PhysRevLett.58.2194. URL <http://link.aps.org/doi/10.1103/PhysRevLett.58.2194>.
- [35] F. A. Jenkins and E. Segrè. The quadratic zeeman effect. *Phys. Rev.*, 55:52–58, Jan 1939. doi: 10.1103/PhysRev.55.52. URL <http://link.aps.org/doi/10.1103/PhysRev.55.52>.
- [36] Myron L. Zimmerman, Jarbas C. Castro, and Daniel Kleppner. Diamagnetic structure of na rydberg states. *Phys. Rev. Lett.*, 40:1083–1086, Apr 1978. doi: 10.1103/PhysRevLett.40.1083. URL <http://link.aps.org/doi/10.1103/PhysRevLett.40.1083>.
- [37] George R. Welch, Michael M. Kash, Chun-ho Iu, Long Hsu, and Daniel Kleppner. Experimental study of energy-level statistics in a regime of regular classical motion. *Phys. Rev. Lett.*, 62:893–896, Feb 1989. doi: 10.1103/PhysRevLett.62.893. URL <http://link.aps.org/doi/10.1103/PhysRevLett.62.893>.

- [38] J.-H. Choi, J. R. Guest, A. P. Povilus, E. Hansis, and G. Raithel. Magnetic trapping of long-lived cold rydberg atoms. *Phys. Rev. Lett.*, 95:243001, Dec 2005. doi: 10.1103/PhysRevLett.95.243001. URL <http://link.aps.org/doi/10.1103/PhysRevLett.95.243001>.
- [39] J.-H. Choi, B. Knuffman, X. H. Zhang, A. P. Povilus, and G. Raithel. Trapping and evolution dynamics of ultracold two-component plasmas. *Phys. Rev. Lett.*, 100:175002, Apr 2008. doi: 10.1103/PhysRevLett.100.175002. URL <http://link.aps.org/doi/10.1103/PhysRevLett.100.175002>.
- [40] G. et al. Andresen. Confinement of antihydrogen for 1,000 seconds. *Nature Physics*, 7:558–564, May 2011. doi: 10.1038/nphys2025. URL <http://www.nature.com/nphys/journal/v7/n7/pdf/nphys2025.pdf>.
- [41] G. Gabrielse, R. Kalra, W. S. Kolthammer, R. McConnell, P. Richerme, D. Grzonka, W. Oelert, T. Sefzick, M. Zielinski, D. W. Fitzakerley, M. C. George, E. A. Hessels, C. H. Storry, M. Weel, A. Müllers, and J. Walz. Trapped antihydrogen in its ground state. *Phys. Rev. Lett.*, 108:113002, Mar 2012. doi: 10.1103/PhysRevLett.108.113002. URL <http://link.aps.org/doi/10.1103/PhysRevLett.108.113002>.
- [42] T. C. Killian, M. J. Lim, S. Kulin, R. Dumke, S. D. Bergeson, and S. L. Rolston. Formation of rydberg atoms in an expanding ultracold neutral plasma. *Phys. Rev. Lett.*, 86:3759–3762, Apr 2001. doi: 10.1103/PhysRevLett.86.3759. URL <http://link.aps.org/doi/10.1103/PhysRevLett.86.3759>.
- [43] Wenhui Li, Michael W. Noel, Michael P. Robinson, Paul J. Tanner, Thomas F. Gallagher, Daniel Comparat, Bruno Laburthe Tolra, Nicolas Vanhaecke, Thibault Vogt, Nassim Zahzam, Pierre Pillet, and Duncan A. Tate. Evolution dynamics of a dense frozen rydberg gas to plasma. *Phys. Rev. A*, 70:042713, Oct 2004. doi: 10.1103/PhysRevA.70.042713. URL <http://link.aps.org/doi/10.1103/PhysRevA.70.042713>.
- [44] H. Friedrich. *Theoretical Atomic Physics*. Advanced Texts in Physics Series. Springer-Verlag, 2006. ISBN 9783540641247. URL <http://books.google.com.au/books?id=7JyfQB4co1IC>.
- [45] D. Poeter. Intel bets on moore’s law for another decade. *PC Magazine*, Sept 2012. URL <http://www.pcmag.com/article2/0,2817,2409635,00.asp>.
- [46] V.V. Zhirnov, R.K. III Cavin, J.A. Hutchby, and G.E. Bourianoff. Limits to binary logic switch scalinga gedanken model. *Proceedings of the IEEE*, 91:1934, Nov 2003. URL <http://ieeexplore.ieee.org/stamp/stamp.jsp?tp=&arnumber=1240081>.
- [47] Artur K. Ekert. Quantum cryptography based on bell’s theorem. *Phys. Rev. Lett.*, 67:661–663, Aug 1991. doi: 10.1103/PhysRevLett.67.661. URL <http://link.aps.org/doi/10.1103/PhysRevLett.67.661>.
- [48] I.L. Chuang, R. Laflamme, P.W. Shor, and W.H. Zurek. Quantum computers, factoring, and decoherence. *Science*, 92:1633, Dec 2003. doi: 10.1126/science.270.5242.1633. URL <http://dx.doi.org/10.1126/science.270.5242.1633>.
- [49] L.M.K. Vandersypen, M. Steffen, G. Breyta, C.S. Yannoni, M.H. Sherwood, and I.L. Chuang. Experimental realization of shor’s quantum factoring algorithm using nuclear magnetic resonance. *Nature*, 414:883, Dec 2001. doi: 10.1038/414883a. URL <http://dx.doi.org/10.1038/414883a>.
- [50] Lov K. Grover. Quantum mechanics helps in searching for a needle in a haystack. *Phys. Rev. Lett.*, 79:325–328, Jul 1997. doi: 10.1103/PhysRevLett.79.325. URL <http://link.aps.org/doi/10.1103/PhysRevLett.79.325>.



- [51] David P. DiVincenzo. The physical implementation of quantum computation. *Fortschritte der Physik*, 48(9-11):771–783, 2000. ISSN 1521-3978. doi: 10.1002/1521-3978(200009)48:9/11<771::AID-PROP771>3.0.CO;2-E. URL [http://dx.doi.org/10.1002/1521-3978\(200009\)48:9/11<771::AID-PROP771>3.0.CO;2-E](http://dx.doi.org/10.1002/1521-3978(200009)48:9/11<771::AID-PROP771>3.0.CO;2-E).
- [52] E. Urban, T.A. Johnson, T. Henage, L. Isenhower, D.D. Yavuz, T.G Walker, and M. Saffman. Observation of rydberg blockade between two atoms. *Nature Physics*, 5:110, Jan 2009. doi: 10.1038/nphys1178. URL <http://dx.doi.org/10.1038/nphys1178>.
- [53] H. Kübler, J.P. Shaffer, T. Baluktsian, R. Löw, and T. Pfau. Coherent excitation of rydberg atoms in micrometre-sized atomic vapour cells. *Nature Photonics*, 4:112, Jan 2009. doi: 10.1038/nphoton.2009.260. URL <http://dx.doi.org/10.1038/nphoton.2009.260>.
- [54] T. Wilk, A. Gaëtan, C. Evellin, J. Wolters, Y. Miroshnychenko, P. Grangier, and A. Browaeys. Entanglement of two individual neutral atoms using rydberg blockade. *Phys. Rev. Lett.*, 104:010502, Jan 2010. doi: 10.1103/PhysRevLett.104.010502. URL <http://link.aps.org/doi/10.1103/PhysRevLett.104.010502>.
- [55] L. Isenhower, E. Urban, X. L. Zhang, A. T. Gill, T. Henage, T. A. Johnson, T. G. Walker, and M. Saffman. Demonstration of a neutral atom controlled-not quantum gate. *Phys. Rev. Lett.*, 104:010503, Jan 2010. doi: 10.1103/PhysRevLett.104.010503. URL <http://link.aps.org/doi/10.1103/PhysRevLett.104.010503>.
- [56] Thibault Vogt, Matthieu Viteau, Jianming Zhao, Amodsen Chotia, Daniel Comparat, and Pierre Pillet. Dipole blockade at förster resonances in high resolution laser excitation of rydberg states of cesium atoms. *Phys. Rev. Lett.*, 97:083003, Aug 2006. doi: 10.1103/PhysRevLett.97.083003. URL <http://link.aps.org/doi/10.1103/PhysRevLett.97.083003>.
- [57] Thibault Vogt, Matthieu Viteau, Amodsen Chotia, Jianming Zhao, Daniel Comparat, and Pierre Pillet. Electric-field induced dipole blockade with rydberg atoms. *Phys. Rev. Lett.*, 99:073002, Aug 2007. doi: 10.1103/PhysRevLett.99.073002. URL <http://link.aps.org/doi/10.1103/PhysRevLett.99.073002>.
- [58] A. Reinhard, K. C. Younge, and G. Raithel. Effect of förster resonances on the excitation statistics of many-body rydberg systems. *Phys. Rev. A*, 78:060702, Dec 2008. doi: 10.1103/PhysRevA.78.060702. URL <http://link.aps.org/doi/10.1103/PhysRevA.78.060702>.
- [59] D. Tong, S. M. Farooqi, J. Stanojevic, S. Krishnan, Y. P. Zhang, R. Côté, E. E. Eyler, and P. L. Gould. Local blockade of rydberg excitation in an ultracold gas. *Phys. Rev. Lett.*, 93:063001, Aug 2004. doi: 10.1103/PhysRevLett.93.063001. URL <http://link.aps.org/doi/10.1103/PhysRevLett.93.063001>.
- [60] Rolf Heidemann, Ulrich Raitzsch, Vera Bendkowsky, Björn Butscher, Robert Löw, Luis Santos, and Tilman Pfau. Evidence for coherent collective rydberg excitation in the strong blockade regime. *Phys. Rev. Lett.*, 99:163601, Oct 2007. doi: 10.1103/PhysRevLett.99.163601. URL <http://link.aps.org/doi/10.1103/PhysRevLett.99.163601>.
- [61] A. Reinhard, T. Cubel Liebisch, B. Knuffman, and G. Raithel. Level shifts of rubidium rydberg states due to binary interactions. *Phys. Rev. A*, 75:032712, Mar 2007. doi: 10.1103/PhysRevA.75.032712. URL <http://link.aps.org/doi/10.1103/PhysRevA.75.032712>.
- [62] I. Mourachko, D. Comparat, F. de Tomasi, A. Fioretti, P. Nosbaum, V. M. Akulin, and P. Pillet. Many-body effects in a frozen rydberg gas. *Phys. Rev. Lett.*, 80:253, Jan 1998. doi: 10.1103/PhysRevLett.80.253. URL <http://link.aps.org/doi/10.1103/PhysRevLett.80.253>.

- [63] W. R. Anderson, J. R. Veale, and T. F. Gallagher. Resonant dipole-dipole energy transfer in a nearly frozen rydberg gas. *Phys. Rev. Lett.*, 80:249–252, Jan 1998. doi: 10.1103/PhysRevLett.80.249. URL <http://link.aps.org/doi/10.1103/PhysRevLett.80.249>.
- [64] K. A. Safinya, J. F. Delpuch, F. Gounand, W. Sandner, and T. F. Gallagher. Resonant rydberg-atom-rydberg-atom collisions. *Phys. Rev. Lett.*, 47:405–408, Aug 1981. doi: 10.1103/PhysRevLett.47.405. URL <http://link.aps.org/doi/10.1103/PhysRevLett.47.405>.
- [65] P. Bohlouli-Zanjani, J. A. Petrus, and J. D. D. Martin. Enhancement of rydberg atom interactions using ac stark shifts. *Phys. Rev. Lett.*, 98:203005, May 2007. doi: 10.1103/PhysRevLett.98.203005. URL <http://link.aps.org/doi/10.1103/PhysRevLett.98.203005>.
- [66] Thad G. Walker and M. Saffman. Zeros of rydberg-rydberg föster interactions. *Journal of Physics B: Atomic, Molecular and Optical Physics*, 38(2):S309, 2005. URL <http://stacks.iop.org/0953-4075/38/i=2/a=022>.
- [67] L. I. Schiff and H. Snyder. Theory of the quadratic zeeman effect. *Phys. Rev.*, 55:59–63, Jan 1939. doi: 10.1103/PhysRev.55.59. URL <http://link.aps.org/doi/10.1103/PhysRev.55.59>.
- [68] J.C. Gay and D. Delande. The hydrogen atom in a magnetic field. symmetries in the low field diamagnetic limit. *Comments At. Mol. Physics.*, 13(6):275, 1983. URL <http://www.spectro.jussieu.fr/Chaos/perso/delande/articles/10.pdf>.
- [69] T. van der Veldt, W. Vassen, and W. Hogervorst. Helium rydberg states in parallel electric and magnetic fields. *Journal of Physics B: Atomic, Molecular and Optical Physics*, 26(13):1945, 1993. URL <http://stacks.iop.org/0953-4075/26/i=13/a=016>.
- [70] P. Cacciani, E. Luc-Koenig, J. Pinard, C. Thomas, and S. Liberman. Experimental studies of a diamagnetic multiplet in odd rydberg states of lithium. *Phys. Rev. Lett.*, 56:1124–1127, Mar 1986. doi: 10.1103/PhysRevLett.56.1124. URL <http://link.aps.org/doi/10.1103/PhysRevLett.56.1124>.
- [71] Roderick V. Jensen. Quantum chaos. *Nature*, 355(6358):311, 1992. URL <http://dx.doi.org/10.1038/355311a0>.
- [72] D. Wintgen and H. Friedrich. Regularity and irregularity in spectra of the magnetized hydrogen atom. *Phys. Rev. Lett.*, 57:571–574, Aug 1986. doi: 10.1103/PhysRevLett.57.571. URL <http://link.aps.org/doi/10.1103/PhysRevLett.57.571>.
- [73] Reinhardt, W. P. and Farrelly, D. The quadratic zeeman effect in hydrogen: an example of semi-classical quantization of a strongly non-separable but almost integrable system. *J. Phys. Colloques*, 43:C2–29–C2–43, 1982. doi: 10.1051/jphyscol:1982204. URL <http://dx.doi.org/10.1051/jphyscol:1982204>.
- [74] A Harada and H Hasegawa. Correspondence between classical and quantum chaos for hydrogen in a uniform magnetic field. *Journal of Physics A: Mathematical and General*, 16(8):L259, 1983. URL <http://stacks.iop.org/0305-4470/16/i=8/a=001>.
- [75] J. R. Guest and G. Raithel. High- $|m|$  rydberg states in strong magnetic fields. *Phys. Rev. A*, 68:052502, Nov 2003. doi: 10.1103/PhysRevA.68.052502. URL <http://link.aps.org/doi/10.1103/PhysRevA.68.052502>.
- [76] M.E. Glinsky and T.M. O’Neil. Guiding center atoms: Three-body recombination in a strongly magnetized plasma. *Phys. Fluids B*, 3:1279, Mar 1991. doi: 10.1063/1.859820. URL <http://link.aps.org/doi/10.1063/1.859820>.
- [77] M. Razavy. *Quantum Theory of Tunneling*. World Scientific, 2003. ISBN 9789812380180. URL <http://books.google.com/books?id=Smu8QgAACAAJ>.

- [78] William Happer. Optical pumping. *Rev. Mod. Phys.*, 44:169–249, Apr 1972. doi: 10.1103/RevModPhys.44.169. URL <http://link.aps.org/doi/10.1103/RevModPhys.44.169>.
- [79] J.H. Taylor. *Optical Pumping*. 2009. URL [http://www.princeton.edu/~romalis/PHYS312/Optical\\_pumping.pdf](http://www.princeton.edu/~romalis/PHYS312/Optical_pumping.pdf).
- [80] E. Arimondo, M. Inguscio, and P. Violino. Experimental determinations of the hyperfine structure in the alkali atoms. *Rev. Mod. Phys.*, 49:31–75, Jan 1977. doi: 10.1103/RevModPhys.49.31. URL <http://link.aps.org/doi/10.1103/RevModPhys.49.31>.
- [81] H.J. Metcalf and P. Van Der Straten. *Laser Cooling and Trapping*. Graduate Texts in Contemporary Physics. Springer, 1999. ISBN 9780387987286. URL <http://books.google.com/books?id=i-40VaXqrj0C>.
- [82] Z. T. Lu, K. L. Corwin, M. J. Renn, M. H. Anderson, E. A. Cornell, and C. E. Wieman. Low-velocity intense source of atoms from a magneto-optical trap. *Phys. Rev. Lett.*, 77:3331–3334, Oct 1996. doi: 10.1103/PhysRevLett.77.3331. URL <http://link.aps.org/doi/10.1103/PhysRevLett.77.3331>.
- [83] J.J. Arlt, O. Marag, S. Webster, S. Hopkins, and C.J. Foot. A pyramidal magneto-optical trap as a source of slow atoms. *Optics Communications*, 157(1-6):303 – 309, 1998. ISSN 0030-4018. doi: 10.1016/S0030-4018(98)00499-4. URL <http://www.sciencedirect.com/science/article/pii/S0030401898004994>.
- [84] E. Hansis, T. Cubel, J.-H. Choi, J.R. Guest, and G. Raithel. Simple pressure-tuned fabryprot interferometer. *Rev. Sci. Instrum*, 76:033105, Mar 2005. doi: 10.1063/1.1866237. URL <http://dx.doi.org/10.1063/1.1866237>.
- [85] Joseph Ladislav Wiza. Microchannel plate detectors. *Nuclear Instruments and Methods*, 162(13):587 – 601, 1979. ISSN 0029-554X. doi: 10.1016/0029-554X(79)90734-1. URL <http://www.sciencedirect.com/science/article/pii/0029554X79907341>.
- [86] Aaron Wexler. Evaporation rate of liquid helium. i. *J. Appl. Phys*, 22(12):1463, 1951. URL <http://dx.doi.org/10.1063/1.1699893>.
- [87] ANDOR Technology. MS Windows NT kernel description, 2013. URL <http://www.andor.com/scientific-cameras/ixon-emccd-camera-series/ixon3-860>.
- [88] S. Urabe, M. Watanabe, H. Imajo, K. Hayasaka, U. Tanaka, and R. Ohmukai. Observation of doppler sidebands of a laser-cooled ca<sup>+</sup> ion by using a low-temperature-operated laser diode. *Applied Physics B: Lasers and Optics*, 67:223–227, 1998. ISSN 0946-2171. URL <http://dx.doi.org/10.1007/s003400050497>. 10.1007/s003400050497.
- [89] D.R. Bates and I. Estermann. *Advances in Atomic & Molecular Physics*, volume 1, pages 347-351, Elsevier Science 1965.
- [90] J. E. Bjorkholm. Collision-limited lifetimes of atom traps. *Phys. Rev. A*, 38:1599–1600, Aug 1988. doi: 10.1103/PhysRevA.38.1599. URL <http://link.aps.org/doi/10.1103/PhysRevA.38.1599>.
- [91] T. Arpornthip, C. A. Sackett, and K. J. Hughes. Vacuum-pressure measurement using a magneto-optical trap. *Phys. Rev. A*, 85:033420, Mar 2012. doi: 10.1103/PhysRevA.85.033420. URL <http://link.aps.org/doi/10.1103/PhysRevA.85.033420>.
- [92] E. Hansis, T. Cubel, J.-H. Choi, J. R. Guest, and G. Raithel. Simple pressure-tuned fabry-pérot interferometer. *Review of Scientific Instruments*, 76(3):033105 –033105–3, Mar 2005. ISSN 0034-6748. doi: 10.1063/1.1866237.

- [93] Wenhui Li, Paul J. Tanner, and T. F. Gallagher. Dipole-dipole excitation and ionization in an ultracold gas of rydberg atoms. *Phys. Rev. Lett.*, 94:173001, May 2005. doi: 10.1103/PhysRevLett.94.173001. URL <http://link.aps.org/doi/10.1103/PhysRevLett.94.173001>.
- [94] M.C. Gutzwiller. *Chaos in Classical and Quantum Mechanics*. Interdisciplinary Applied Mathematics. Springer, 1990. ISBN 9780387971735. URL <http://books.google.com/books?id=fn03XYYpU54C>.
- [95] H. Friedrich. *Theoretical Atomic Physics*. Advanced Texts in Physics Series. Springer-Verlag, 2006. ISBN 9783540641247. URL <http://books.google.com.au/books?id=7JyfqB4co1IC>.
- [96] R.R. Jones, P. Fu, and T. F. Gallagher. Alteration of the lifetimes of autoionizing states by a circularly polarized microwave field. *J. Chem. Phys.*, 106:3578, Nov. 1997. doi: 0.1063/1.473453. URL <http://dx.doi.org/10.1063/1.473453>.
- [97] Chun-ho Iu, George R. Welch, Michael M. Kash, Long Hsu, and Daniel Kleppner. Orderly structure in the positive-energy spectrum of a diamagnetic rydberg atom. *Phys. Rev. Lett.*, 63:1133–1136, Sep 1989. doi: 10.1103/PhysRevLett.63.1133. URL <http://link.aps.org/doi/10.1103/PhysRevLett.63.1133>.
- [98] Jianing Han, Yasir Jamil, D. V. L. Norum, Paul J. Tanner, and T. F. Gallagher. Rb  $nf$  quantum defects from millimeter-wave spectroscopy of cold  $^{85}\text{Rb}$  rydberg atoms. *Phys. Rev. A*, 74:054502, Nov 2006. doi: 10.1103/PhysRevA.74.054502. URL <http://link.aps.org/doi/10.1103/PhysRevA.74.054502>.
- [99] Rudolf Grimm, Matthias Weidemller, and Yurii B. Ovchinnikov. Optical dipole traps for neutral atoms. 1999. URL <http://arxiv.org/pdf/physics/9902072.pdf>.
- [100] Bindiya Arora and B. K. Sahoo. State-insensitive trapping of rb atoms: Linearly versus circularly polarized light. *Phys. Rev. A*, 86:033416, Sep 2012. doi: 10.1103/PhysRevA.86.033416. URL <http://link.aps.org/doi/10.1103/PhysRevA.86.033416>.
- [101] C. Slowe, L. Vernac, and L. V. Hau. High flux source of cold rubidium atoms. *Review of Scientific Instruments*, 76:103101, Oct 2005. doi: 10.1063/1.2069651. URL <http://dx.doi.org/10.1063/1.2069651>.
- [102] T. Cubel Liebisch, A. Reinhard, P. R. Berman, and G. Raithel. Atom counting statistics in ensembles of interacting rydberg atoms. *Phys. Rev. Lett.*, 95:253002, Dec 2005. doi: 10.1103/PhysRevLett.95.253002. URL <http://link.aps.org/doi/10.1103/PhysRevLett.95.253002>.
- [103] A. Schwarzkopf, R. E. Sapiro, and G. Raithel. Imaging spatial correlations of rydberg excitations in cold atom clouds. *Phys. Rev. Lett.*, 107:103001, Aug 2011. doi: 10.1103/PhysRevLett.107.103001. URL <http://link.aps.org/doi/10.1103/PhysRevLett.107.103001>.
- [104] Kilian Singer, Jovica Stanojevic, Matthias Weidemller, and Robin Ct. Long-range interactions between alkali rydberg atom pairs correlated to the  $n s n s$ ,  $n p n p$  and  $n d n d$  asymptotes. *Journal of Physics B: Atomic, Molecular and Optical Physics*, 38(2):S295, 2005. URL <http://stacks.iop.org/0953-4075/38/i=2/a=021>.
- [105] M. Amoretti, C. Amsler, G. Bonomi, A. Bouchta, P. Bowe, C. Carraro, C. L. Cesar, M. Charlton, M. J. T. Collier, M. Doser, V. Filippini, K. S. Fine, A. Fontana, M. C. Fujiwara, R. Funakoshi, P. Genova, J. S. Hangst, R. S. Hayano, M. H. Holzscheiter, L. V. Jorgensen, V. Lagomarsino, R. Landua, D. Lindelof, E. Lodi Rizzini, M. Macri, N. Madsen, G. Manuzio, M. Marchesotti, P. Montagna, H. Pruys, C. Regenfus, P. Riedler, J. Rochet, A. Rotondi, G. Rouleau, G. Testera, A. Variola, T. L. Watson, and D. P. van der Werf. Production and detection of cold antihydrogen atoms. *Nature*, 419:456, Oct 2002. doi: 10.1038/nature01096. URL <http://dx.doi.org/10.1038/nature01096>.

- [106] G. Gabrielse, P. Laroche, D. Le Sage, B. Levitt, W. S. Kolthammer, R. McConnell, P. Richerme, J. Wrubel, A. Speck, M. C. George, D. Grzonka, W. Oelert, T. Sefzick, Z. Zhang, A. Carew, D. Comeau, E. A. Hessels, C. H. Storry, M. Weel, and J. Walz. Antihydrogen production within a penning-icoffe trap. *Phys. Rev. Lett.*, 100:113001, Mar 2008. doi: 10.1103/PhysRevLett.100.113001. URL <http://link.aps.org/doi/10.1103/PhysRevLett.100.113001>.
- [107] H. Gao, D. R. DeWitt, R. Schuch, W. Zong, S. Asp, and M. Pajek. Observation of enhanced electron-ion recombination rates at very low energies. *Phys. Rev. Lett.*, 75:4381–4384, Dec 1995. doi: 10.1103/PhysRevLett.75.4381. URL <http://link.aps.org/doi/10.1103/PhysRevLett.75.4381>.
- [108] R. S. Fletcher, X. L. Zhang, and S. L. Rolston. Using three-body recombination to extract electron temperatures of ultracold plasmas. *Phys. Rev. Lett.*, 99:145001, Oct 2007. doi: 10.1103/PhysRevLett.99.145001. URL <http://link.aps.org/doi/10.1103/PhysRevLett.99.145001>.
- [109] F. Robicheaux. Three-body recombination for electrons in a strong magnetic field: Magnetic moment. *Phys. Rev. A*, 73:033401, Mar 2006. doi: 10.1103/PhysRevA.73.033401. URL <http://link.aps.org/doi/10.1103/PhysRevA.73.033401>.
- [110] F. Robicheaux, J. V. Hernández, T. Topçu, and L. D. Noordam. Simulation of coherent interactions between rydberg atoms. *Phys. Rev. A*, 70:042703, Oct 2004. doi: 10.1103/PhysRevA.70.042703. URL <http://link.aps.org/doi/10.1103/PhysRevA.70.042703>.
- [111] Kwanghsi Wang and Shih-I Chu. Dynamics of multiphoton excitation and quantum diffusion in rydberg atoms. *Phys. Rev. A*, 39:1800–1808, Feb 1989. doi: 10.1103/PhysRevA.39.1800. URL <http://link.aps.org/doi/10.1103/PhysRevA.39.1800>.
- [112] I. Percival. *Quantum State Diffusion*. Cambridge University Press, 2005. ISBN 9780521021203. URL <http://books.google.com/books?id=iejnHAAACAAJ>.
- [113] G. Breit and I. I. Rabi. Measurement of nuclear spin. *Phys. Rev.*, 38:2082–2083, Dec 1931. doi: 10.1103/PhysRev.38.2082.2. URL <http://link.aps.org/doi/10.1103/PhysRev.38.2082.2>.
- [114] D.A. Steck. Rubidium 85 D line data. Sept. 2012. URL <http://steck.us/alkalidata>.
- [115] D.A. Steck. Rubidium 87 D line data. May. 2008. URL <http://steck.us/alkalidata>.